

Laser Microspot Welding for Interconnection of Back-contacted Silicon Solar Cells

Von der Fakultät für Mathematik und Physik
der Gottfried Wilhelm Leibniz Universität Hannover
zur Erlangung des Grades

Doktor der Naturwissenschaften

Dr. rer. nat.

genehmigte Dissertation

von

M. Sc. Henning Schulte-Huxel

geboren am 10.01.1985, in Dorsten

2015

Referent: Prof. Dr.-Ing. Rolf Brendel
Korreferent: Prof. Dr. Jozef Poortmans
Tag der Vorlage: 29.07.2015
Tag der Promotion: 18.11.2015

Abstract

This work presents a new laser microspot welding process for the interconnection of aluminum metallized crystalline silicon solar cells and the investigation of this process. Furthermore, it demonstrates the application of laser welding for interconnection of back-junction back-contacted solar cells.

In the current production, the majority of silicon solar cells is interconnected by soldering a solder-coated copper ribbon to its front and rear side. This process induces thermomechanical stress in the brittle silicon solar cells and demands metal surfaces free of stable oxides, e.g., silver. In this work, a pulsed laser welding process for solar cell interconnection is developed to minimize the mechanical stress and to omit the use of cost-intensive silver by contacting aluminum. The interconnects consist of a 10- μm -thick aluminum layer. It is attached to a substrate, which is transparent for the laser irradiation. A laser irradiates the aluminum layer through this substrate in order to weld it to the aluminum metallization of the solar cell. The so-called aluminum-based mechanical and electrical laser interconnection (AMELI) process is analyzed for pulse durations of 20 ns and 1.3 μs and the process windows for these laser sources are determined. The electrical contact resistivity of the laser welded interconnections is determined to be less than 10 $\mu\Omega\text{ cm}^2$. Mechanical tear-off stresses of up to 450 kPa are measured. Additionally, the laser induced damage to the silicon surface passivation and silicon crystal is investigated using specially designed test structures. Silicon samples with aluminum layers as thin as one micrometer can be electrically and mechanically contacted without inducing any detectable laser damage.

The thermal processes involved in the laser interconnection process are investigated by microscopic surface analysis and the finite element method simulations. They show that a transparent substrate is indispensable for the welding process. For an aluminum layer thickness up to 5 μm , the process is dominated by thermal diffusion. For thicker layers, the melting at the irradiated surface that is in contact with the substrate results in material expansion causing a breakage of the solid layer and ejection of molten aluminum.

The impact of the laser interconnection process on back-junction back-contacted solar cells is studied. The full performance of the solar cells can be transferred to the module level by the laser process. The modules reach efficiencies of up to 20.4%. In artificial aging, laser interconnected modules experience no significant degradation of the fill factor after 1402 humidity-freeze cycles proving their longterm stability. Additionally, the successful interconnection of solar cells with a thickness of 90 μm is demonstrated. To avoid losses associated with the busbars required for solder interconnection, solar cells without busbars are interconnected. This results in an efficiency increase from cell to module of 4% relative and an absolute efficiency of 22.1%. Detailed analysis of the characteristic *I-V*-parameters show that this increase is caused by a reduction of the series resistance by a factor of three. This leads to module fill factors of 80.5%. Additionally, the process is further developed for the interconnection of solar cells with two dimensional contact structures by employing the high lateral precision of laser systems.

The results of this work suggest that laser welding is an alternative to the widely used soldering process. Laser microspot welding enables a significant reduction of material consumption, has proven its longterm stability, and opens new opportunities for advanced solar cell designs with improved efficiencies.

Keywords: photovoltaics, module interconnection, back-junction back-contacted solar cell, laser welding, aluminum, silicon solar cells

Zusammenfassung

In dieser Arbeit wird ein neuer laserbasierter Mikroschweißprozess zur Verschaltung von aluminiummetallisierten, kristallinen Silizium-Solarzellen präsentiert und analysiert. Zudem wird die Anwendung des Laserschweißens für die Verschaltung von Rückkontakt-Solarzellen demonstriert.

In der industriellen Produktion wird heute der überwiegende Teil der Solarzellen mittels Lötens verschaltet, indem ein lotummantelter Flachdraht von der Vorderseite auf die Rückseite der Solarzelle geführt wird. Dieser Prozess induziert jedoch thermomechanische Spannung in das spröde Silizium und benötigt Oberflächen, die frei von stabilen Oxiden sind, wie z.B. Silber. In dieser Arbeit wird ein gepulster Laserschweißprozess für die Verschaltung von aluminiummetallisierten Solarzellen entwickelt, um die mechanischen Spannungen zu minimieren und das kostenintensive Silber zu vermeiden. Eine 10 μm dicke Aluminiumschicht dient hierbei als Verbinder. Diese ist mit einem Substrat verbunden, das transparent für die verwendete Laserstrahlung ist. Die Aluminiumschicht wird durch das Substrat hindurch mit einem Laser bestrahlt, um sie mit der Zellmetallisierung zu verschweißen. Der sogenannte AMELI (aluminumbased mechanical and electrical laser interconnection) Schweißprozess wird für Pulsdauern von 20 ns und 1.3 μs analysiert und die jeweiligen Prozessfenster bestimmt. Der elektrische Kontaktwiderstand der Laserschweißverbindung wird mit unter 10 $\mu\Omega\text{ cm}^2$ gemessen. Mechanische Abrissspannungen von bis zu 450 kPa werden ermittelt. Der laserinduzierte Schaden von passivierten Siliziumoberflächen und Kristallschädigungen werden mit Teststrukturen untersucht. Siliziumproben mit Aluminiummetallisierungen, deren Schichtdicke bis auf einen Mikrometer reduziert wird, können ohne detektierbaren Schaden mechanisch und elektrisch kontaktiert werden.

Die thermischen Prozesse, die im Laserschweißprozess auftreten, werden mittels mikroskopischer Oberflächenanalyse und Simulationen auf Basis der Finiten Elementen Methode untersucht. Es wird gezeigt, dass das transparente Substrat unabdingbar für den verwendeten Prozess ist. Für Aluminiumschichten bis zu einer Dicke von 5 μm wird der Prozess durch thermische Diffusion dominiert. Für dickere Schichten resultiert aus dem Aufschmelzen des Aluminiums an der bestrahlten Oberfläche, die in Kontakt mit dem Substrat ist, eine Materialausdehnung, die zu Rissen in der Schicht und zum Auswurf von flüssigem Aluminium führt.

Der Einfluss der Laserverbindung wird in der Anwendung am Beispiel von Rückkontakt-Solarzellen untersucht. Die volle Leistung der Solarzellen kann mittels des Laserprozesses ins Modul übertragen werden. Die Module erreichen einen Wirkungsgrad von bis zu 20,4%. In beschleunigten Alterungstests erfahren die lasergeschweißten Module keine signifikante Degradation des Füllfaktors nach 1402 Feuchte-Frost-Zyklen, was ihre Langzeitstabilität belegt. Zusätzlich wird die erfolgreiche Verschaltung von 90 μm dicken Solarzellen demonstriert. Um Verluste zu vermeiden, die mit den für das Lötens benötigten Stromsammelschienen einhergehen, werden Solarzellen ohne Stromsammelschienen verschaltet. Hierdurch wird eine relative Effizienzsteigerung von 4% und ein Wirkungsgrad von 22,1% erreicht. Detaillierte Analysen der charakteristischen I - V -Parameter zeigen, dass diese Steigerung aus der Reduzierung des Serienwiderstandes um den Faktor drei resultiert. Dies erlaubt Modul-Füllfaktoren von 80,5%. Unter Ausnutzung der hohen örtlichen Präzision von Laseranlagen ist ein Verschaltungsprozess auch für punktkontaktierte Rückkontakt-

Solarzellen entwickelt.

Die Ergebnisse dieser Arbeit zeigen, dass das Laserschweißen eine Alternative zum etablierten Lötprozess zur Verschaltung von Solarzellen darstellt. Laserschweißen erlaubt eine deutliche Verringerung des Materialverbrauches, trägt zur Erhöhung der Langzeitstabilität von Modulen bei und eröffnet neue Möglichkeiten für weiterentwickelte Zellstrukturen mit höherem Wirkungsgrad.

Schlagwörter: Photovoltaik, Modulverschaltung, Rückkontakt-Solarzellen, Laserschweißen, Aluminium, Silizium-Solarzellen

Table of Contents

1	Introduction	1
2	State-of-the-art and theory of module interconnection and laser welding	3
2.1	Back-contacted solar cells	3
2.2	State-of-the-art of module interconnection techniques	5
2.2.1	Solar cell interconnection by soldering	5
2.2.2	Solar cell interconnection by conductive adhesives	6
2.2.3	Multi-level metallization for back-contacted solar cells	7
2.3	Laser ablation and welding	8
2.3.1	Photothermal surface heating	8
2.3.2	Laser-induced forward transfer	11
2.3.3	Laser welding	12
2.3.4	Welding in photovoltaics	13
3	Experimental conditions of the laser welding process	15
3.1	Laser welding process	15
3.2	Laser systems	16
3.3	Sample preparation	18
3.3.1	Substrates	18
3.3.2	Silicon samples and solar cells	19
3.4	Characterization techniques	20
3.4.1	Tear-off test	20
3.4.2	Electrical resistance measurements	22
3.4.3	Infrared lifetime mapping	23
3.4.4	Infrared lock-in thermography	24
3.4.5	Camera-based luminescences measurements	25
3.4.6	Light-beam-induced current	26
3.4.7	Accelerated aging	26
4	Experimental results of the laser welding	27
4.1	Laser welding on glass substrates by the ns laser	27
4.1.1	Mechanical properties and laser-induced damage	27
4.1.2	Electrical properties	32
4.2	Laser welding on glass substrates by the μ s laser	33
4.2.1	Mechanical properties and laser-induced damage	33
4.2.2	Test of process limits on solar cells	35
4.2.3	Electrical properties	36
4.3	Laser welding on foil substrate by the μ s laser	37
4.3.1	Laser-induced damage	37
4.3.2	Mechanical properties	38

4.3.3	Electrical properties	39
4.4	Chapter summary and discussion	40
4.4.1	Comparison of the laser systems	40
4.4.2	Comparison of the glass and foil substrates	42
4.4.3	Electrical properties of the laser welds	43
4.4.4	Summary	43
5	Thermal processes involved in the AMELI laser welding process	45
5.1	Experimental determination of melt-through threshold	45
5.2	Two dimensional finite element method	48
5.2.1	Simulation results for melt-through by thermal diffusion	50
5.2.2	Simulation results for onset of melting at the irradiated interface	51
5.3	Estimation of energy losses	52
5.4	Interface properties between the two Al layers	55
5.5	Chapter summary and discussion	57
6	Module interconnection of BJBC solar cells by laser welding	59
6.1	Two busbar modules	59
6.1.1	Glass substrate	60
6.1.2	Foil substrate	62
6.1.3	Artificial aging	65
6.2	Single busbar modules	68
6.3	Busbar-free modules	72
6.3.1	Fill factor	76
6.3.2	Open-circuit voltage	79
6.3.3	Short-circuit current density	80
6.3.4	Efficiency	85
6.4	Two dimensional contact structure	85
6.4.1	Application of the multi-level metallization	86
6.4.2	Reduction of series resistance by the multi-level metallization	88
6.4.3	Mechanical aspects in dependence on solar cell size	89
6.5	Chapter summary and discussion	89
7	Summary and Outlook	95
A	Appendix	99
A.1	Comparison of conductivities and prices for Al, Ag, and Cu	99
A.2	Additional experimental details to section 3.3.2	99
A.3	Comparison of interconnect resistances	100
A.4	Qualitative correlations between mechanical and electrical properties	101
A.5	Input parameters for the FEM simulations 5.2	103
A.6	Oscillating temperature effect at thermal barrier	105
A.7	Input parameters for numerical device simulations in section 6.3.1	106
	Bibliography	107
	List of publication	121

Curriculum vitae	124
Danksagung	126

1 Introduction

Solar cells exposed to sunlight transform the solar radiation into electrical power. In order to make use of this property, the solar cells' functionality under environmental conditions must be ensured desirably for two or more decades. Additionally, single solar cells provide only limited voltage levels. In order to reach higher voltages, the individual solar cells are connected in series. Hereby, the voltages of the individual cells sum up and result in a sufficiently high voltage that can be efficiently converted from the direct current of the solar cells into alternating current of the electrical grid [1]. Additionally, at higher voltages the relative resistive power losses are reduced. To protect the interconnected solar cells from humidity, chemical, and mechanical impact, they are encapsulated into an elastic material and covered by glass or non-permeable foils. A module is by definition "a collection of individual solar cells integrated into a package that protects them from the environment in which the module is installed for a long period of time" [2].

For an economical power generation one has to maximize the energy conversion from solar irradiation to electrical output and to minimize the production costs. In order to achieve a high energy conversion efficiency η for modules, first of all highly efficient solar cells are required. Crystalline silicon is dominating the photovoltaic (PV) market with a share of 90% in 2013 [3]. Recently in the year 2014, the long-standing record in energy conversion efficiency for crystalline silicon solar with a single junction under one sun was broken by different research groups [4–7]. All these cells feature the *p-n*-junction and the contacts for both polarities on their rear side, so-called back-junction back-contact (BJBC) solar cells. Modules using such cells reach the highest conversion efficiency of $\eta = 22.4\%$ on large area ($A = 1.58 \text{ m}^2$) [7, 8]. It is only possible to achieve such high module efficiencies if all optical,



Figure 1.1: PV modules installed on a building roof.
Picture taken from www.sunpower.de/haus/solarmodule-schwarz/:30.12.2014

electrical, and other losses are minimized. One way is to optimize the cell and the module separately, as it is often done in research institutes. Alternatively, one may simultaneously develop both, cell and module combined, to benefit from synergy effects in order to use the sunlight as efficient as possible.

Over the last decades soldering, has proven to be a reliable interconnection technique for solar cells [2, 9, 10]. However, it requires solderable metallization, mostly silver, which is a significant cost driver in the photovoltaic production [11]. An attractive choice for the metallization of Si solar cells is aluminum, an abundant element on earth, due to its low material costs compared to other commonly used metals like silver or copper. Although aluminum has a slightly lower conductivity than copper and silver, the cost advantage compensates this aspect¹. Investigations of Al impurities, which form during the crystallization process of the Si ingot, show recombination activity of Al [12–14]. However, these defects form only at high temperatures ($>900^\circ\text{C}$) [15, 16]. At lower temperatures as they occur during cell back-end and module processing only marginal effects were observed [15]. Additionally, the diffusion coefficient of Al [14, 17] in Si is 6 to 7 orders of magnitude lower compared to other metals like Cu and Fe [18–20]. Therefore, a contact between Al and Si is uncritical. This makes aluminum a well suitable metal for contacting Si solar cells.

Another drawback of the soldering process is that it induces mechanical stress [21–25], which can result in cell breakage. Therefore, soldering is known to be the process step with one of highest yield losses during the whole production chain [21, 26]. This becomes even more critical for thin ($< 120\ \mu\text{m}$) Si solar cells, which have the potential of increasing the efficiency [27, 28] and decreasing the material consumption and thus production costs [29, 30]. Thus, there is a need for an interconnection process that avoids the consumption of cost-intensive materials like silver, minimizes mechanical stress, and offers sufficient flexibility for a combined cell and module development.

Therefore, we developed the so-called AMELI process, a new interconnection method for BJBC solar cells, which is the focus of this work. AMELI stands for aluminum-based mechanical and electrical laser interconnection. We apply laser microspot welding to contact a thin ($\approx 10\ \mu\text{m}$) Al layer serving as interconnect to the rear side of an Al metallized BJBC solar cell. The laser radiation heats the aluminum layer only locally to form weld spots with a size of 50 to 100 μm . AMELI avoids mechanical stress that otherwise originates from the difference in thermal expansion of the solar cell and the interconnect, which occurs when both parts are heated entirely. Additionally, the AMELI process offers the opportunity of novel interconnection designs, which enables the development of the cell-to-module interface.

In this work, we investigate the AMELI process with respect to its mechanical and electrical properties, as well as its impact on the surface passivation underneath the metallization. The relevant physical processes driving our welding process are studied by scanning electron microscope and numerical simulations of the thermal diffusion. We apply the AMELI method to various types of solar cells. It is shown how the solar cell design and, thus, the cell efficiency, benefits from the novel interconnection method and its application to thin ($< 100\ \mu\text{m}$) solar cells.

¹A comparison of the prices and conductivities is given in appendix A.1

2 State-of-the-art and theory of module interconnection and laser welding

In this chapter, we introduce different concepts for the interconnection of back-contacted solar cells with their advantages and limitations. Since the laser is the key tool applied in this work, we present the basic concepts of light-matter interaction as well as the previous application of laser processing in PV.

2.1 Back-contacted solar cells

Back-contacted solar cells have been used since the very beginning of Si photovoltaics in 1955 [31, 32] and demonstrated high energy conversion efficiencies of up to 25.6% until today [4, 5, 33–36]. In contrast to bifacially contacted solar cells (Fig.2.1 a)), the contacts for both polarities are on the rear side. Therefore, back-contacted solar cells have reduced or no shading due to the minimized area fraction or absence of metal contacts on the front side, which increases the efficiency. However, they require an adapted interconnection process, which is focus of this work.

Different types of back-contacted solar cells have been developed. Among them the most important classes are [34]:

- Metallization wrap-through (MWT) solar cells [37, 38] (Fig.2.1 b)): The emitter on the front side of these solar cells is contacted with a metal grid. The solar cells feature holes filled with metal, through which the front grid is connected to contact pads on the rear side. This reduces the shading losses by busbars, i.e., wide metal structures on the front side that collect the current of the individual fingers, and by interconnects on the front side.
- Emitter wrap-through (EWT) solar cells [39](Fig.2.1 c)): They have in contrast to MWT cells no metal grid on their front side. The emitter covers not only the front side, but is also diffused into the walls of numerous holes in the cell. The front side is electrically contacted to metallized contact points on the rear side through the highly doped, conductive emitter layer in the holes.
- Back-junction back-contact (BJBC) solar cells [40, 41] (Fig.2.1 d)): They feature the emitter as well as the back surface field (BSF) on their the rear side, where both polarities are contacted.

For further detail please refer to [34, 42].

Among the back-contacted solar cells, BJBC cells reach the highest efficiencies [4, 5, 35]. However, they require a complex processing sequence. Although the BJBC solar cells are free from optical shading, an effect called electrical shading decreases the current collection

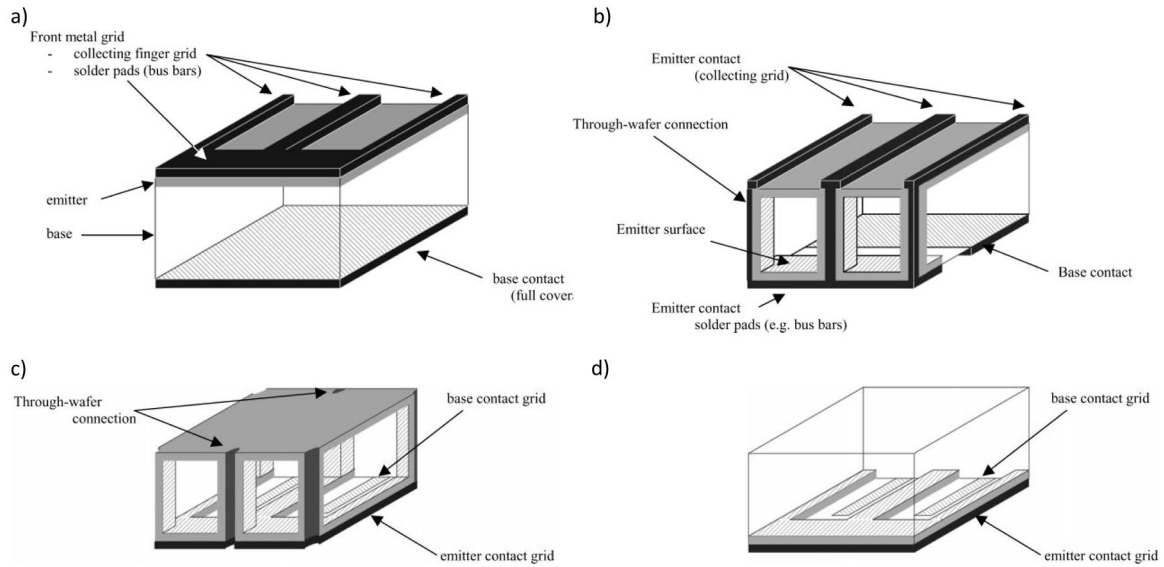


Figure 2.1: Schematic of different solar cell designs: a) conventional bifacially contacted solar cell, b) metallization wrap-through solar cell, c) emitter wrap-through solar cell, and d) back-junction back-contact solar cell. Image taken from [34]

[43–46]. Above the BSF or undoped regions, the recombination of the minority charge carriers is larger compared to the emitter regions. In order to increase the collection probability of the minority charge carriers, the emitter area should be maximized. When the metallization geometry coincides with the doping geometry, emitter and base metallization have non-symmetric cross-sections. This leads to an increased series resistance [47].

Decoupling the metallization and doping geometry requires for example thick insulating dielectric layers. Ensuring a high insulation on a large area is known to be challenging with commonly used passivation layers [48–50]. Another approach are adaptations of the cell structure, for example buried emitter solar cells [47]. However, buried emitters are double-diffused p^+n^+ -junctions that also have specific disadvantages, like the potential to cause junction shunting via trap assisted tunnelling [47].

The current of the individual fingers is collected in busbars. These are often located at the edge of the solar cells. For each polarity, the busbar is at one edge, vis-à-vis to the other polarity. The busbars are much wider than the fingers and, hence, the electrical shading effect of the busbars is even more critical. A diffusion of the minority charge carriers generated above the busbar to an emitter region is more unlikely for the busbars than for the fingers. Therefore, the base busbars reduce the current significantly. Above the emitter busbars, the majority charge carriers are able to diffuse to the next base region, but they experience a certain resistance. This increases the total series resistance of the solar cell resulting in a reduction of the fill factor [44, 51, 52].

To avoid the negative impact of the busbars and to decouple the metallization and doping geometry, an alternative interconnection scheme needs to be developed. This is the focus of this work. A combined development of cell and module aiming to maximize the cell efficiency and minimize the interconnection losses is advantageous.

2.2 State-of-the-art of module interconnection techniques

Individual solar cells are integrated into larger units, i.e., modules. This enables to reach suitable voltage and current outputs, which can be fed into the electrical grid after conversion to alternating current, and easier handling during installation. The interconnection must be mechanically stable, have a low contact resistance, not induce any damage to the solar cells, avoid cost intensive material, and be longterm stable. Various interconnection processes have been developed to contact and interconnect back-contacted solar cells. In the following, a short overview of the most common processes is given.

2.2.1 Solar cell interconnection by soldering

Soldering has been used for decades to interconnect Si solar cells [9, 10] and is a well proven process that is used for almost all commercially available PV modules with crystalline Si solar cells. During soldering, a metal with a melting point lower than the melting point of the joining partners, i.e., solder, melts and solidifies afterwards to form the contact. For example, the commonly used solder (Sn62.5Pb36Ag1.5) has a melting point of 179 °C [53], whereas the melting point of silver is 962 °C. Therefore, the joining partners stay well below their melting temperatures during the soldering process [54].

Si solar cells are contacted using copper interconnects that are covered with solder. After the application of a flux to remove native oxides from the surface of the joining partners, the interconnects are soldered to the busbars or solder pads of the solar cell. During this, the interconnects as well as the solar cells are heated well above 180 °C.

Such solder joints have an electrical contact resistance ρ_c below 100 $\mu\Omega\text{cm}^2$, depending on the soldering technique [55]. Laser solder joints even reach contact resistances in the order of 10 $\mu\Omega\text{cm}^2$ [55].

The mechanical requirement of the solder joints for PV application is specified in DIN EN 50461 to be 1 N per mm of joint width and determined in a peel test [56]. Typically, values between 1 and 3 N/mm are reached. The long term stability of PV modules with solar cells interconnected by solder depends highly on the used material and the soldering process. Soldering has proven its long term stability in the fields over the last decades. Nevertheless, disconnected cell and string interconnect ribbons are well known for PV systems in operation [57] and are the main cause for customer complaints [58].

Although soldering is a widely used process, it has some drawbacks:

- Solderable metallizations that do not have a chemical highly stable oxide are necessary for a reliable connection [59]. These are in general cost intensive noble metals, like silver, or require a stack of different metallization [60], which complicates the process. Aluminum has a chemically stable oxide and is not solderable with the common processes.
- The unwanted oxides from the surface are removed by flux agents. These chemicals have the risk to interact with the lamination foil leading to bubble formation in the laminate [57].
- Leaded solder is still widely used [61] due to its lower melting temperature [62]. The melting point of Sn62Pb36Ag2 solder is 179 °C, whereas for lead-free Sn96.5Ag3.5 it

is 221 °C [53] . However, lead has to be abolished due to its environmental impact and legal obligations [63].

- Typically, different metals are involved in the solder interconnecting, like tin, silver, and lead in the solder, copper in the ribbon, and silver as well as aluminum in the paste on the cells¹. This enables electrochemical processes, like galvanic corrosion, which have a negative impact on the module longterm stability [62, 64]. Additionally, the large variety of metals requires several steps during recycling [65, 66].
- Due to the difference of the linear thermal expansion coefficient of silicon ($2.6 \times 10^{-6} \text{K}^{-1}$) [67] and copper ($16.8 \times 10^{-6} \text{K}^{-1}$) [68], mechanical stress is induced after cooling down to room temperature [21–25], which might induce cracks into the solar cell. The soldering process is known to result in one of the highest yield losses during processing, especially for thin solar cells [21, 26].

Today the only commercially available BJBC solar cells are interconnected by soldering, too [69, 70]. These are well know for their long term stability [58]. The busbars of this solar cells widen to form solder pads in the dimensions of approximately² $5 \times 5 \text{mm}^2$, which increases the busbar area with the previously mentioned drawbacks. In other processes for back-contacted solar cells, copper ribbons are soldered at two to eight busbars on the rear side of the solar cells [71–73].

2.2.2 Solar cell interconnection by conductive adhesives

Especially for back-contacted solar cells, where soldering is applied only on one side, the thermomechanical stress induced after cooling down is substantial [74, 75]. Conductive adhesives are an alternative, since they cure at lower temperatures than required for the common soldering processes. However, conductive adhesives in general require a metal surface with similar properties as the surface for soldering has to have for a stable interconnection. A direct contact to aluminum was not yet demonstrated for PV application and silver or oxidation stable layers need to be applied [76, 77]. Furthermore, conductive adhesives are cost intensive since they contain a large fraction of silver [76, 78, 79].

Conductive adhesives have a contact resistance ρ_c between $100 \mu\Omega\text{cm}^2$ and $500 \mu\Omega\text{cm}^2$ [79, 80]. Since the contact resistance degrades during artificial aging [80], a reduction of the module efficiency of 4% or more is observed after 200 humidity-freeze cycles [79] or 200 thermal cycles [52]. Peel strengths of 1.0 N/mm are achieved [79].

Conductive adhesives are used to interconnect bifacially contacted solar cells. Compared to the standard soldering process, no busbars are required on the front side and a direct contacting of the individual fingers is possible [79, 81]. Furthermore, they enable novel module concepts especially for back-contacted solar cells and have been successfully implemented in combination with conductive back sheets [74, 80, 82, 83]. A lamination foil with punched holes is placed between the conductive back sheet and the solar cell. The conductive adhesive is applied in these holes and cures during the lamination. This process enables the

¹The oxidation potentials of for example Ag/Ag(I), Cu/Cu(II), Pb/Pb(II) and Sn/Sn(II) are +0.799 V, +0.337 V, -0.126 V, -0.136 V, respectively [62].

²Images in reference [25, 70] show such solder pads, without stating the exact dimensions.

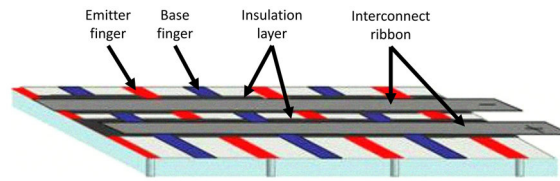


Figure 2.2: Schematic of busbar-free interconnection of EWT solar cells. The emitter and the base fingers are shown in red and blue, respectively. The gray layers are the interconnect ribbons and the black layer represents the patterned insulator layer, which isolates the interconnect ribbons from the fingers of the opposite polarity. Taken from [52].

reduction of the lamination foil thickness resulting in less material consumption³. Conductive adhesives also enable busbar-free concepts for back-contacted solar cells, see Fig.2.2. Hacke et al. [52] applied a screen-printable dielectric material to the rear side of EWT solar cells. It has several lines with openings on top of each polarity and, thus, isolates the ribbon from the other polarity. A conductive adhesive is applied onto these openings. This concept has proven to increase the cell efficiency by up to 2% absolute for busbar-free back-contacted solar cells by avoiding the busbar related losses.

2.2.3 Multi-level metallization for back-contacted solar cells

Busbar-free contacting of back-contacted solar cells can also be achieved using multi-level metallization first applied by Verlinden et al. [85, 86]. Figure 2.3 depicts the basic idea of the concept. In order to maximize the current collection, the emitter covers the largest fraction of the rear side. Its current is conducted in a metal layer, which is directly deposited on the rear side of the solar cell and covers the total rear side except for the base contacts (metal I). A dielectric layer (insulator) isolates the second layer (metal II) from the first. This insulator covers the whole metal layer I and leaves the base contacts open. The base region is then locally contacted to the second layer, which carries the base current. In this case, the metallization of each polarity occupies almost the total rear side of the solar cell and, thus, the series resistance is reduced. Further, it decouples the geometry of the metallization scheme from the doping geometry.

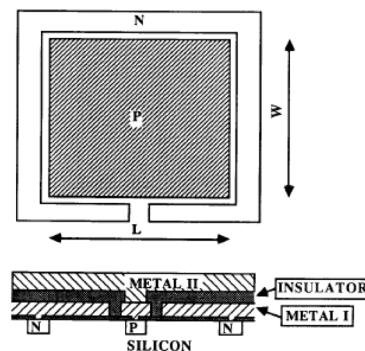


Figure 2.3: Schematic of multi-level metallization with two Al layers deposited on the rear side for contacting point-contacted solar cells [85].

³Alternatively to the conductive adhesives, solder paste can be used to contact the cells to the conductive backsheets. The melting of the solder within the module is achieved by laser irradiation [84].

However, the process presented by Verlinden et al. requires a complex processing: deposition of a first metal layer, contact separation, application of a stack of insulation layers (e.g., anodic oxidized Al and SiO_x), opening of the dielectric layers on the point contacts, deposition of a second metal layer, and module integration of the cells [86]. In total, it requires 13 steps among these four photolithography steps. In this work, we develop a simplified alternative process sequence.

2.3 Laser ablation and welding

As an alternative to the interconnection scheme discussed in section 2.2, laser welding is investigated in this work in order to avoid the drawbacks of soldering and conductive adhesives. Here, we introduce the underlying mechanisms aiming to understand the applied parameters as well as the models used to simulate and to describe the laser welding process. Additionally, we discuss our process in the context of laser welding in photovoltaics.

2.3.1 Photothermal surface heating

In this work, we use laser pulses with pulse duration of either $\tau_p = 20$ ns or 1.3 μ s to irradiate the aluminum surfaces. Therefore, the dominant light-matter interaction is the photothermal surface heating. The photons of the laser light excite electrons in the irradiated metal. The electrons thermal relax and the energy is transferred to the solid resulting in heating of the material. The optical penetration depth l_α in aluminum is about 10 nm for the used wavelengths of 355 nm and 1064 nm [87]. Therefore, we approximate the optical absorption by surface absorption and, thus, we assume surface heating. In other words, the heat is introduced by the light at the metal-ambient-interface and not within the material. The change in temperature also influences the heat capacity, thermal conductivity, optical absorption, and other material properties [87].

The temperature T within a homogeneous and isotropic material can be described by the Fourier heat-conduction equation [87, 88]

$$K(T)\nabla^2 T(\vec{x}, t) = \frac{\partial T(\vec{x}, t)}{\partial t}. \quad (2.1)$$

Here, $K(T)$ is the thermal diffusivity. It is related via $K = \kappa/(\rho c_p)$ to the density ρ of the material, its specific heat at constant pressure $c_p(T)$, and the thermal conductivity $\kappa(T)$. This equation extended by suitable heat sources for the laser-induced energy is also used in the finite element simulations for evaluation of the temperature distribution within our samples.

In order to describe the heat diffusion within a solid in one dimension, we solve equation 2.1 using the following ansatz for the temperature [87, 89]:

$$T(x, t) = T(0, t)e^{-\frac{x^2}{4Kt}}, \quad (2.2)$$

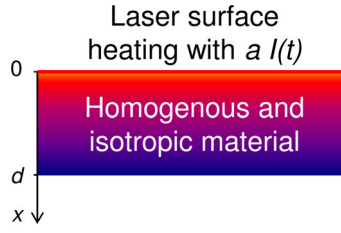


Figure 2.4: Schematic of a solid body with a thickness d and a surface absorptivity a heated by a laser with an intensity $I(t)$.

i.e., we assume a Gaussian decay of the temperature in depth. The characteristic length at which the temperature is decreased to $1/e$ is the thermal diffusion length [87]

$$l_T(t) = 2\sqrt{Kt}. \quad (2.3)$$

The thermal diffusion length l_T increases proportionally to \sqrt{t} . Thus, the heat diffuses into the solid and the temperature gradient decreases. Inserting the trial function 2.2 into the heat-conduction equation 2.1 results in

$$\frac{\partial T(0, t)}{\partial t} + \frac{T(0, t)}{2t} = 0. \quad (2.4)$$

This can be solved using the ansatz

$$T(0, t) = \frac{B}{\sqrt{t}}, \quad (2.5)$$

where B is a constant. Therefore, the maximum temperature is inversely proportional to l_T , which fulfills the requirement of energy conservation⁴.

For laser processing, the solution of equation 2.1 needs to be extended by a heat source. We can use the "heat-balance integral methode" [88, 90] to solve this in one dimension and for constant material properties. Using this approach, the partial differential equation 2.1 is solved by evaluating the temperature in an average sense, i.e., by integration of whole or part of the solid rather than at each point x . We assume a solid body between $x = 0$ and d , which is heated at its front surface by a laser, see Fig. 2.4. The method accounts only for longitudinal heat conduction and does not include any other heat loss mechanisms like convection, emission, and heat conduction parallel to the surface. Phase changes are included by dividing the heating process of the material into different time steps, e.g., the time until melting or evaporation is initiated at the front side or the time before the body is heated or melted through. For simplicity, the material properties are kept constant for each phase.

In the following, we briefly describe an example of the method for the time interval before vaporization starts on the front side and no appreciable heat has reached the rear side as presented by Harrach [88]. For the one dimensional case, the integration of equation 2.1

⁴For the one dimensional case solved here, with constant material parameters and no heat sources or losses the integral of $\int_{-\infty}^{\infty} T(x, t)c_p dx$ must be constant in time.

gives

$$\int_0^d K \frac{\partial^2 T}{\partial x^2} dx = \int_0^d \frac{\partial T}{\partial t} dx. \quad (2.6)$$

The laser-induced energy is included by suitable boundary conditions, e.g., the rate at which heat flows through the surface, which is irradiated by a laser with an intensity $I(t)$. For the irradiated front side this is given by [88, 89]

$$-\kappa \frac{\partial T}{\partial x} \Big|_{x=0} = aI(t), \quad (2.7)$$

where a is the surface absorptivity. Under the assumption that the heat has not yet reached the rear side of the solid body with a thickness d , it holds

$$\kappa \frac{\partial T}{\partial x} \Big|_{x=d} = 0. \quad (2.8)$$

Since both boundaries of the integral are constant for the case that evaporation has not yet started on the front side and the solid has a constant thickness, we can rewrite the right hand side of equation 2.6

$$\int_0^d \frac{\partial T}{\partial t} dx = \frac{d}{dt} \int_0^d T dx. \quad (2.9)$$

Using the boundary conditions 2.8 and 2.7 and constant material parameters the integration of the left-hand side in equation 2.6 results in

$$\frac{K}{\kappa} aI(t) = \frac{d}{dt} \int_0^d T dx. \quad (2.10)$$

According to [91] a suitable ansatz for the temperature is

$$\begin{aligned} T(x, t) &= T(0, t) \left(1 - \frac{x}{d_T(t)}\right)^2 e^{\frac{-x}{d_T(t)}} \\ &\text{for } 0 \leq x \leq d_T(t), \quad d_T(t) \leq d \\ &= 0 \text{ for } x > d_T(t). \end{aligned} \quad (2.11)$$

Here, $d_T(t)$ is the thermal penetration depth. It is defined such that the temperature is decreased to 50% of the surface temperature at $x = 0.21 d_T$ and to 15.2% at $x = 0.5 d_T$. Integrating equation 2.11 over x from 0 to d under the assumption that no heat reaches the rear side ($d > d_T$) and inserting the solution in equation 2.10 results in

$$\frac{d}{dt} T(0, t) d_T(t) = \frac{KaI(t)}{(1 - 2e^{-1})\kappa}. \quad (2.12)$$

In order to relate $T(0, t)$ to $d_T(t)$, we differentiate $T(x, t)$ with respect to x according to equation 2.7 and obtain

$$3K \frac{T(0, t)}{d_T(t)} = aI(t). \quad (2.13)$$

Under the assumption that $I(t)$ is a step-function with a constant intensity of I_0 and using equations 2.12 and 2.13, we arrive at the solutions for $T(0, t)$ and $d_T(t)$ when t is smaller or equal to the laser pulse duration τ_p

$$T(0, t) = \left(\frac{Kt}{3(1 - 2e^{-1})} \right)^{\frac{1}{2}} \frac{aI_0}{\kappa}, \quad (2.14)$$

$$d_T(t) = \left(\frac{3Kt}{1 - 2e^{-1}} \right)^{\frac{1}{2}} \approx 3.37\sqrt{Kt} \propto l_T(t). \quad (2.15)$$

Thus, the temperature increase at the surface ($x = 0$) is proportional to the irradiated intensity. Even though the total energy absorbed by the solid is proportional to the time of irradiation, the surface temperature is proportional to the square root of the time, due to the heat flux into the solid. The time the surface is irradiated by a laser is the pulse duration τ_p . Thus, equations 2.14 and 2.15 enable us to judge on the different behavior of the laser processes for the different pulse durations applied in this work.

The light-induced heating will lead to surface melting in the case of sufficiently large laser intensities. For even higher intensities, the material can evaporate leading to material removal. However, additionally to melting and evaporation, the situation might become more complicated due to stress-related effects, liquid-phase expulsion, and ejection of liquid droplets, which also remove material. Additionally, shielding of the laser beam by plasma or vapor may occur, too [87]. For a discussion of these effects please refer to [87] or [92].

2.3.2 Laser-induced forward transfer

The process of light-induced material heating initiating evaporation and, thus, material removal is called direct ablation. However, this process is not very efficient. Experimental data [93] show that a direct ablation of a thin molybdenum film on a glass substrate using an ultrashort laser pulse requires 260 J/mm^3 . If the molybdenum film is irradiated from glass side through this substrate, only 30 J/mm^3 are required. This is even less than the total evaporation enthalpy of 78 J/mm^3 . The latter process is called induced laser ablation [93]. Figure 2.5 schematically shows the two different ablation processes. Since our laser welding process is similar to the indirect ablation, this process is described in the following in detail.

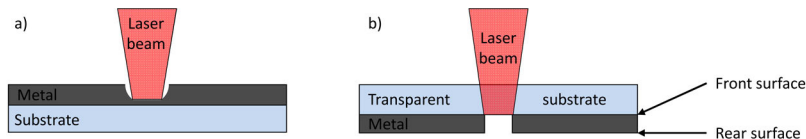


Figure 2.5: Schematics of a) direct and b) induced laser ablation for a metal layer deposited on a substrate transparent for the laser light.

Induced laser ablation is widely used and well investigated for transferring metal layers in a defined manner onto a receiver substrate, called laser-induced forward transfer (LIFT). Adrian et al. [94] describe the ejection of the opaque material from the transparent substrate in four steps:

1. The laser heats the opaque material at the front side, which is in contact with the substrate, until melting starts.
2. This melt front propagates through the opaque layer until the phase front reaches the rear side of the layer.
3. At this time or slightly before the layer is molten through, the front side is superheated or close to its boiling point.
4. The vapor pressure of the opaque material at the front side, i.e., the interface to the glass, propels the molten liquid to the receiver substrate.

This explains why the induced ablation is much more efficient than the direct ablation. Firstly, no energy is released into the open half space due to the evaporation of the material. Secondly, a complete evaporation of the ablated volume is not required since solid or molten material is blown off.

Schultze and Wagner [95] extended this four step model by two different modes for the material blow-off. In the first mode, the layer is molten through at a time τ_{mt} before the evaporation at the front side starts at τ_v . Then, the vapor can expand and blows off the molten layer. In the other mode, the evaporation starts before the melting through ($\tau_v < \tau_{mt}$). Since the material at the front side cannot expand, its temperature further increases and high pressures in the order of the ultimate tensile stress of aluminum (4×10^8 Pa) are generated. This may result in a bursting and ejection of solid material. However, it is still possible that the pressure is not sufficient and that the ejection process starts just after the melt-through, which Schultze und Wagner suggested to be preferred.

2.3.3 Laser welding

The heat generated by the laser irradiation may not only be used for material ablation, but also for laser welding. Welding is a joining technique, where two joining partners directly coalesce, in general by melting and fusing. In comparison to soldering, during welding the joining partners are heated locally in the fusion zone above their melting temperature and no additional materials, like adhesives or solder, are required [53, 54].

Laser welding is the welding technique with the greatest increase of its market share due to a high weld speed, easy automation, and flexibility [96]. It can be classified by the applied intensity in two types [87]:

- Conduction-limited welding: Moderate laser intensities locally melt the material without significant evaporation. The heat transport is dominated by conduction and convection within and around the melt pool.
- Deep-penetration or keyhole welding: Intensive continuous wave (CW) laser light results in local evaporation and forms a deep vapor cavity (keyhole) surrounded by a melt pool. Therefore, keyhole welding can form deep weld seams and reach large aspect-ratios. Multiple reflections and high absorption within the keyhole result in an

efficient welding process.

Even though laser welding is a well proven process in industry, welding of thin sheets is still challenging due to distortion, crack formation, and material drop-out [97–100]. It becomes even more critical when joining thin layers on thermally sensitive substrates like polymer layers or solar cells [101–103], where the heat needs to be applied in a highly controlled manner.

2.3.4 Welding in photovoltaics

A new laser welding process for interconnection of solar cells is developed in this work. However, welding was also used in the past in PV. A short overview is given to set our process into the context of welding in PV. Since the 1970s, welding is an alternative to soldering for interconnection of Si solar cells [10, 104–107]. At that time, parallel gap resistance welding, thermal compression bonding or ultrasonic bonding/welding were investigated. It was pioneered by AEG Telefunken in 1968, who ceased soldering for their array production in 1971 [107], mainly due to the fact that solder joints had a high breakage risk in space application [10]. For space application different tests as for terrestrial applications are used. The weld joints were accelerated aged in 500 thermal cycles ($\approx -200^\circ\text{C}$ to $+100^\circ\text{C}$) and no significant decrease of the mechanical properties was observed [104, 106]. In an undefined peel test, 7 N were measured per interconnector [104]. AEG Telfunken also applied welding for terrestrial application of the PV modules since the 1970s. The solar cells had a Ti/Pd/Ag metallization and the interconnects were silver based [108]. In the 1980s, they used aluminum metallized solar cells and aluminum interconnects⁵. The same technique of ultrasonic bonding drew attention again in the recent years due to the possibility of direct contacting of Al [59] and, thus, avoiding copper or silver. Peel forces of 2 N for 2 mm wide ribbons on the front side of their solar cells are reported. This coincides with the required 1 N/mm in the standards (DIN EN 50461). During artificial aging in 200 temperature cycles, the efficiency of the modules reduced by 6% relative and, thus, more than the limit of 5% according to the IEC61215 standards [59]. Details on the electrical properties are not given.

In the field of laser welding, different processes have been investigated, but only limited publications are available. The Laser Zentrum Hannover (LZH) worked together with the ISFH on a laser welding process for solar cells using Nd:YAG laser with pulse duration in the order of ms [109, 110]⁶. Only limited details relevant for cell interconnection are presented. Electrical contact resistances of one to $10\ \mu\Omega\text{cm}^2$ were achieved. However, the resistances increased by a factor of 5 after 100 thermal cycles⁷ [109]. Details about the behavior after

⁵Information based on modules installed in front of ISFH. The name plates indicates them as modules fabricated by AGE in 1988. The analysis of the interconnects were done by energy dispersive X-ray spectroscopy (EDX) in-house. The modules are in function outdoors until today.

⁶The LZH improved the welding process together with Rofin-Bassel by using a bi-wavelength process [111]. Instead of soldering a Cu ribbon to the cell metallization, it is welded by two overlapped laser beams. One of the lasers emits light at 532 nm and the second at 1064 nm. During the bi-wavelength welding, the green laser (532 nm) with a low efficiency initiates the melting. This decreases the reflectivity of Cu for the IR-light (1064 nm), such that the more efficient IR laser can introduce the high power required for welding into the Cu ribbon.

⁷The thermal cycles are not defined in the paper, but experiments were done at ISFH. The standard thermal cycle at ISFH is between -40°C and 85°C , see section 3.4.7.

the standard test of 200 cycles are not given. The mechanical contact on screen-printed pastes did not fulfill the requirement of 2 N. However, peel forces of 3 to 6 N were reported for evaporated metallizations⁸ [109]. The laser damage was only characterized regarding the failure mode mechanical peel-off test [110]. Analysis about the laser-induced damage on solar cells are not shown to the best of our knowledge.

Another process by Ehrhardt et al. [102] contacts the busbar of GaAs solar cells with a thin silver foil. The Ag foil is ablated using a ns laser until it is thinned down so that the thermal diffusion length l_T is larger than the foil thickness, and a weld spot can be formed. The process benefits from the recoil pressure of the ablated material. The mechanical properties for the Ag-Ag joints were tested in a 0°-peel test [101] instead of the commonly used 180° [56]. The measured shear tension⁹ for this test is 0.62 N/mm². The only reported detail on the electrical properties is the efficiency of the GaAs solar cells. It reduces from 26.4% before interconnection to 25.4% after joining.

⁸The width of the used interconnector ribbon for the peel test is not given. However, ribbons with a width of 2 mm would have been probably used, i.e., the required 2 N coincide with the 1 N/mm as given in the standards.

⁹This would correspond to 0.19 N/mm (0.47 N per 2.5 mm). However, the test conditions have a critical influence on the measurement results [56] and, thus, are not comparable.

3 Experimental conditions of the laser welding process

In the previous chapter 2 we presented the state-of-the-art processes for contacting solar cells by soldering and conductive adhesives, which in general both require surfaces covered with noble metals like silver. Furthermore, the interconnection between the solar cell and the interconnector is commonly formed at elevated temperatures resulting in mechanical stress. As an alternative, we developed the aluminum-based mechanical and electrical laser interconnection (AMELI). Additional to the welding process the samples and the applied analytical methods are presented.

3.1 Laser welding process

Figure 3.1 schematically shows the laser welding process. An Al layer, which serves as interconnect in the module, is attached to a substrate being transparent with respect to the laser light. This enables an easier handling and positioning. The metallic side of the substrate, i.e., the Al layer with thickness d_{su} , is brought in contact with the solar cells' Al metallization, which has a thickness d_{si} . We place the substrate carrying the solar cells on a vacuum chuck so that the transparent substrate is accessible for the laser. The edges are sealed using an adhesion foil. The volume between the substrate and the chuck is evacuated. Thereby, the Al layer on the substrate is pressed onto the solar cell by approximately one bar. We focus the laser on the Al layer on the substrate. The aluminum melts and fuses with the Al metallization of the solar cell and the laser weld spot is formed. Figure 3.2 shows a cross-section of such a weld spot. A close contact between the two layers is important for the welding process, because the molten material should fuse the two Al layers. In the case of a too wide gap, the aluminum can splash into the gap between the surfaces without enabling a contact. By scanning the pulsed laser beam over the surface, both layers form a

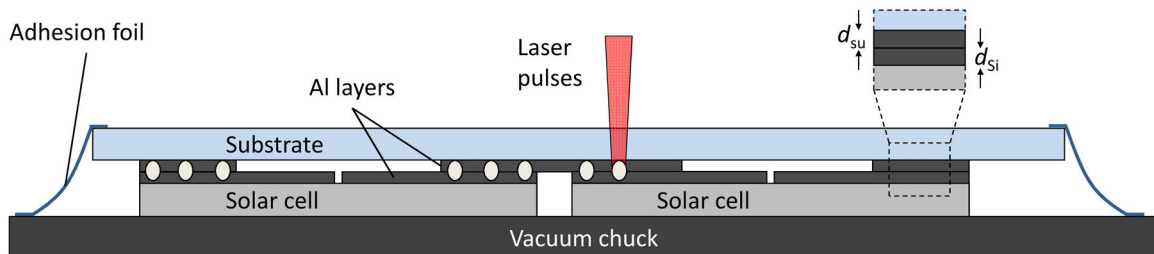


Figure 3.1: Schematic representation of the laser microwelding process used for interconnection of solar cells. In this example two BJBC solar cells are shown. The magnification indicates the thickness of the Al layer on the substrate and on the Si wafer d_{su} and d_{si} , respectively.

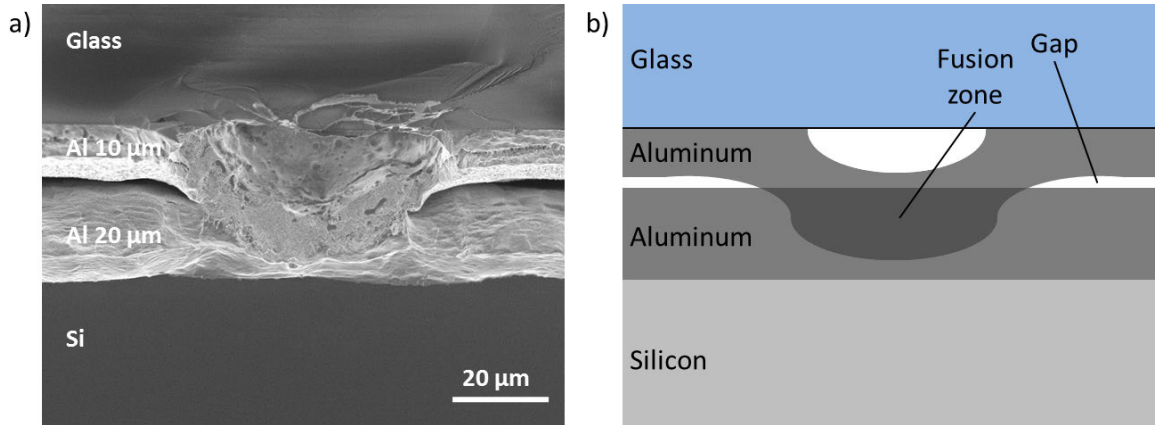


Figure 3.2: a) Scanning electron microscope (SEM) image of a cross-section of a laser weld spot. The weld spot is formed between a 10- μm -thick Al layer, which is evaporated on a glass substrate, and 20 μm of aluminum, which is evaporated on a Si wafer, using with 8 pulses with a pulse duration of 20 ns at 40 J/cm². b) Schematics of the SEM image in a).

mechanically stable and electrically conductive interconnection. In this way the individual Al metallized solar cells are interconnected by laser welding using the Al layer on a substrate as interconnect.

The laser welding is able to break the chemically stable native oxide of aluminum. Since Al layers on the rear side of the BJBC solar cells are only about 10 μm thick, the thermal impact on the underlying Si surface and its passivation must be minimized. This can be achieved by using short laser pulses due to their short thermal diffusion length l_T , see section 2.3.1.

The substrate prevents the evaporation of the irradiated aluminum and the energy transport is directed towards the Al metallization of the solar cell. The energy is kept thereby in the Al layers to form the laser weld. This results in an efficient process combining conduction-limited welding with the benefits of the LIFT process, see section 2.3. Therefore, the substrate is crucial for the AMELI process.

3.2 Laser systems

We use two different laser systems for the laser welding. As discussed in section 2.3.1, the pulse duration has a dominant impact on the thermal processes. Therefore, in this work the nomenclature of the lasers is based on their pulse duration. The first one is a ns laser emitting light in the ultra violet (UV) range and the other system uses a μs laser emitting in the infrared (IR) range. Due to technical issues, we had to replace the μs laser during this work, i.e., μs laser 1 by μs laser 2. The relative motion between the ns laser beam and the working sample is enabled by two linear stages moving the sample. In the case of the μs lasers, a scanner system (HurryScan, Scanlab) deflects the laser beam. The details of the laser systems are given in Tab. 3.1.

We determine the Gaussian radius ω_0 of the laser beam in the focal plane of the optical system by the method of Liu [112]. The Gaussian radius corresponds to the radius r where

Table 3.1: Characteristics of the used laser systems. The pulse duration and wavelength are given by the manufactures, the pulse energy is determined by measuring the average output power divided by the repetition rate, and the Gaussian radius is determined by the method of Liu [112].

Laser as labeled here	Manufacture & type	x-y-motion	Pulse duration τ_p	Central wavelength λ [nm]	Maximum pulse energy E_p [mJ]	Gaussian radius ω_0 [μm]
ns laser	Coherent AviaX	Linear axis	20 ns	355	0.18	17
μs laser 1	Rofin StarCut Disc 100ICQ	Scanner	1.0 μs	1030	3.1	22
μs laser 2	IPG YLP-C-2-1500-15-30	Scanner	1.3 μs	1064	2	42

the fluence F decreases to a value of $1/e^2$. The fluence F in dependence of the radius is

$$F(r) = F_0 e^{-\frac{2r^2}{\omega_0^2}}. \quad (3.1)$$

The the maximum fluence F_0 is related to the pulse energy E_p via

$$F_0 = \frac{2E_p}{\pi\omega_0^2}. \quad (3.2)$$

The method bases on the assumption that material is ablated for fluences higher than a constant ablation threshold F_a . The diameter D of the laser ablated area coincidence with diameter of the laser beam with $F_a = F(\frac{D}{2})$. Thus, the relationship between F_a , D , and ω_0 is given by

$$F_a = F_0 e^{-\frac{D^2}{2\omega_0^2}}. \quad (3.3)$$

Taking the natural logarithm and rewriting the formula results in

$$D^2 = 2\omega_0^2 [\ln(F_0) - \ln(F_a)]. \quad (3.4)$$

Therefore, the square of the diameter is proportional to the logarithm of the maximum fluence, which is proportional to the applied pulse energy. The proportionality factor is $2\omega_0^2$. Figure 3.3 shows an example of a measurement to determine the Gaussian radius for the μs laser 2. Additionally, to the measured values the linear regressions are shown. The green line includes all values above the ablation threshold. The slope is $3493 \pm 194 \mu\text{m}^2$, which corresponds to a Gaussian radius of $42 \pm 10 \mu\text{m}$. The large uncertainty is caused by the uncertainty of the measurement of D and E . In contrast to the behavior of a purely Gaussian beam profile, the slope is not constant on the whole range of the measured values. Therefore, we additional fit the values for low pulse energies up to 0.8 mJ in red. For this regime of E_p the slope is $2149 \pm 331 \mu\text{m}^2$, which corresponds to $\omega_0 = 32 \pm 12 \mu\text{m}$. This is still within the uncertainty of the Gaussian radius determined for the whole pulse energy range. However, we have to assume that the beam is deformed from a perfect Gaussian beam.

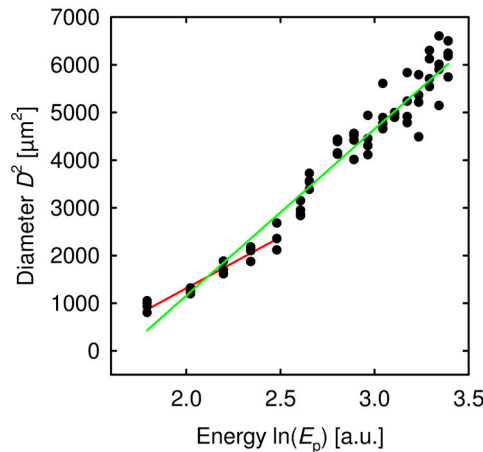


Figure 3.3: Measured values and the corresponding linear regressions for the determination of the Gaussian radius according to Liu [112] in the case of the μs laser 2. In green the linear regression over all measurements is shown, in red for $E_p \leq 0.8 \text{ mJ}$.

3.3 Sample preparation

3.3.1 Substrates

The AMELI process requires for a reliable contacting that the Al layer used as interconnect is attached to a substrate. The substrate has to fulfill the following requirements:

- Bonding or deposition of an Al layer on the substrate must be possible.
- It has to be transparent with respect to the used laser light.
- The substrate must sustain the irradiated laser power and generated heat at the interface to the aluminum layer.
- It should be incorporated in the final module as rear side sealing or as encapsulant.

Therefore, we use substrate materials that are commonly employed in PV and can remain permanently within the module. We evaluate two types of substrates:

- A glass substrate, which we clean in NH_3 and HCl solutions. Aluminum is evaporated by means of physical vapor deposition (PVD) on the glass surface. Unless stated otherwise, we evaporate $10 \mu\text{m}$ Al to one side of the glass. The depositions are done in a high rate in-line metallization system (ATON 500, Applied Materials). We apply a dynamic deposition rate of $5 \mu\text{m} \times \text{m}/\text{min}$ at a tray speed of $1 \text{ m}/\text{min}$ and two oscillations for the $10\text{-}\mu\text{m}$ -thick Al metallization. During this process the glass has to sustain temperatures up to $275 \text{ }^\circ\text{C}$. The glass has to seal the rear side of the module and to be transparent for the laser light. Since the used lasers emit in the wavelength range between 355 and 1064 nm , we choose ultra violet (UV) transparent borosilicate glass (Borofloat, Schott Technical Glasses). This glass type is designed to be resistant to thermal shock [113].
- Alternative suitable substrates are encapsulants (also called lamination foils), which are used to encapsulate the solar cells in the module. Evaporating Al to the encapsu-

lant is not possible, however a thin (about 10 μm) Al foil can thermally be attached to it. This is done by laminating the Al foil to the encapsulant in a laboratory laminator (Icolam, Meier Vakuumtechnik GmbH) at temperatures between 75 $^{\circ}\text{C}$ and 125 $^{\circ}\text{C}$. Due to this process we heat the encapsulant more than once. Therefore, we choose a thermoplastic encapsulant (Tectosil, Wacker Solar). However, encapsulants are transparent for visible and near IR light, but not for UV light. Thus, we can use the encapsulant only for laser welding with the μs lasers.

3.3.2 Silicon samples and solar cells

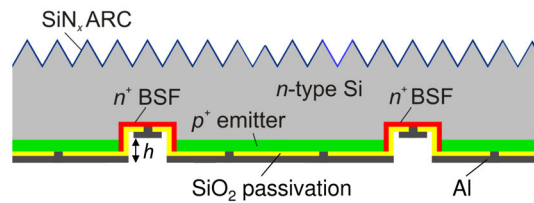


Figure 3.4: Schematic cross-section of the BJBC cell used in this work. h indicates the height difference between base and emitter regions.

In this work we use mono-crystalline silicon wafers. They are cleaned with a cleaning agent solution (Puratron) and damage etched in a KOH solution. We metallize the wafers in the same way as the glass substrates. For the variation of its thickness, we change the tray speed and the number of oscillations, but keep the deposition rate constant at 5 $\mu\text{m} \times \text{m}/\text{min}$.

The wafers receive an additional RCA cleaning¹, when we use them as passivated samples for lifetime tests. Details about the wafer material are given in appendix A.2. We deposit a silicon nitride (SiN_x) layer ($n = 2.4$ at 500 $^{\circ}\text{C}$) of 100-nm-thickness using an industrial SiNA PECVD reactor (Roth & Rau).

The BJBC solar cells interconnected in this thesis were processed and provided by a scientific team working in the same research project², in which we developed the AMELI process. They feature the p - n junction as well as both contacts on the rear side. The emitter is formed in a furnace diffusion step. The definition of the polarities is done by laser ablation and subsequent wet chemical etching [116, 117]. This results in a height difference h between the p - and n -type regions. Then, the back surface field is formed in a second furnace diffusion step. Both polarities are passivated by a silicon dioxide (SiO_x) layer. The contacts of the two polarities are metallized simultaneously with aluminum by PVD. On top of the Al layer we deposit a SiO_x layer, which is porous at the steep flanks between the two polarities. This enables a self-aligned, wet chemical contact separation of the Al layer at these flanks [116, 118]. The front side of the solar cells is texturized and passivated with a SiN_x double layer. For further information regarding these solar cells please refer to [51, 119, 120].

¹Called after the Radio Corporation of America [114, 115].

²Funding by the German Ministry for the Environment, Nature Conservation, and Reactor Safety under contract number 0325192 (CrystalLine Project)

3.4 Characterization techniques

Module integration of the solar cells requires to contact the cells without significant efficiency losses and to ensure the functionality of the solar cells. Therefore, we characterize the laser-welded interconnection regarding the following aspects:

- The mechanical properties of the laser weld spots by evaluating if a sufficient mechanical contact is formed.
- The electrical properties of the interconnection are determined in order to analyze if the resistive losses significantly affect the performance of the solar cells.
- The electronical properties are evaluated on Si test samples, which are passivated on both sides, with respect to the variation of the effective charge carrier lifetime τ_{eff} due to the welding process. The charge carrier lifetime is highly sensitive to damages induced at the passivated Si interfaces or in the Si crystal.

Additionally to the characterization of the weld bonds, we investigate the produced modules regarding:

- Their electrical properties by measuring their I - V -characteristics, which also reveals the efficiency of the module.
- The absence of shunts in the case of finished modules induced for example by unintended contacting of the metallization of both polarities.
- Non-contacted cell areas, i.e., areas where the laser welding failed.
- The longterm stability under accelerated aging test.

3.4.1 Tear-off test

We test the mechanical strength of the laser welds by measuring the force required to separate the two bonding partners from each other. For this purpose, we cut the silicon wafer into circular samples of 25 mm diameter using the μs laser 2 in order to reduce edge effects for tear-off measurements. We weld a circular Si piece to an Al-coated substrate. In order to be able to apply a force, the glass substrate, which is larger than the circular silicon sample, is clamped with a metal plate. We glue a dolly with an epoxy adhesive to the Si sample, see Fig. 3.5. The dolly is then fixed with a plug clutch. To ensure a perpendicular tear-off, the clutch is connected to the lever of the tensile testing machine (Zwick Roell Z0.5) by a steel cord. We determine the mechanical strength of the laser welds by measuring the force perpendicular to the wafer surface.

The force required for separating the circular Si piece from the glass, the tear-off force F_{to} , is measured by the tensile testing machine. The resulting tear-off stress σ is then calculated via

$$\sigma = \frac{F_{\text{to}}}{A_{\text{Si}}} \quad (3.5)$$

with A_{Si} being the area of the circular Si-sample.

Due to experimental conditions, F_{to} can be determined with an accuracy of better than 5 N. This leads to an uncertainty of the tear-off stress σ of less than 10 kPa in the case of

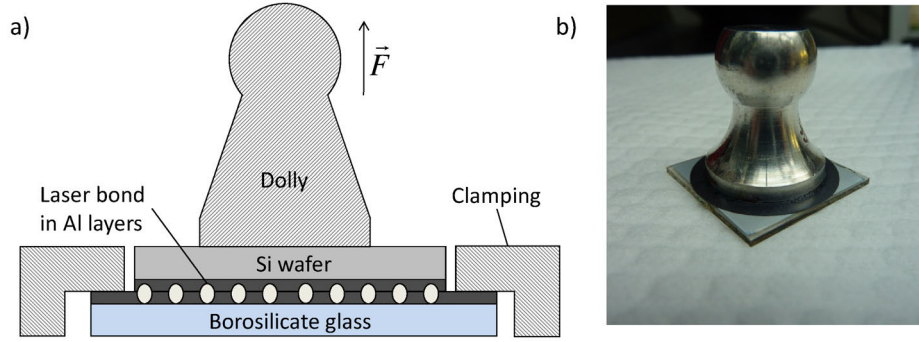


Figure 3.5: Sample for the mechanical tear-off test. a) Schematic cross-section of the test-structure. An aluminum dolly, which can be fixed to the lever of the tensile testing machine, is glued to the sample using an epoxy adhesive. The glass, which is larger than the circular silicon sample, is clamped with a metal plate (hatched clamping). b) Photograph of a prepared sample for tear-off test.

our circular samples with a diameter of 25 mm. For the experiments done with the ns laser, we test three samples for each parameter (the thickness of the Al layer on the Si wafer d_{Si} varied from 1 to 20 μm ; the fluence F between 12 and 40 J/cm^2 , and the number of pulses irradiated in the same spot between one to eight). Since three samples do not allow any relevant statistics, we determine the upper limit of the variation of the tear-off stress by measuring 10 samples for one parameter ($d_{\text{Si}} = 2 \mu\text{m}$; $F = 26 \text{ J}/\text{cm}^2$, single pulses) to be 50%. We assume that the variation is similar for the other parameters. For the μs laser 2, we limit the variation of the number of pulses to single pulses. Therefore, the set of parameters is smaller and five or more samples are tested for each parameter. Due to the larger number of samples for each parameter, the uncertainty is given by the standard variation assuming Gaussian distribution.

Other sources of uncertainty are boundary effects. These may cause that the tear-off process to start from one boundary and, thus, introduce a peel-off like contribution to the separation process. This becomes more critical for example in the case of a slight disturbance of the angle and a not perfectly perpendicular tear-off.

To ensure that the laser interconnected module withstands the handling and other subsequent processes³, we define a lower limit of 25 kPa for tear-off stress. This corresponds to a force of 10 N in the case of a laser-welded area of $2 \times 2 \text{ cm}^2$.

Since the number of welded spots and their area can influence the tear-off stress, we introduce f_w , the area fraction covered by the weld spots:

$$f_w = \frac{\pi \cdot \omega_0^2}{p_w^2}, \quad (3.6)$$

where p_w is the pitch between the weld spots, which are arranged in a squared pattern.

³We test for example screen printing on solar cells contacted by laser welding. For $\sigma = 25 \text{ kPa}$ no detachment is observed.

3.4.2 Electrical resistance measurements

We determine the electrical contact resistivity ρ_c by measuring the voltage drop over two laser-welded interconnections. In order to differentiate the contact resistance from the resistance in the Al layers, we vary the distance between the interconnections. We use a metallized substrate (encapsulant or glass) and structure its Al layer by a laser in $440\ \mu\text{m}$ or $420\ \mu\text{m}$ wide strips, respectively. Figure 3.6 shows photographs of the two structures on lamination foil and glass. We laser weld a Si strip to these Al strips on the substrates. The silicon strips are $940\ \mu\text{m}$ wide in the case of the tests on encapsulant foil and $970\ \mu\text{m}$ wide for glass substrate. They are laser cut out of a metallized wafer. Figure 3.6 b) and e) show the schematics of the structures applied for the measurement of ρ_c and Fig. 3.6 c) and f) cross-sections of the lay-ups.

Using this sample configuration, we measure the resistance for example from point A to point C by four-point-probe measurements (blue dotted line in Fig. 3.6 b)). This is repeated for the different distances d between the Al strips on the substrate.

The measured resistance $R_m(d)$ is given by the contributions of the individual passages that are connected in series:

$$R_m(d) = R_{\text{sub1}} + R_c + R_{\text{Si}}(d) + R_c + R_{\text{sub2}} \quad (3.7)$$

R_{sub1} is the contribution of the Al layer on the lower side of the Si-strip, R_c the contact resistance between the Al layer on the substrate and the Al metallization on the Si strip,

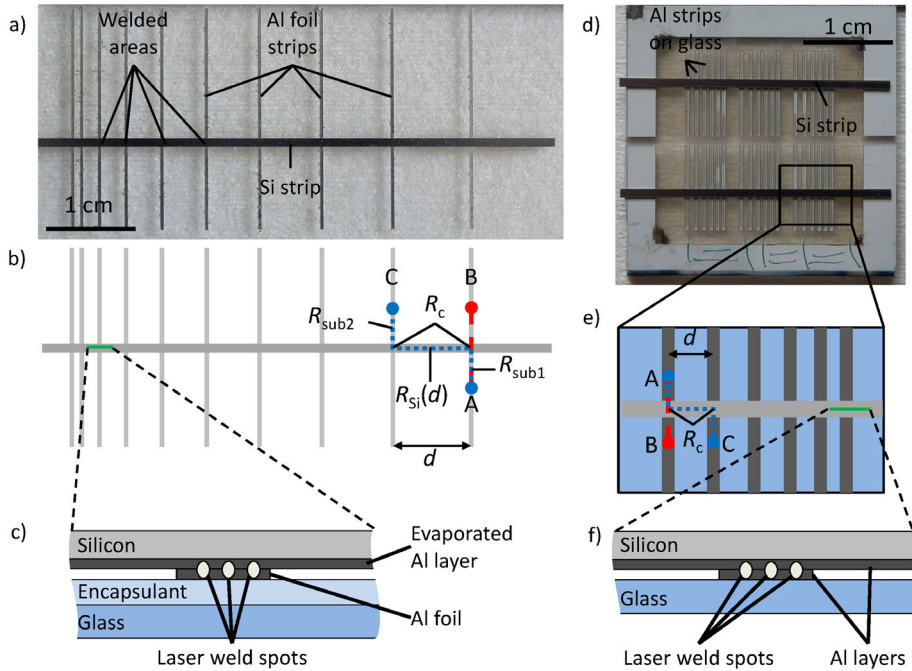


Figure 3.6: Structure for the measurement of the contact resistivity ρ_c on two types of substrates, a) encapsulant and d) glass. b) and e) show the schematics with the contributing resistances, and c) and f) the cross-sections of the structure. The green continuous lines in b) and e) indicate where the cross-sections are located. The points A, B, and C are examples of the locations between which the resistance is measured.

and $R_{\text{sub}2}$ the resistance of the Al layer strip on the other side of the Si strip. The resistance of the Al metallization on the Si $R_{\text{Si}}(d)$ depends on d , which is the distance between the two contacts.

The measured resistance $R_{\text{m}}(d)$ is corrected by the resistance of a single Al layer strip on the substrate measured from the point A to point B, i.e., $R_{\text{sub}1} + R_{\text{sub}2}$ (red dashed line in Fig. 3.6 b)). Therefore, we can reduce equation 3.7 to a corrected resistance

$$R_{\text{cor}}(d) = R_{\text{m}}(d) - (R_{\text{sub}1} + R_{\text{sub}2}) = 2R_{\text{c}} + R_{\text{Si}}(d), \quad (3.8)$$

where $R_{\text{Si}}(d)$ is the product of a constant and the distance d . We determine the contact resistance between the Al layer on the substrate and the Al metallization on the Si R_{c} by plotting $R_{\text{cor}}(d)$ versus the distance d . The intersection of the linear regression of $R_{\text{cor}}(d)$ with the ordinate is then $2R_{\text{c}}$.

3.4.3 Infrared lifetime mapping

The effective charge carrier lifetime τ_{eff} is determined in this work using the dynamic infrared lifetime mapping (ILM), details about this technique are given in [121, 122]. Electrons in the conduction band and holes in valence band (free carriers) excited by visible or near infrared light can absorb and emit photons with energies smaller than the band gap energy E_{gap} . This absorption and also emission is proportional to the density of the free charge carriers n and p . Using an infrared camera this free charge carriers emission is detected. The signal recorded by the camera is

$$S \propto \epsilon(T, \lambda, n, p) \cdot \Phi_{\text{BB}}(T, \lambda) \quad (3.9)$$

with ϵ the emissivity of sample and Φ_{BB} the emitted photon flux of a black body. Since the change of the camera signal is proportional to the change of emissivity and, thus, to the change of the charge carriers $\Delta n = \Delta p$, we can determine the effective charge carrier lifetime from the data analysis of the camera signal in the time domain.

Figure 3.7 shows the schematic of the experimental set-up. Since in thermal equilibrium absorption and emission are in balance, the silicon sample must be heated (here on a hot

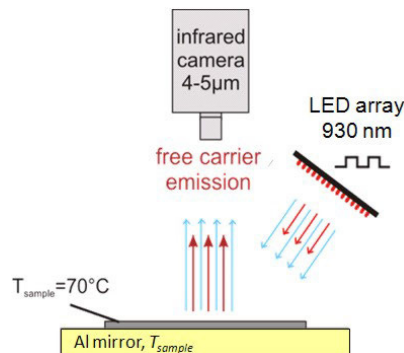


Figure 3.7: Schematic of the infrared lifetime mapping set-up taken from [123]. A near infrared LED array illuminates the sample and generates excess charge carriers. The infrared emission of these free carriers is recorded by the camera.

plate) in order to measure the free carrier emission. An array of light emitting diodes (LED) excites charge carriers within the wafer. The array is periodically switched on and off. The light emitted from the free carriers in the mid infrared is detected by the IR camera. Four images are taken: the first directly when the array is switched on, one when a steady-state under illumination is reached within the wafer, one directly when the array is switched off, and the fourth when steady-state is reached again. A calibration-free lifetime measurement can be performed due to the dynamic approach, i.e., measuring the change of the carrier concentration in the time domain instead of performing steady-state measurements. The signal-to-noise ratio is improved by using a lock-in technique for data processing. Since this is an optical measurement, it can be also applied to single side metallized samples [124], which are employed for the laser welding experiments.

All measurements in this work are done at an illumination level of about 0.3 suns. We measure the samples before and after laser welding to investigate laser-induced damage. In order to determine the variation due to the laser welding process and to distinguish them from the local variation of the material, the normalized effective charge carrier lifetime τ_{norm} is used and calculated via

$$\tau_{\text{norm}} = \frac{\tau_{\text{a}}}{\tau_{\text{b}}} \quad (3.10)$$

with τ_{b} and τ_{a} being the effective charge carrier lifetimes before and after laser micro-welding, respectively.

The measurement uncertainty of the dynamic ILM method is in the range of 10% [124]. Additional uncertainties of the measurements result from spacial misalignment of the evaluation before and after laser welding as well as due to inhomogeneities in the samples' lifetime distribution.

3.4.4 Infrared lock-in thermography

The same set-up as used for the ILM measurements shown in Fig. 3.7 can also be used for infrared lock-in thermography (ILIT) [125, 126] measurements, which we use to detect shunts in solar cells and modules. Again we excite charge carriers by modulated near infrared light. The energy of the excited charge carriers dissipates into heat with a higher rate at local shunts than in the other parts of the solar cell. According to equation 3.9 the camera signal is depended on the temperature of the sample. Using an IR-camera we detect the local change of the temperature by such shunts, instead of detecting the change of the emissivity by charge carriers like in the case of ILM.

The samples, i.e., solar cells or modules, are placed on a plate at room temperature. For the analysis of the shunts the signal detected in steady-state when the array is switched on is corrected by the signal of the steady-state when the array is turned off. Thereby, areas heated by the power dissipation in shunts are identified. The advantage of this method is that these measurements can be performed under open-circuit condition and, thus, without the need to contact the cells or modules to an external power supply. For more details see for example [121, 126].

3.4.5 Camera-based luminescences measurements

For module integration it is of high importance that all parts of the cells are contacted. We use electroluminescence (EL) [127] measurements in order to detect non-contacted cell parts. Charge carriers are injected through the contacts into the solar cell for this measurement technique. These carriers then recombine within the wafer. Among many others, radiative recombination is one possible recombination path. If radiative recombination takes place, photons with an energy close to the band gap energy are emitted and can be detected by a CCD camera. Figure 3.8 shows the experimental set-up.

The intensity of the local luminescence signal is [128, 129]

$$I_{l,i} \propto n \cdot p \propto e^{\frac{qU_i}{k_B T}} \quad (3.11)$$

with q the elementary charge, U_i the local voltage, and k_B the Boltzmann constant. The radiative recombination is less probable than other recombination processes, since in an indirect semiconductor like silicon it is a three-particle process (a hole, an electron, and a phonon). Therefore, other recombination path, for example due to damage of the Si bulk or of the surface passivation, decrease the concentration of charge of electrons and hole, n and p , respectively. As a consequence the luminescence signal intensity decreases locally at such defects. The luminescence signal can be also interpreted from the perspective of the local voltage. Series resistances reducing the voltage lead to a reduction of signal intensity. In the case no contact is formed, no EL signal can be detected. This enables us to localize failed cell interconnections.

Apart from injecting charge carriers by applying an external voltage, they can also be generated by illumination. This method is called photoluminescence (PL) [130]. An homogenized laser beam illuminates the solar cells or modules. Since the charge carries are not injected through the contacts, the signal is unaffected by series resistances. However, it is affected by damages of the silicon bulk or of the surface passivation. Thus, it is a suitable complement to the EL measurements to differentiate between recombination and resistive effects.

For more details about EL and PL see for example [127, 128, 130].

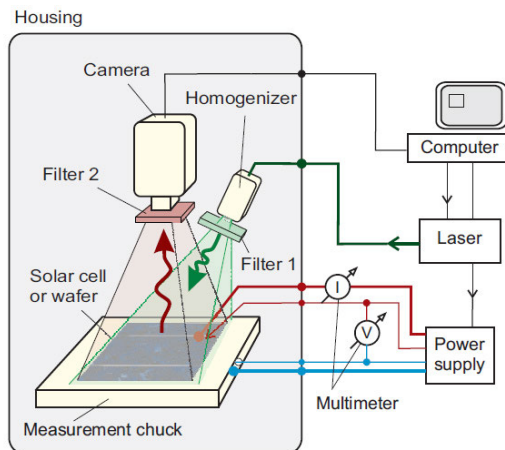


Figure 3.8: Schematic of the set-up for spatially resolved electro- and photoluminescence measurements. Taken from [128]

3.4.6 Light-beam-induced current

Solar cells are typically illuminated uniformly on their whole front-side. In the case of light-beam-induced current (LBIC) [131], the solar cell is illuminated spot wise in order to access the information on the local current generation under I_{sc} condition. We gain an image of the space resolved current generation by scanning the surface of a solar cell. Location of defects that decrease the local photo current are identified and their impact quantified by this method.

The excitation can be done with a spot of white light or with monochromatic light, e.g., laser beams, to obtain additional information about the local quantum efficiency. For silicon the optical penetration depth is highly dependent on the wavelength. Therefore, one obtains information about the depth dependent carrier generation and collection using light at different wavelength. Thus, mappings of the local external quantum efficiency are obtained. If additionally the local reflectance is measured the local internal quantum efficiency can be calculated. The system used in this thesis (LOANA, pv-tools GmbH) has six discrete wavelength 405 nm, 532 nm, 670 nm, 830 nm, 925 nm, and 980 nm. The spot size is about 100 μm . For further information about LBIC see for example [131–134].

3.4.7 Accelerated aging

Accelerated aging tests based on the IEC norm 61215 [135] are performed in order to investigate failures within the modules due to chemical processes or fatigue. In general, the different test sequences consist of 1) 200 thermal cycles (-40°C to 85°C), 2) 1000 hours of damped heat (85°C and 85% rel. humidity), and 3) 10 humidity-freeze cycles (-40°C with humidity control to $+85^\circ\text{C}$ with 85% rel. humidity). In our laboratory we use a test sequence that combines the three tests in one. It consists of the humidity-freeze test with a reduced humid time of 6 hours instead of 20 hours. Figure 3.9 shows the humidity-freeze cycles used at ISFH (black lines) and the one according to the standards (red dotted line). After 200 cycles of this test the required 200 thermal cycles, 1000 h of damped heat, and the humidity-freeze test are completed. By this, one can rapidly reveal and understand failures due to chemical reactions, like corrosion, or thermal-mechanical cycling, like fatigue of interconnections, under humid conditions.

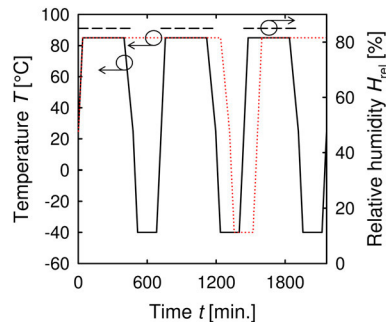


Figure 3.9: Humidity-freeze cycles used at ISFH and the one according to the standards IEC norm 61215. The solid black line and the dotted red line show the temperature profile of the humidity-freeze cycles used at ISFH and an example of a cycle according to the standards, respectively. The humidity is controlled at 85% relative for temperatures above 25°C , as shown exemplary for the ISFH cycles as dashed black line. Below 25°C the relative humidity is not controlled.

4 Experimental results of the laser welding

In this chapter, the analysis of the laser weld joints' properties are presented. The set of laser parameters applicable for laser welding is limited on the one hand for low laser fluences by the mechanical contact. If the fluence is too small, no mechanical contact is formed. On the other hand, the Si surface underneath the metal layer is damaged, if we use too high laser fluences. A decrease of the effective charge carrier lifetime τ_{eff} therefore defines the upper limit of the fluence. These two limits enclose the process window and, thus, are presented together. A low electrical contact resistivity is also required for cell interconnection, which is presented separately.

4.1 Laser welding on glass substrates by the ns laser

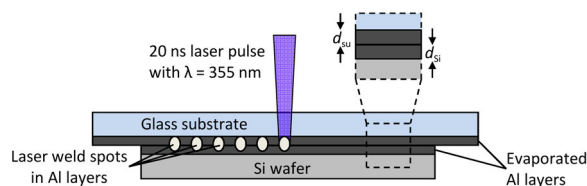


Figure 4.1: Schematic representation of the laser welding experiments in this section. The magnification indicates the thickness of the Al layer on the glass substrate and on the Si wafer d_{su} and d_{si} , respectively.

As described in section 3.2, we use laser pulses with durations in the range of ns and μs for laser welding. In the following, we start with the results of the ns laser system since one expects less thermal impact due to the shorter thermal diffusion length. In order to limit the number of parameters, we start with constant laser parameters to determine a suitable Al layer thickness d_{su} on the substrate. With this thickness we, investigate the process limits for various Al layer thicknesses d_{si} on the silicon wafer. Table 4.1 gives an overview of the experimental conditions in this section and Fig. 4.1 a schematic of the weld experiments. Wafer without surface passivation are used for mechanical tests, whereas we use passivated samples for lifetime experiments, see section 3.3.2.

4.1.1 Mechanical properties and laser-induced damage

Variation of Al layer thickness on the glass substrate

As a starting point for the analysis of lower and upper fluence limits, we take an Al layer thickness of $d_{\text{si}} = 20 \mu\text{m}$ on the silicon samples. This thickness corresponds to the lower limit of the metallization thickness in the case of 5" BJBC solar cells with two busbars

Table 4.1: Overview of the parameters that we vary or keep constant during the experiments in this section. The numeric values are given for constant parameters. In experiment 1 we evaluate the mechanical properties in dependence on d_{su} , in experiment 2 the limits for the laser welding process for various laser parameters in dependence on d_{Si} are determined, and in experiment 3 we measure the electrical properties of the weld spots.

Experiment	Laser system	Substrate type	Al	Al	Number of pulses	Fluence	Welded area fraction
			thickness on substrate	thickness on Si wafer			
			d_{su} [μm]	d_{Si} [μm]		F [J/cm^2]	f_{w} [%]
1	ns laser	glass	varied	20	8	40	0.4
2	ns laser	glass	10	varied	varied	varied	0.4
3	ns laser	glass	10	20	8	40	2

[51, 52]. We investigate the influence of the aluminum layer thickness on the glass substrate d_{su} by measuring the mechanical properties of the laser weld spots. We keep the laser parameters constant at eight pulses with a fluence of $40 \text{ J}/\text{cm}^2$.

Figure 4.2 a) shows an example of a mechanical measurement using the tensile testing machine. The machine measures the force F in dependence of the displacement of its cantilever. Here, the displacement corresponds mainly to the elongation of the steel cord used to connect the clutch to the cantilever, see section 3.4.1. The force increases up to the failure of the laser welds, when the force decreases abruptly. The maximum force corresponds to the tear-off force F_{to} of the welded interconnection, which we use to determine the tear-off stress according to equation 3.5.

Figure 4.2 b) shows the dependence of the mechanical tear-off stress on d_{su} . The tear-off stress increases up to $d_{\text{su}} = 10 \mu\text{m}$, where a maximum tear-off stress of 303 kPa is achieved. Increasing the thickness d_{su} further to $20 \mu\text{m}$ leads to a decrease of the tear-off stress to $\sigma = 107 \text{ kPa}$. Thus, for this laser parameters, $d_{\text{su}} = 10 \mu\text{m}$ leads to the strongest mechanical

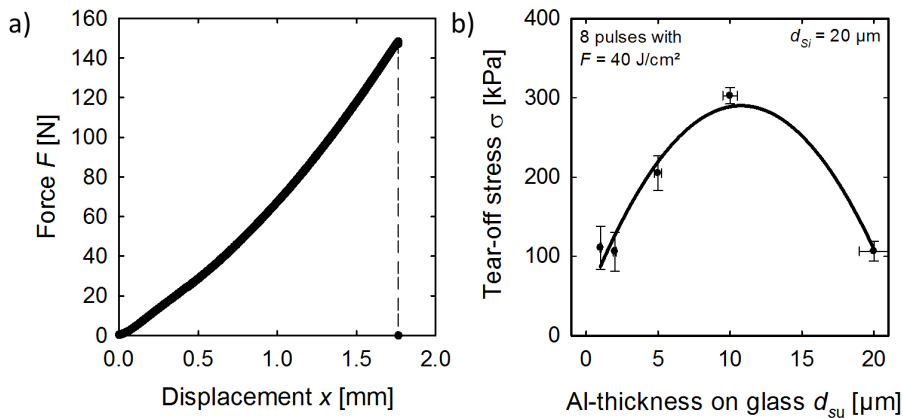


Figure 4.2: a) Example of a measurement for the tear-off force F_{to} for a laser-welded interconnection using $d_{\text{Si}} = 20 \mu\text{m}$, $d_{\text{su}} = 10 \mu\text{m}$, and eight pulses with $40 \text{ J}/\text{cm}^2$. b) Tear-off stress σ in dependence of the Al thickness on glass d_{su} for the ns laser. The metallization on the wafer is constantly $d_{\text{Si}} = 20 \mu\text{m}$ as well as the laser parameters of eight pulses with $40 \text{ J}/\text{cm}^2$. The line is a guide to the eye. Table 4.1, experiment 1 summarizes the experimental details.

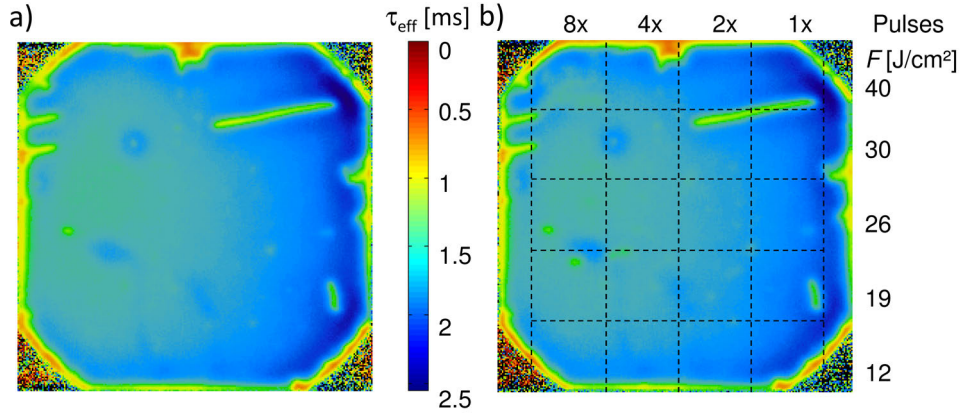


Figure 4.3: Dynamic ILM images of Al-coated lifetime samples with $d_{\text{Si}} = 20 \mu\text{m}$ a) before and b) after laser welding to a glass substrate ($d_{\text{su}} = 10 \mu\text{m}$) using various parameters for the ns laser. The dashed lines indicate the matrix of the laser parameters. Table 4.1, experiment 2 summarizes the experimental details.

contact and in the following, all experiments are performed with $d_{\text{su}} = 10 \mu\text{m}$, which is also a reasonable thickness for the interconnection of solar cells, see appendix A.3.

Variation of Al layer thickness on the silicon samples

Figure 4.3 shows a dynamic ILM image of a passivated silicon sample with $d_{\text{Si}} = 20 \mu\text{m}$ before and after laser welding to a glass substrate with $d_{\text{su}} = 10 \mu\text{m}$ using one to eight laser pulses with fluences between $12 \text{ J}/\text{cm}^2$ and $40 \text{ J}/\text{cm}^2$. Qualitatively, no variation of the lifetime before and after laser welding is observed. Figure 4.4 a) gives the quantitative analysis of the resulting normalized effective charge carrier lifetimes τ_{norm} . It varies between

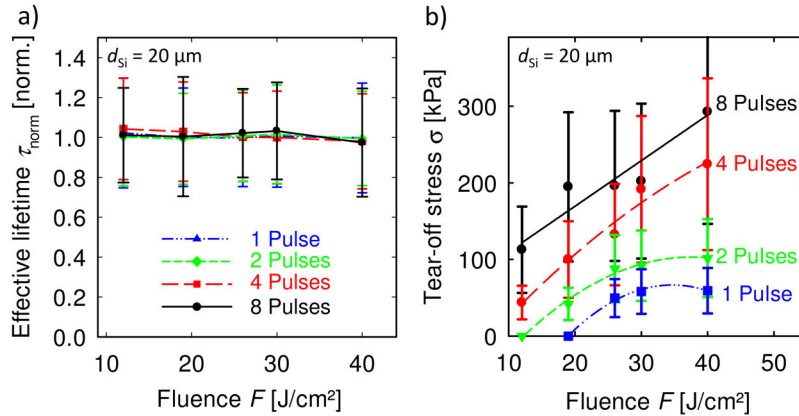


Figure 4.4: a) Quantitative evaluation of the dynamic ILM images in Fig. 4.3, the normalized effective charge carrier lifetimes τ_{norm} in dependence on the laser fluence. The metallized lifetime samples with $d_{\text{Si}} = 20 \mu\text{m}$ are welded to a metallized glass substrate with $d_{\text{su}} = 10 \mu\text{m}$. The lifetimes after laser welding τ_{a} are normalized by the charge carrier lifetimes before laser welding τ_{b} and averaged over the area covered by weld spots for each laser parameter. b) The corresponding tear-off stress σ is shown for the same set of laser parameters. The lines in both images are guides to the eye. Table 4.1, experiment 2 summarizes the experimental details.

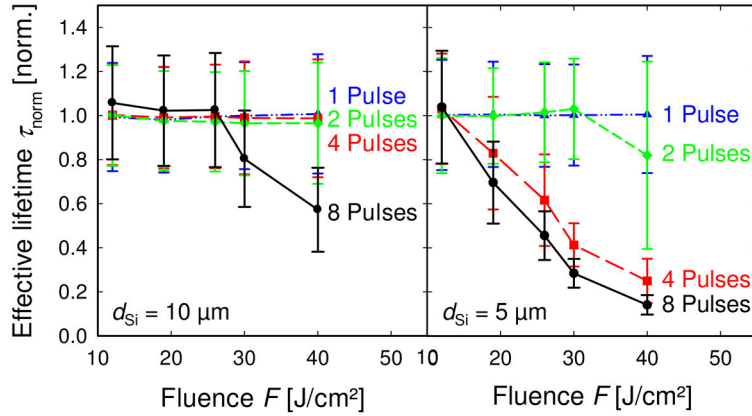


Figure 4.5: The normalized effective charge carrier lifetimes τ_{norm} in dependence on the laser fluence. A metallized lifetime sample with $d_{\text{Si}} = 5 \mu\text{m}$ and $10 \mu\text{m}$ is laser welded to a metallized glass substrate. The lines in both images are guides to the eye. Table 4.1, experiment 2 summarizes the experimental details.

0.97 ± 0.27 and 1.04 ± 0.25 , i.e., no significant degradation of the lifetime for the given set of laser parameters can be detected. Figure 4.4 b) shows the mechanical tear-off stress σ for the same set of laser parameters. The results of the mechanical tear-off and the qualitative results of the lifetime are also entered in Tab. 4.2 for comparison to other Al layer thicknesses. The tear-off stress increases with increasing laser fluence F as well as with increasing number of pulses irradiated at the same spot. No detectable mechanical contact is achieved for single pulses with a fluence of 12 J/cm^2 and 19 J/cm^2 and two pulses with 12 J/cm^2 . The maximum tear-off stress of 293 kPa is achieved with eight pulses at a fluence $F = 40 \text{ J/cm}^2$.

We perform the same investigations for Al layer thicknesses between $1 \mu\text{m}$ and $10 \mu\text{m}$ and for non-metallized wafers. Figure 4.5 shows the normalized effective charge carrier lifetimes τ_{norm} in dependence on the laser parameters for $d_{\text{Si}} = 5 \mu\text{m}$ and $10 \mu\text{m}$. In the case of $d_{\text{Si}} = 10 \mu\text{m}$, the welding process induces damage only for eight pulses and fluences above 26 J/cm^2 . For the undamaged areas, where τ_{norm} is between 0.97 and 1.06 , we achieve the maximum tear-off stress $\sigma = 240 \pm 120 \text{ kPa}$ for four laser pulses with $F = 40 \text{ J/cm}^2$.

For $d_{\text{Si}} = 5 \mu\text{m}$, four to eight pulses with fluences above 12 J/cm^2 as well as two pulses with more than 30 J/cm^2 induce laser damage. The other laser parameters lead to a normalized effective lifetime τ_{norm} between 1.00 and 1.04 . As shown in Tab. 4.2, we measure the highest mechanical tear-off stress $\sigma = 48 \pm 24$ and $52 \pm 26 \text{ kPa}$ and no significant damage induced for single pulses with 40 J/cm^2 and two pulses with 30 J/cm^2 , respectively.

The tendency that for thinner Al layers on the Si wafer less pulses with higher fluence lead to the highest tear-off stress without measuring laser damage holds also for $2 \mu\text{m}$ and $1 \mu\text{m}$, see Tab. 4.2. In the case of $2 \mu\text{m}$, no damage is observed (here $\tau_{\text{norm}} = 1.01 - 1.10$) for one to four pulses with fluences of 12 J/cm^2 as well as for two pulses with $F = 19 \text{ J/cm}^2$ and single pulses with up to 40 J/cm^2 . Out of these, the last one leads to the highest mechanical tear-off stress $\sigma = 64 \pm 32 \text{ kPa}$.

For $1 \mu\text{m}$, the same parameters can be used as for $2 \mu\text{m}$. Except for single pulses with 40 J/cm^2 , which does not lead to a significant change in τ_{norm} , but inhomogeneities can be observed in the ILM images. Single pulses with 30 J/cm^2 and 40 J/cm^2 lead to tear-off stresses $\sigma = 39 \pm 20$ and $59 \pm 30 \text{ kPa}$, respectively.

Table 4.2: Overview of tear-off stresses σ for Al layer thickness on the Si wafer between 20 μm and 1 μm and for non-metallized wafers. For each thickness d_{Si} we varied the laser parameters between one to eight pulses (rows) and fluences between 12 J/cm^2 and 40 J/cm^2 (columns). The numerical values correspond to the tear-off stresses and the color indicates if we detect laser-induced damage on the lifetime samples (red: laser damages detected, green: no laser damage detected), see for example Fig. 4.4 and Fig. 4.5. The uncertainty of the tear-off stresses is below 50%, see section 3.4.1. If no entry is given, the measurement is not possible or not performed. Table 4.1, experiment 2 summarizes the experimental details.

	$d_{\text{Si}} = 20 \mu\text{m}$				$d_{\text{Si}} = 10 \mu\text{m}$			
$F [\text{J}/\text{cm}^2]$	8	4	2	1	8	4	2	1
40	293	224	102	59	196	240	64	50
30	202	191	92	58	196	99	58	46
26	196	132	88	50	162	67	25	11
19	195	100	42	0			28	2
12	113	44	0				0	0
	$d_{\text{Si}} = 5 \mu\text{m}$				$d_{\text{Si}} = 2 \mu\text{m}$			
$F [\text{J}/\text{cm}^2]$	8	4	2	1	8	4	2	1
40			56	48			76	64
30			52	19			70	39
26			33	3			49	15
19		33	20	0		46	28	8
12	42	14	0	0	37	10	0	0
	$d_{\text{Si}} = 1 \mu\text{m}$				no Al			
$F [\text{J}/\text{cm}^2]$	8	4	2	1	8	4	2	1
40			77	59			25	49
30			62	39			23	23
26			36	4			14	9
19		37	29	1		15	9	0
12	45	7	0	0		4	1	0

In the case of non-metallized wafers ($d_{\text{Si}} = 0 \mu\text{m}$), only single pulses with 12 J/cm^2 and 19 J/cm^2 and two pulses with 12 J/cm^2 do not result in detectable laser damage, see Tab. 4.2. However, these three parameters do not form a detectable mechanical contact. We conclude that a damage-free laser joining of non-metallized wafer is not possible for the used conditions.

These analysis as summarized in Tab. 4.2 show that laser welding is possible down to single micrometer of Al layer thickness on the Si wafer. For Al layers with thicknesses between 5 μm and 20 μm , we determine suitable process windows including a range of laser fluences up to the maximum fluence of the laser system of 40 J/cm^2 and using multiple pulses. For thin layers ($d_{\text{Si}} < 5 \mu\text{m}$), the highest tear-off stress without inducing detectable laser damage is achieved with single pulses and a fluence of 40 J/cm^2 . However, an Al layer is required for welding without inducing detectable laser damage as shown by the results of no aluminum on the samples.

Figure 4.6 shows the tear-off stress σ in dependence on the Al layer thickness d_{Si} on the silicon for single pulses. Within the uncertainty of the measurement, no dependence on the

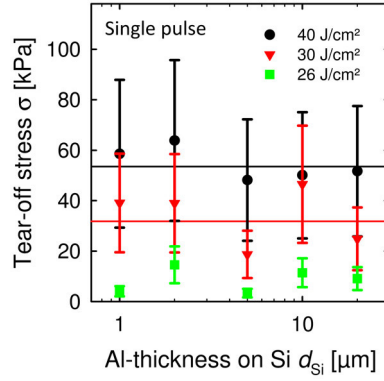


Figure 4.6: Mechanical tear-off stress σ in dependence of the Al thickness on d_{Si} on the Si wafer from 1 to 20 μm for single pulses. The lines are the averages over all thicknesses. Table 4.1, experiment 2 summarizes the experimental details.

Al layer thickness d_{Si} can be observed. The average tear-off stress for all thicknesses and $F = 40 \text{ J}/\text{cm}^2$ is 54 kPa. This is more than two times the limiting tear-off stress of 25 kPa, see section 3.4.1. In the case of a fluence of $30 \text{ J}/\text{cm}^2$, it is reduced to 32 kPa and for $F = 26 \text{ J}/\text{cm}^2$ no reliable contacting is possible. For some laser parameters that lead to no detectable degradation of the wafer lifetime, the mechanical contact is determined by the thickness of the Al layer on the substrate and independent on the layer thickness on the wafer.

4.1.2 Electrical properties

The laser weld spot should also result in a low electrical contact resistance. Preliminary experiments, see appendix A.4, show that if there is a mechanical contact, the electrical contact resistivity is low. In order to determine the contact resistivity ρ_c quantitatively, we use a test structure as described in section 3.4.2.

Figure 4.7 shows the results of the measurements for the electrical contact resistance. As shown in Figure 3.6 d) there are 18 Al strips on the glass substrates. More than 108 measurements of the different combinations of the strips, i.e., different locations for the points A, B, and C in Figure 3.6 b), are done. Due to the uncertainty of the measurement, which for example is caused by the variation of the contact resistance between the measurement needles and the Al layer or slight variations of their position on the Al strips, only an upper limit of the contact resistance can be determined. In the case of the ns laser, the Al layer thickness on silicon d_{Si} is 20 μm and the laser-welded area fraction f_w is about 2%. We use eight pulses and $40 \text{ J}/\text{cm}^2$ for the interconnection. The intersection with the y-axis of the linear regression corresponds, according to Equation 3.8, to twice the contact resistance R_c . We determine R_c to be smaller than 1 m Ω . The intersection area of the metallized silicon strip and the Al strips on glass is $970 \times 440 \mu\text{m}^2$. Taking into account the total intersection area and not only the laser-welded area, this results in a contact resistivity of ρ_c below 5 $\mu\Omega\text{cm}^2$. This resistivity is close to ρ_c of laser solder joints, which reach contact resistances in the order of 10 $\mu\Omega\text{cm}^2$ and an order of magnitude below standard contact solder joints ($\rho_c \approx 50 - 100 \mu\Omega\text{cm}^2$) [55].

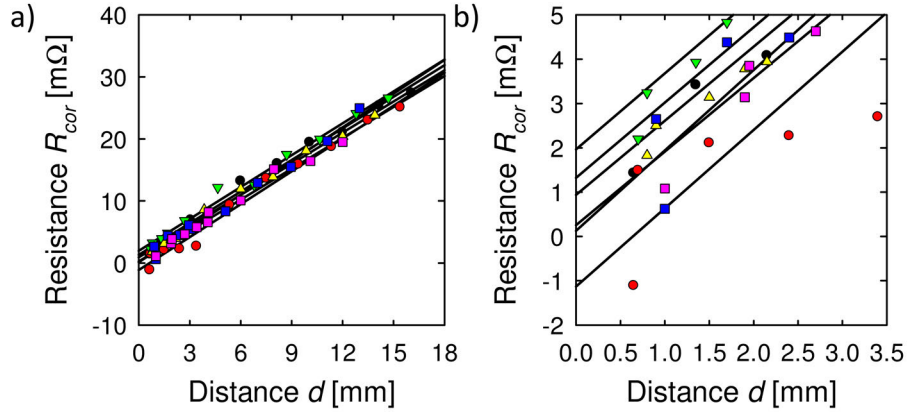


Figure 4.7: Corrected measured resistance $R_{\text{cor}}(d)$ versus the distance d separating the Al strips on the glass substrate in the case of the ns laser with eight pulses and 40 J/cm^2 , an Al layer thickness on silicon $d_{\text{Si}} = 20 \mu\text{m}$, and a laser-welded area f_w about 2%. The different symbols correspond to the different sets of measurements and the solid lines are the corresponding linear regressions. b) is a magnification of the measurements shown in a). Table 4.1, experiment 3 summarizes the experimental details.

4.2 Laser welding on glass substrates by the μs laser

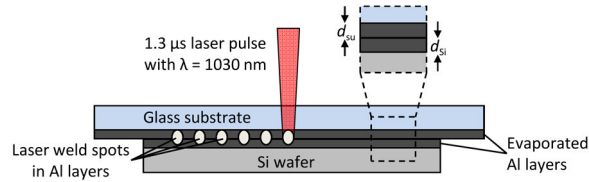


Figure 4.8: Schematic representation of the laser welding experiments in this section. The magnification indicates the thickness of the Al layer on the glass substrate and on the Si wafer d_{su} and d_{si} , respectively.

The μs laser reaches higher fluences compared to the ns laser. Therefore, we limit the experiments to single pulses, which show the best results in the case of the ns laser, especially for thin layer thicknesses. Additional to investigations on lifetime samples, we compare this results to an application on solar cells. The details of the experimental conditions are summarized in Tab. 4.3 and Fig. 4.8 shows a schematics of the weld experiments.

4.2.1 Mechanical properties and laser-induced damage

Figure 4.9 a) shows the normalized effective lifetime τ_{norm} versus the laser fluence for various thicknesses d_{Si} between $1 \mu\text{m}$ and $20 \mu\text{m}$. The normalized lifetimes τ_{norm} are constantly at 1 until a certain threshold. We call this threshold the maximum fluence F_{max} , up to which $\tau_{\text{norm}} \geq 0.95$ and above which the normalized lifetimes decrease with increasing fluence F . We expect up to F_{max} no surface damage and above this threshold a damage of the passivation layer.

Figure 4.9 b) shows the maximum fluence F_{max} in dependence on the thickness d_{Si} . It increases with increasing Al layer thickness on the silicon d_{Si} . The same graph also shows

Table 4.3: Overview of the parameters that we vary or keep constant during the experiments in this section. The numeric values are given for constant parameters. In experiment 1 the limits of the laser welding process for various Al layer thicknesses on Si are determined, in experiment 2 we apply the laser process to solar cells with highly doped rear side, and in experiment 3 and 4 we measure the electrical properties of the weld spots.

Experiment	Laser system	Substrate type	Al thickness on substrate	Al thickness on Si wafer	Number of pulses	Fluence	Welded area fraction
			$d_{\text{su}} [\mu\text{m}]$	$d_{\text{Si}} [\mu\text{m}]$		$F [\text{J}/\text{cm}^2]$	$f_w [\%]$
1	μs laser 2	glass	10	varied	1	varied	6
2	μs laser 2	glass	10	2.5	1	varied	6
3	μs laser 2	glass	10	10	1	44	20
3	μs laser 2	glass	10	2	1	36	20

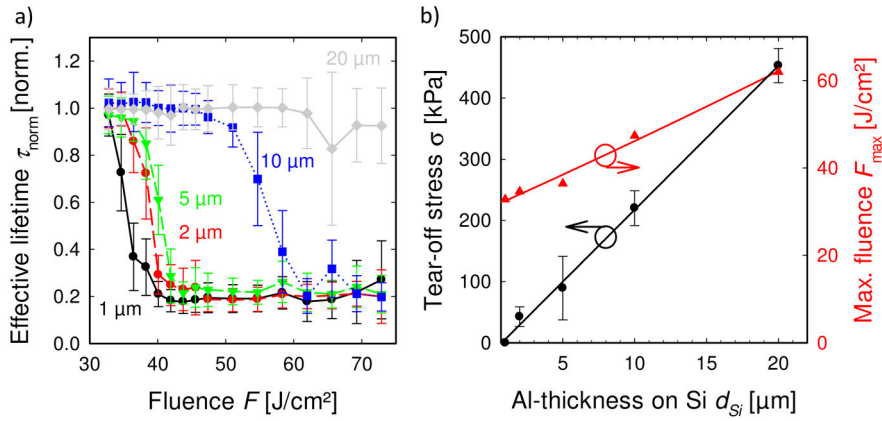


Figure 4.9: a) The normalized effective charge carrier lifetimes τ_{norm} in dependence on the laser fluence for various thicknesses of the Al layer on the silicon d_{Si} between 1 μm and 20 μm in the case of the μs laser 2. b) The resultant maximal fluence, which can be applied without damage, and the corresponding mechanical tear-off stress σ in dependence on the Al thickness on the silicon d_{Si} from 1 to 20 μm . Table 4.3, experiment 1 summarizes the experimental details.

the perpendicular tear-off stress σ for the corresponding thicknesses d_{Si} and the fluence¹ F_{max} . Here, the area fraction covered by the laser spots is about $f_w = 6\%$. In the case of thicker layers, higher fluences can be applied and lead to higher mechanical strengths of the laser weld spots. The maximum tear-off stress of 450 ± 30 kPa is determined in the case of $d_{\text{Si}} = 20 \mu\text{m}$ using a fluence $F = 62 \text{ J}/\text{cm}^2$. In the case of $d_{\text{Si}} = 2 \mu\text{m}$, a fluence $F = 35 \text{ J}/\text{cm}^2$ can be applied for damage-free laser welding resulting in a perpendicular tear-off stress of 43 ± 16 kPa, which is above the limiting tear-off stress of 25 kPa, see section 3.4.1. A fluence of up to $33 \text{ J}/\text{cm}^2$ can be applied in the case of $d_{\text{Si}} = 1 \mu\text{m}$. However, this parameter leads to mechanical tear-off stress that is too low to be measured with our set-up and, thus, is

¹Since the fluence variation used for the mechanical test is less finely resolved (e.g. for $d_{\text{Si}} = 10 \mu\text{m}$ $\Delta F = 7 \text{ J}/\text{cm}^2$) compared to the lifetime experiment (e.g. for $d_{\text{Si}} = 10 \mu\text{m}$ $\Delta F = 1.8 - 3.6 \text{ J}/\text{cm}^2$) close to F_{max} , the depicted tear-off stresses correspond to fluences slightly below the maximum fluence d_{Si} of 10 μm and 20 μm . For $d_{\text{Si}} = 10 \mu\text{m}$, $F_{\text{max}} = 47 \text{ J}/\text{cm}^2$ and the tear-off stress is determined at $F = 44 \text{ J}/\text{cm}^2$. For $d_{\text{Si}} = 20 \mu\text{m}$, $F_{\text{max}} = 58 \text{ J}/\text{cm}^2$ and the tear-off stress is determined at $F = 58 \text{ J}/\text{cm}^2$.

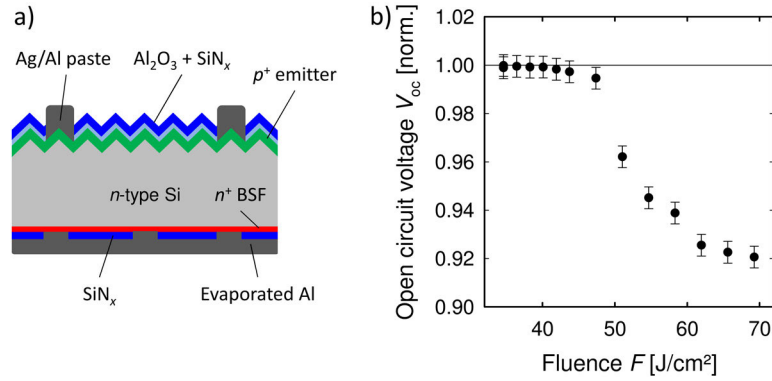


Figure 4.10: a) Schematics of the PERT solar cells with a BSF formed by ion implantation. Taken from the presentation to [137]. b) Open-circuit voltage V_{oc} of PERT solar cells with $d_{Si} = 2.5 \mu\text{m}$ after laser welding to a glass metallized with $10 \mu\text{m}$ aluminum normalized by the open-circuit voltage before welding. The given uncertainty is the measurement uncertainty of the I - V -tester within the LOANA system. Table 4.3, experiment 2 summarizes the experimental details.

not sufficient to form mechanical reliable weld spots. Hence, we can contact solar cells with a metallization thickness down to $d_{Si} = 2 \mu\text{m}$ in the case of $10 \mu\text{m}$ Al on the substrate.

4.2.2 Test of process limits on solar cells

In order to test this limit on cell structures, we apply the process to passivated emitter, rear totally-diffused (PERT) solar cells [136, 137], see Fig. 4.10 a). This enables us to compare the results gained on lifetime samples to samples with a highly doped layer underneath the passivation and to detect the impact of the laser damage on the device performance. Such structures are closer to the BJBC solar cells, which we aim to interconnect, than the lifetime samples. However, such bifacially contacted cells have only one polarity on the rear side so that other challenges, for example due to misalignment of the weld spots, are avoided. The PERT solar cells used for these experiments have a BSF formed by ion implantation. The cells are metallized using PVD with $2.5 \mu\text{m}$ Al on the rear side and laser diced in pieces of $20 \times 20 \text{mm}^2$ using the ns laser. A damaging of the passivation on the rear side would result in a reduction of the open-circuit voltage V_{oc} . The open-circuit voltages of the diced solar cells before interconnection are within the range of 647.7mV and 652.3mV for all cells. Figure 4.10 b) shows the open-circuit voltage of the solar cells after laser welding normalized by the open-circuit voltage before welding. A tendency of a reduced open-circuit voltage

Table 4.4: I - V -parameters of PERT solar cells with measurement uncertainty measured under standard testing conditions (100mW/cm^2 , 25°C) before and after contacting by laser welding with 35J/cm^2 . Abbreviations used: Cell area A , efficiency η , fill factor FF, open-circuit voltage V_{oc} , and short-circuit current density J_{sc} .

	A [cm ²]	η [%]	FF [%]	V_{oc} [mV]	J_{sc} [mA/cm ²]
Before	4	18.8 ± 0.6	74.2 ± 0.8	648 ± 3	39.2 ± 1.1
After	4	18.9 ± 0.6	74.0 ± 0.8	648 ± 3	39.4 ± 1.1

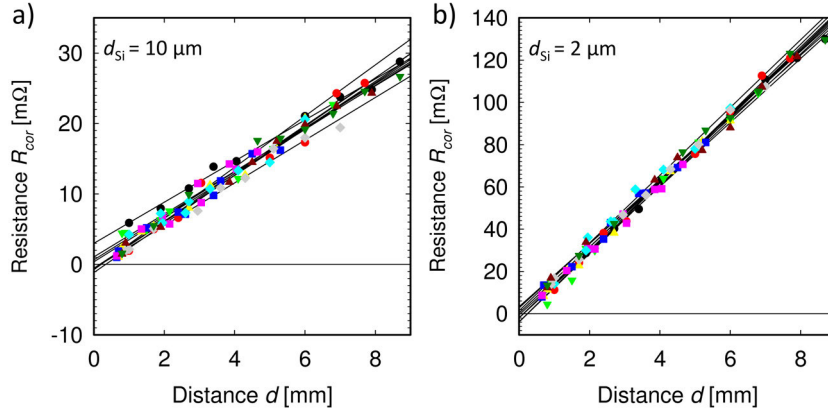


Figure 4.11: Corrected measured resistance $R_{\text{cor}}(d)$ versus the distance d separating the Al strips on the glass substrate with $d_{\text{Si}} = 10 \mu\text{m}$ using the μs laser 2 a) for $d_{\text{Si}} = 10 \mu\text{m}$ and a fluence of 44 J/cm^2 and b) for $d_{\text{Si}} = 2 \mu\text{m}$ and 36 J/cm^2 . The laser-welded area f_w is about 20%. The different symbols correspond to the different sets of measurements and the solid lines are the corresponding linear regressions. Table 4.3, experiments 3 and 4 summarize the experimental details.

is observable above 40 J/cm^2 , which is significantly more than the limit determined by the lifetime samples of 35 J/cm^2 and 36 J/cm^2 for d_{Si} of $2 \mu\text{m}$ and $5 \mu\text{m}$, respectively. A significant reduction of the open-circuit voltage can be observed starting from 47 J/cm^2 . This shows that the evaluation with the lifetime samples is more sensitive with respect to laser-induced surface damage compared to solar cells with a highly doped layer (here an ion-implanted BSF) underneath the passivation. Therefore, the evaluation using the lifetime samples is a sensitive and conservative estimation of the process limits of the laser welding. No degradation of the cell performance is expected when applying these parameters for interconnection of solar cells. The different behavior for solar cells and lifetime samples is caused by the BSF layer. The doping results in an electrical field reducing the concentration of minority charge carrier concentration and, thus, the recombination at the surface. The characteristic I - V -parameters of an interconnected PERT solar cell is given as an example in Tab. 4.4. The cell is laser welded with 35 J/cm^2 , which is the limiting fluence determined using the lifetimes samples, see Figure 4.9. The laser welding process fully preserves the efficiency of the solar cells. No degradation in V_{oc} , FF or J_{sc} can be detected.

4.2.3 Electrical properties

Similarly to the ns laser in section 4.1.2, we measure the contact resistance for the μs laser 2. We determine the contact resistance for the Al layer thickness d_{Si} on silicon of $2 \mu\text{m}$ and $10 \mu\text{m}$. Figure 4.11 shows the corrected resistance $R_{\text{cor}}(d)$ for the two cases. Due to the thick Al layer and, therefore, the lower resistance within the Al layer, the values for the corrected resistance $R_{\text{cor}}(d > 0)$ are lower for $d_{\text{Si}} = 10 \mu\text{m}$ compared to the $2 \mu\text{m}$. The average slope is $3.2 \text{ m}\Omega/\text{cm}$ for $d_{\text{Si}} = 10 \mu\text{m}$ and for $d_{\text{Si}} = 2 \mu\text{m}$ it is $15.7 \text{ m}\Omega/\text{cm}$. Assuming a width² of the strips of $970 \mu\text{m}$, this corresponds to a resistivity of the Al layer of $31.7 \text{ n}\Omega \text{ m}$ and $30.4 \text{ n}\Omega \text{ m}$ for d_{Si} of $10 \mu\text{m}$ and $2 \mu\text{m}$, respectively. These results are similar

²The laser diced edges of the strips are not perfectly straight leading to an uncertainty in the effective width.

to the ones determined by Nekarda et al. of $\rho = 29\text{--}33\text{ n}\Omega\text{ m}$ [138] for an in-line high-rate evaporation tool.

As discussed already for the ns laser, only an upper limit of R_c can be determined due to the uncertainty of the measurement. In the case of the $10\text{ }\mu\text{m}$ Al on silicon and a fluence of 44 J/cm^2 , R_c is below $1.5\text{ m}\Omega$. This corresponds to a contact resistivity of less than $7\text{ }\mu\Omega\text{ cm}^2$. Here, the resistance is related to the total intersection area of the metallized silicon strip and the Al strips on glass of $970 \times 440\text{ }\mu\text{m}^2$ and not only to the weld spots. In the case of $d_{\text{Si}} = 2\text{ }\mu\text{m}$ and $F = 36\text{ J/cm}^2$, R_c is below $1.7\text{ m}\Omega$, which results in a contact resistivity ρ_c of less than $8\text{ }\mu\Omega\text{ cm}^2$.

The contact resistivity for both thicknesses is close to the value of ρ_c determined for the ns laser ($< 5\text{ }\mu\Omega\text{ cm}^2$) and, thus, below the resistivity of standard contact soldering.

4.3 Laser welding on foil substrate by the μs laser

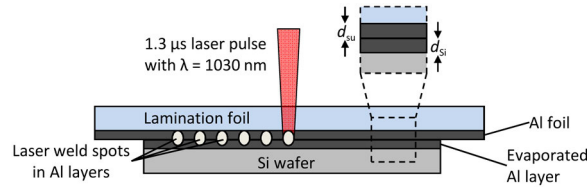


Figure 4.12: Schematic representation of the laser welding experiments in this section. The magnification indicates the thickness of the Al layer on the foil substrate and on the Si wafer d_{su} and d_{si} , respectively.

We also use lamination foil as an alternative to the glass substrate. The foil is a thermoplastic silicone (Tectosil, Wacker). We attach a $10\text{-}\mu\text{m}$ -thick Al foil to the lamination foil, see section 3.3.1 and Fig. 4.12. The silicone is not transparent for high intensities of UV-light. Therefore, we cannot apply the ns laser and use only the μs laser. Table 4.5 summarizes the parameters used in the experiments in this section.

4.3.1 Laser-induced damage

Figure 4.13 a) shows the normalized lifetime τ_{norm} in dependence on the applied laser fluence F for various thicknesses d_{Si} between $1\text{ }\mu\text{m}$ and $20\text{ }\mu\text{m}$ using the μs laser 2. We use a pitch between the weld spots $p_w = 250\text{ }\mu\text{m}$, which corresponds to a laser-welded area fraction f_w of about 2%. We observe no significant laser damage for layer thicknesses d_{Si} of $10\text{ }\mu\text{m}$ and $20\text{ }\mu\text{m}$. For $d_{\text{Si}} = 5\text{ }\mu\text{m}$, a reduced normalized lifetime τ_{norm} is detected for 73 J/cm^2 , i.e., the maximum fluence F_{max} is 69 J/cm^2 . In the case of $d_{\text{Si}} = 1\text{ }\mu\text{m}$ and $2\text{ }\mu\text{m}$, the maximum fluences are 62 J/cm^2 and 66 J/cm^2 , respectively. Therefore, the threshold fluences are higher for the glass substrate using the same laser.

We also vary the pitch between the laser weld spots, i.e., the laser welded area fraction f_w , as shown in Figure 4.13 b) for the case of $10\text{ }\mu\text{m}$ Al on the silicon. For $f_w = 9\%$ or a spot pitch of $250\text{ }\mu\text{m}$, no laser damage is detected, i.e., the maximum fluence F_{max} cannot be determined with the μs laser 2 due to the limited power. If the pitch is reduced to $100\text{ }\mu\text{m}$ ($f_w = 55\%$), we determine a maximum fluence of 62 J/cm^2 , which further reduces in the case $p_w = 71\text{ }\mu\text{m}$ ($f_w = 110\%$, i.e., slight overlapping of the laser pulses) to $F_{\text{max}} = 58\text{ J/cm}^2$. A possible

Table 4.5: Overview of the parameters that we vary or keep constant during the experiments in this section. The numeric values are given for constant parameters. In experiment 1 the limits of the laser welding process for various Al layer thicknesses on Si are determined, in experiment 2 we evaluate the impact of the pitch p_w , in experiment 3 we investigate the mechanical properties of the laser weld spots, and in experiment 4 we measure the electrical properties of the weld spots. Experiments 3 and 4 are done with the μs laser 1, with a smaller Gaussian radius than μs laser 2, see Tab. 3.1 and, thus, a higher fluence. No lifetime results are available, since the laser was replaced due to technical issues, but as shown in [139] a damage free laser welding is possible with these parameters ($F = 360 \text{ J/cm}^2$ and $f_w = 15\%$).

Experiment	Laser system	Substrate type	Al thickness on substrate	Al thickness on Si wafer	Number of pulses	Fluence	Welded area fraction
			$d_{\text{su}} [\mu\text{m}]$	$d_{\text{Si}} [\mu\text{m}]$		$F [\text{J/cm}^2]$	$f_w [\%]$
1	μs laser 2	foil	10	varied	1	varied	8
2	μs laser 2	foil	10	10	1	varied	varied
3	μs laser 1	foil	10	10	1	400	3
3	μs laser 1	foil	10	10	1	300	1.5

explanation for this dependence on the pitch is the residual heat from the neighboring weld spots. The lamination foil does not serve well as a heat sink due to its low heat capacity and thermal conductivity. Additionally, changes in the optical properties of the lamination foil, which is effected by previous laser pulses close by, can increase the local absorption.

4.3.2 Mechanical properties

Testing the mechanical properties of the foil stack is not possible in the same manner as described for the glass substrate, since the mechanical contact between the Al foil and the substrate is less strong then the contact of evaporated Al to the glass. Figure 4.14 a) shows

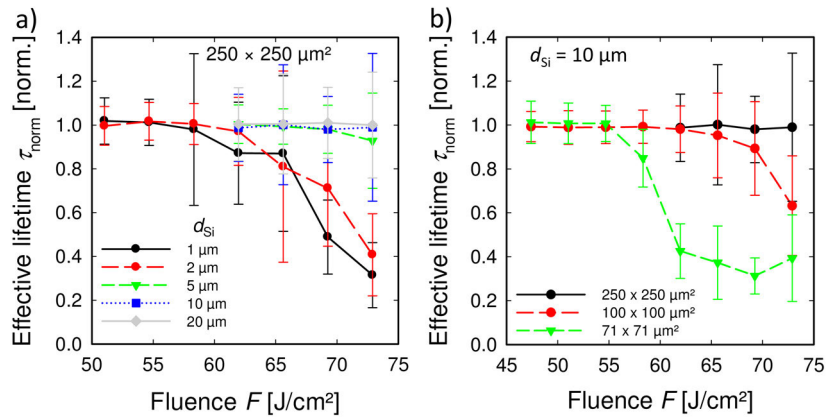


Figure 4.13: a) The normalized effective charge carrier lifetimes τ_{norm} in dependence on the laser fluence for various thicknesses of the Al layer on the silicon d_{Si} between $1 \mu\text{m}$ and $20 \mu\text{m}$ in the case of the μs laser 2. b) Variation of pitch p_w between the weld spots for d_{Si} of $10 \mu\text{m}$. Table 4.5, experiment 2 summarizes the experimental details.

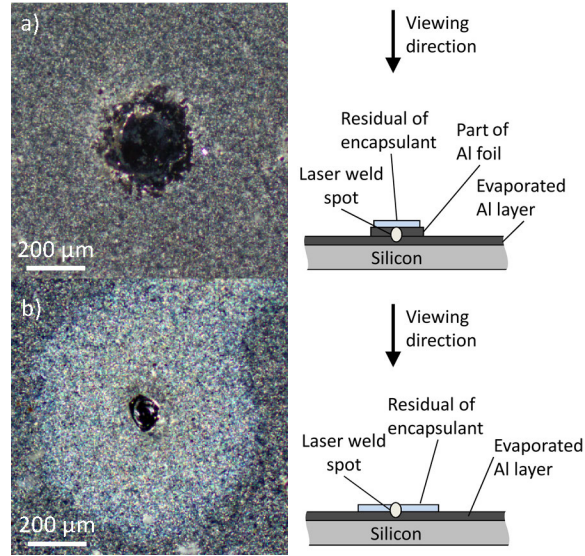


Figure 4.14: Microscope image of the Al metallized surface of the Si sample after tear-off of the encapsulant with the Al foil (not shown here). a) A microweld of the sample which is not laminated is covered by a residual piece of Al foil, whereas in b) a microweld of the sample laminated at 160°C is surrounded by the encapsulant (bright area). The schematics are cross-sections of the samples seen in the microscope images. Table 4.5, experiment 3 summarizes the experimental details.

a microscope image of a laser weld between an Al foil and the Al metallization on a wafer. A piece of Al foil is visible, which is pulled out of the Al layer on the substrate, as depicted in the schematics next to the microscope image. The perpendicular tear-off stress required to pull out the Al foil for such an interconnection formed by μs laser 1 is $\sigma = 77 \pm 13 \text{ kPa}$. We also laminate the stack (Al metallized Si wafer, Al foil, and lamination foil) at 160°C after the laser welding, as done in the module process. In this case, the interconnection with the μs laser 1 leads to a perpendicular tear-off stress σ of $380 \pm 80 \text{ kPa}$. Figure 4.14 b) shows that remains of the encapsulant are visible on the Si sample around the weld spot. Therefore, we have to assume that the encapsulant can flow through pin holes around the laser weld into the gap between the two Al layers during lamination. Thereby, it supports the mechanical contact. Additionally, the Al foil has a stronger contact to the lamination foil.

However, in both cases the mechanical contact cannot be related to the weld spots itself. If the sample is not laminated, the peel-off force is limited due to the breakage of the Al foil. If the sample is laminated after laser welding, the mechanical properties are influenced by the encapsulant, which supports the mechanical contact between the Al layer on the Si wafer and the Al foil.

4.3.3 Electrical properties

We also determine the contact resistance R_c in the case of the lamination foil substrate using μs laser 1. Figure 4.15 shows the corrected resistance R_{cor} in dependence on the distance d . We determine a contact resistance of less than $2.2 \text{ m}\Omega$. Taking into account the cross-section area of $940 \times 420 \mu\text{m}^2$, this corresponds to a contact resistivity ρ_c of below

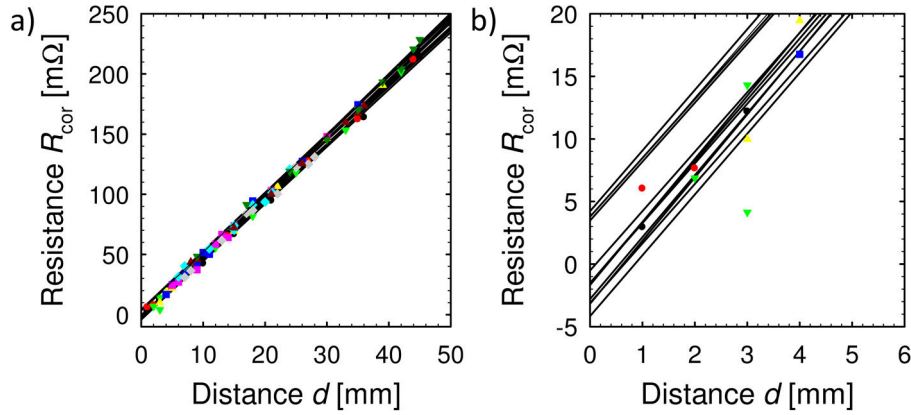


Figure 4.15: a) Corrected measured resistance $R_{\text{cor}}(d)$ versus the distance d separating the Al foil strips on the lamination foil substrate in the case of the μs laser 1 for $d_{\text{Si}} = 10 \mu\text{s}$. The laser welded area f_w is about 20%. The different symbols correspond to the different sets of measurements and the solid lines are the corresponding linear regressions. b) is a magnification of the measurements shown in a). Table 4.5, experiment 4 summarizes the experimental details.

$9 \mu\Omega\text{cm}^2$. This contact resistivity is close to the value of ρ_c determined for both lasers on glass ($< 8 \mu\Omega\text{cm}^2$) and below the resistivity of standard contact soldering, too.

4.4 Chapter summary and discussion

4.4.1 Comparison of the laser systems

In section 4.1 and 4.2 the results of laser welding on a glass substrate for the ns and the μs laser 2 are described. For these laser systems and their corresponding wavelengths, the optical penetration depth in aluminum is about 10 nm [87]. The energy is therefore transferred into the material by thermal conduction [87]. For laser joining of thin metal foils [101] or in the case of ablation of thin metal layers [140], it is assumed that the thermal diffusion length l_T limits the processes. Here, the difference in pulse duration τ_p between the two laser systems is two orders of magnitude and the resulting thermal diffusion lengths are $2.9 \mu\text{m}$ and $22 \mu\text{m}$ for the ns and μs laser, respectively. The threshold fluence required for welding, i.e., the minimum fluence, with single pulses is $28 \pm 2 \text{ J/cm}^2$ in the case of the ns laser. For the μs laser, this threshold is $35 \pm 2 \text{ J/cm}^2$. In contrast to the thermal diffusion length, the difference in the threshold for the laser welding is marginal. Additionally, the thickness of the Al layer on the glass $d_{\text{su}} = 10 \mu\text{m}$ is much thicker than the thermal diffusion length of the ns laser pulses. For shorter pulses, one would expect a higher threshold fluence to reach the same temperature in a depth larger than the thermal diffusion length. We conclude that the thermal diffusion length does not limit the Al layer thickness as in the other mentioned applications. This can be explained by the fact that the irradiated energy cannot escape in an open half space, as in the case of laser ablation, due to the covering glass substrate. Hence, the largest part of the energy is conducted into the Al layer and used for the welding process.

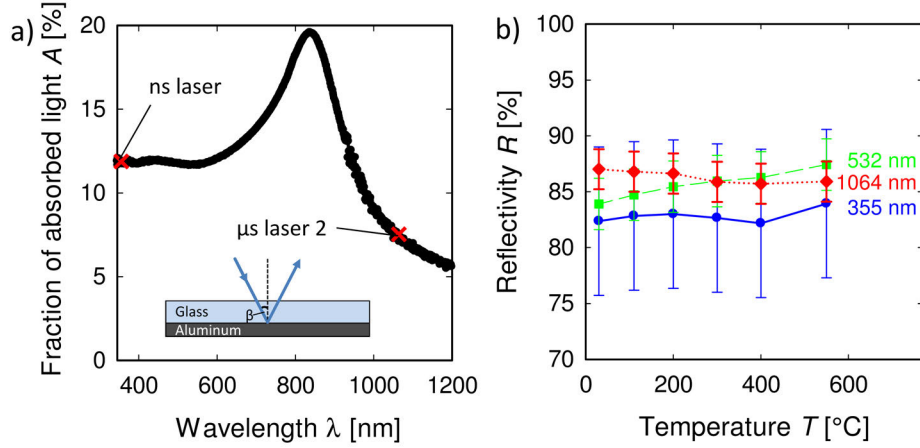


Figure 4.16: a) The fraction of light absorbed in the Al layer A for the used samples. The total reflectivity is measured through the glass under an incident angle of $\beta = 8^\circ$ at room temperature. The inset shows a schematics of the measurement configuration. b) Reflectivity R of an Al layer measured through a glass substrate under an incident angle of $\beta = 40^\circ$ between room temperature and 550°C . The lines are guides to the eye.

Wavelength and temperature dependent absorption

An explanation for the difference in the minimum fluence ($F = 28\text{ J/cm}^2$ and 35 J/cm^2) can be given by the difference in the reflectivity of the Al layer for the two laser wavelengths. Figure 4.16 a) shows the absorbed fraction of light. Here, the reflectivity R of an Al-coated glass is measured under an incident angle of 8° at room temperature using a spectrophotometer (Agilent Cary 5000), see inset in Fig. 4.16 a). The transmission of the glass is constant for these wavelengths (less than $\pm 0.4\%$ relative). Assuming no absorption in the glass and no transmission through the Al layer, the fraction of light absorbed in the Al layer underneath the glass substrate is

$$A = 1 - R. \quad (4.1)$$

R includes the reflectivity at the front side of the glass of 4% and the reflectivity of the Al layer.

The absorption is $11.9 \pm 0.4\%$ for the ns laser emitting at 355 nm and for the μs laser emitting at 1064 nm it is $7.5 \pm 0.4\%$. The higher absorption in the Al layer at 355 nm explains the tendency of the reduced threshold for the ns laser. However, the measurement is performed at room temperature and we expect from literature that the reflection varies with temperature [141, 142]. During welding, the Al surface is heated from room temperature above melting and, thus, effects the total amount of energy absorbed in the Al layer.

Using a spectral ellipsometer (Woollam M2000U) we measure the reflectivity R of the samples under an incident angle of 40° between room temperature and 550°C , as shown in Figure 4.16 b). Within the uncertainty, no variation in dependence on temperature is observed for the depicted wavelength. We again neglect the absorption in the glass, which shows according to its data sheet [113] no significant changes in transmission in dependence on temperature. Hüttner et al. [142] predict that above the melting temperature the absorption is similar for both wavelengths and ranges from 10 to 15% increasing with further temperature rise. As a consequence, the relative difference of the absorbed energy

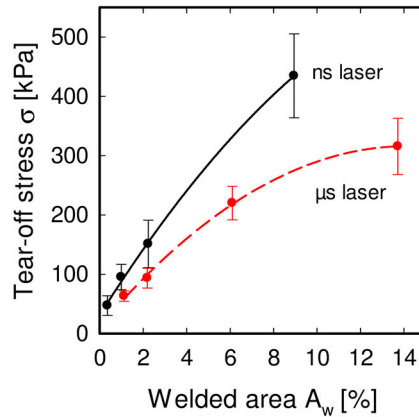


Figure 4.17: Perpendicular tear-off stress σ in dependence on the laser welded area f_w for the ns laser and μ s laser 2. The lines are guides to the eye.

between the two wavelength is reduced taking into account the whole welding process. The difference in welding threshold is in accordance with the difference in reflectivity.

Mechanical properties of the two laser systems

A comparison of the tear-off stress σ in dependence on laser welded area f_w is given in Figure 4.17. The laser fluence is kept constant for the ns laser at 40 J/cm^2 and for the μ s laser at 44 J/cm^2 . The Al layer thickness is $d_{\text{Si}} = 10 \mu\text{m}$. Comparing the perpendicular tear-off stress σ in the case of the same laser-welded area f_w for both laser processes shows that laser weld spots formed by the ns laser lead to stronger mechanical contacts compared to the ones formed by the μ s laser 2. However, a constant laser-welded area f_w corresponds to a higher number of laser spots per area in the case of the ns laser due to its smaller beam diameter compared to the μ s laser 2. This indicates that not the whole laser-welded area is involved in the mechanical contact, which becomes also clear taking a closer look on Figure 3.2. There one can observe that mainly the outer parts of the weld spots contribute to the mechanical contact. Therefore, at a constant laser-welded area the ns laser leads to higher tear-off stresses due to the larger sum in circumference of the weld spot.

As one would expect, a larger laser-welded area leads to a stronger mechanical contact. However, doubling the laser welded area leads not to twice the tear-off stress σ . This nonlinearity can be explained by boundary effects, for example a slightly disturbed and a non-perfect perpendicular tear-off. In such a case, the tear-off may start from one side and a peel-off might additionally contribute to the separation process, resulting in lower tear-off stresses. Further, for large area fractions of laser welded area and using the ns laser, we observed damages in the glass substrates that may also lead to a decrease of the tear-off stress.

4.4.2 Comparison of the glass and foil substrates

The comparison of the results related to the two different substrates, glass in section 4.2 and lamination foil in section 4.3, shows that in the case of the lamination foil the maximum

fluence F_{\max} is increased. One explanation is that the glass is only marginally affected by the focused laser light, whereas the lamination foil shows locally thermal decomposition. This results for example in increased absorption within the lamination foil. However, these damages of the lamination foil do not negatively affect the long term stability of the samples after final lamination as shown in accelerated aging tests (see section 6.1.3).

4.4.3 Electrical properties of the laser welds

For applications in photovoltaics, a low contact resistivity is of high importance. A benchmark for the laser welding process is the standard contact soldering process leading to a contact resistivity ρ_c of about 0.05 to 0.1 m Ω cm² [55]. Laser soldering results in lower contact resistivities of about 0.01 m Ω cm² [55]. For the laser welding process presented here, the contact resistivity is below 0.01 m Ω cm² for the two used lasers and both substrates and, thus, below the benchmark. No strong dependence on the substrate or laser system is observed within the measurement accuracy.

4.4.4 Summary

We evaluate the process windows for the ns laser and μ s laser in this chapter. We use 10 μ m Al on the glass substrate to contact Al layers deposited to Si wafers with various thickness. It is possible to contact down to single micrometers without inducing detectable laser damage with ns laser. For the μ s laser, we detect no damage when contacting Al layers with thickness down to $d_{\text{Si}} = 2 \mu\text{m}$.

In order to decrease the process time, it is favorable to use single laser pulses for welding. Since the μ s laser leads to much higher tear-off forces with single pulses, using the μ s laser for Al layer thickness above 1 μ m is preferred.

Together with the lamination foil as substrate, we can only use the μ s laser, since the encapsulant is not transparent for the UV light of the ns laser. With an Al foil of an thickness of 10 μ m on the encapsulant, laser welding is possible without inducing damage. However, the mechanical properties highly depend on the mechanical contact between the Al foil and the encapsulant and, thus, a determination of the process limits depends on the sample preparation. For an Al layer thickness of 1 μ m, laser fluences of up to 62 J/cm² can be applied.

5 Thermal processes involved in the AMELI laser welding process

In the previous section 4.4, we discussed the results of the laser welding process for two pulse durations and various laser pulse energies. However, in contrast to other laser welding processes [87, 101] our AMELI process is not solely limited by the thermal diffusion length. We investigate in this chapter the heat transfer in the Al layers in order to answer the open question regarding the relevant processes. We numerically simulate the thermal distribution using finite element modeling (FEM) to understand the mechanisms of the laser welding process. Here, we focus on the laser welding process using the μs laser, since it is more relevant for application in the following chapter¹.

To form a reliable weld spot it is required that the Al layer on the substrate and the cell metallization have to melt and fuse. We first focus on the melt process within the layer on the substrate in experiments and simulations, since only this Al layer is irradiated by the laser. Additionally, we investigate the heat losses by thermal radiation on the front side and by heat conduction into the glass substrate.

5.1 Experimental determination of melt-through threshold

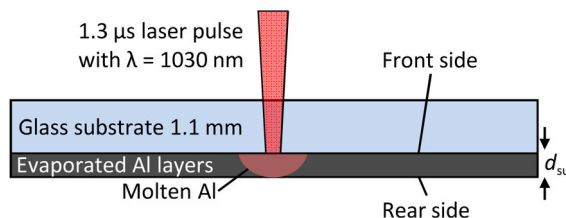


Figure 5.1: Schematic representation of the laser welding experiments in this section. The front side of the Al layer, which is in contact with the glass substrate, is irradiated by the laser. The melt-through is detected on the opposite side, here the bottom of the Al layer. The thickness of the Al layer on the glass substrate is d_{su} .

We start with the experimental investigation of the processes occurring during laser irradiation and the determination of the melt-through threshold. This threshold is the laser energy required such that the melt front penetrates through the whole Al layer, which enables welding. A cross section of samples used in the experiment is shown in Fig. 5.1. The melt-through is detected in dependence on the Al layer thickness on a glass substrate d_{su}

¹We presented a comparison of the ns and μs laser using an one dimensional analytical approximation [88] in [143]. However, the 1D analytical approximation is not able to include temperatures depended material parameters, pulse shape and horizontal heat flow and, therefore, results in only limited description of the process.

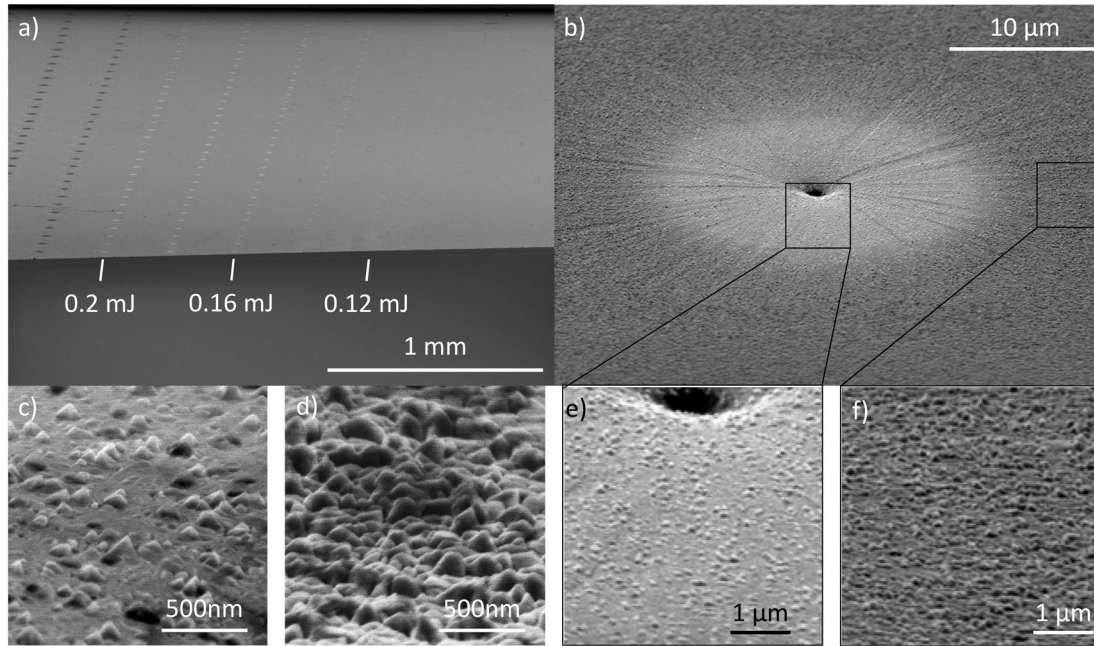


Figure 5.2: SEM images of an Al layer with $1\ \mu\text{m}$ thickness irradiated through the glass substrate with various laser pulse energies. a) An overview of the Al surface that is opposite to the irradiated side. Several lines corresponding to the different laser energies are visible. b) shows a laser irradiated spot for $E_p = 0.2\ \text{mJ}$. c) and e) show magnifications of the bright regions and d) and f) of the dark regions. e) and f) are magnifications of the image in b).

by investigating the surface opposite to the irradiated side (rear side) using SEM. We vary d_{su} between $1\ \mu\text{m}$ and $20\ \mu\text{m}$, starting with the thinnest.

Figure 5.2 shows an example of an Al layer with $d_{\text{su}} = 1\ \mu\text{m}$. An overview of the Al surface after laser treatment is shown in Fig. 5.2 a). Lines of laser irradiated spots are visible in the image. The pulse energy decreases from left to right. In order to determine the melt-through threshold, we are interested in the surface modification on the rear side that indicates the layer was molten. A bright appearance of the laser spots is visible down to $0.12\ \text{mJ}$. Figure 5.2 b) shows an example of such a bright area in the case of an applied pulse energy of $E_p = 0.2\ \text{mJ}$. The brighter appearance of the laser spot in the tilted SEM image is caused by the reduction of the surface texture towards its center, see also Fig. 5.2 c) and e). The Al layer surrounding the laser spot appears dark due to its rough surface structure, as shown in Fig. 5.2 d) and f). We attribute the change of the surface to the melting process initiated by the laser. Therefore, we take the increase in the SEM signal as an indicator to determine the melt-through threshold.

For the thicker layers, we observe no change of the surface texture. However, a bulging of the surface or even ejected and re-solidified aluminum is visible in Fig. 5.3. We attribute these observations to the thermal expansion of the liquefied aluminum within the solid layer. This results in an increase of pressure and stress within the aluminum layer. If the stress surpasses the ultimate strength of the Al layer, a breakage of the surface and, subsequently, an ejection of liquid Al occurs. The glass substrate is indispensable to build up the pressure, since without substrate the molten Al would expand into the open half space on top of the Al layer. The threshold is defined as the minimum pulse energy that results in an ejection of molten Al for the thicker Al layers.

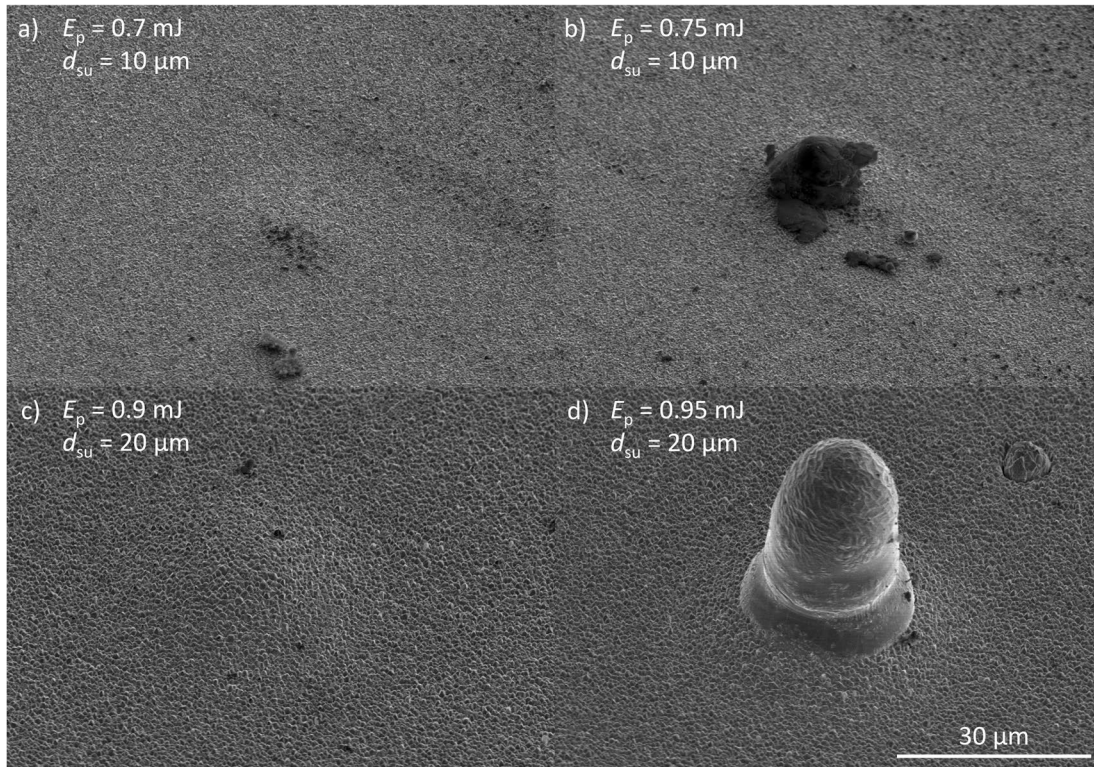


Figure 5.3: SEM images of an Al layer with 10 μm and 20 μm thickness irradiated through the glass substrate with laser pulse energies above and below the threshold for which modifications are observed. a) and b) show images of a sample with an Al layer thickness d_{su} of 10 μm , c) and d) with $d_{\text{su}} = 20 \mu\text{m}$. In a) and c) we observe no modification of the surface structure, i.e., the energy E_p is below the threshold, and in b) and d) the energy is above the threshold.

Figure 5.4 shows the determined pulse energies required for the melt-through in dependence on the Al layer thickness d_{su} . Higher pulse energies are required to reach the melt-through for thicker Al layers. We observe two different regimes of increase. For thin layer ($d_{\text{su}} = 1\text{--}5 \mu\text{m}$), doubling the layer thickness requires approximately twice the pulse energy. Assuming a heat capacity of 0.95 J/gK [95] a density of 2700 kg/m³ [87] the increase in energy of 0.106 mJ/ μm layer thickness results in a molten cylindrical volume with a radius of 31 μm . This is in accordance with the Gaussian radius for small pulse energies of $\omega_0 = 32 \pm 12 \mu\text{m}$, see section 3.2.

We observe a different increase for thicker layers, i.e., $d_{\text{su}} = 7 \mu\text{m}$ to 20 μm . For these thicknesses, we observe thrown-out material instead of a change of the surface appearance due to melting. Therefore, the two distinct processes leading to the presence of molten Al on the rear side result in different dependence of the threshold on d_{su} .

Based on the interpretations of the SEM images, which we use to determine the melt-through threshold, we postulate two qualitative working hypotheses for the different processes:

- For thin layers, the heat induced at the front side causes the irradiated layer to melt. When the energy is sufficiently large, the melt front reaches the rear side by thermal diffusion.
- For thicker layers, the aluminum also melts at the front side due to the laser irradi-

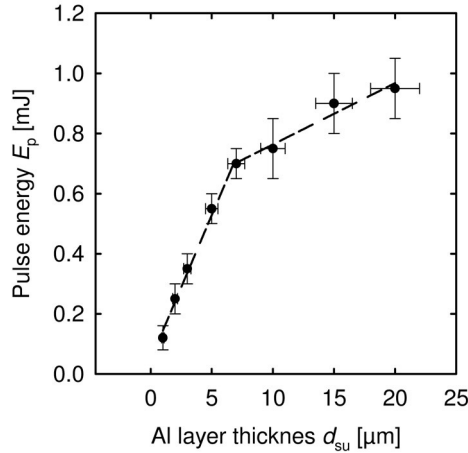


Figure 5.4: Experimentally determined pulse energies required to melt through the Al layers with thicknesses d_{su} between 1 μm and 20 μm , which are shown as black dots. The dashed lines are linear fits for the thickness ranges between 1 μm and 5 μm as well as 7 μm to 20 μm .

ation. The melt front propagates into the direction of the rear side. Due to thermal expansion and the phase transition, the material expands. When enough Al is molten and the solid part between the melt front and the rear side is still too stiff, the surface of the Al layer breaks and molten material is pressed through the crack.

5.2 Two dimensional finite element method

We use numerical simulations based on finite element method (FEM) in COMSOL 4.3 [145] in order to verify our hypotheses. Figure 5.5 shows an example of the simulated temperature distribution. We employ the rotational symmetry of the laser weld spots to compute the three-dimensional heat flow in two dimensions. A Gaussian profile of the laser pulse in space (shown in Fig. 5.5 b) as white plot) and time (shown in Fig. 5.6 a) as dashed line) is used. We simulate the heat flow into the glass or the second Al layer to evaluate the change in internal energy after the laser irradiation. Since we assume surface absorption of the Al layer (the optical penetration depth is about 10 nm \ll d_{su} [87]), the energy is induced into the system at the boundary between the glass and the Al layer. We use temperature-dependent material parameters for the heat capacity of the glass substrate and of the Al layer and include the melting enthalpy and the thermal conductivity for both layers, and the optical absorption of the Al layer. For the absorption, we use the measured values as shown in Fig. 4.16 a) for temperatures up to melting. For temperatures above the melting point, the values are taken from literature [142]. Since the measured values scatter for various samples, we simulate emissivities of 7% to 8%. The detailed material parameters are given in appendix A.5.

We experimentally determine the Gaussian radius ω_0 using the method of Liu [112], see section 3.2. The measured data show that our beam shape deviates from a perfect Gaussian shape. Therefore, we vary in the simulations the Gaussian radius ω from 32 μm to 42 μm as determined in section 3.2. In this section we describe the laser intensities by the two independent parameters, the pulse energy and the Gaussian radius.

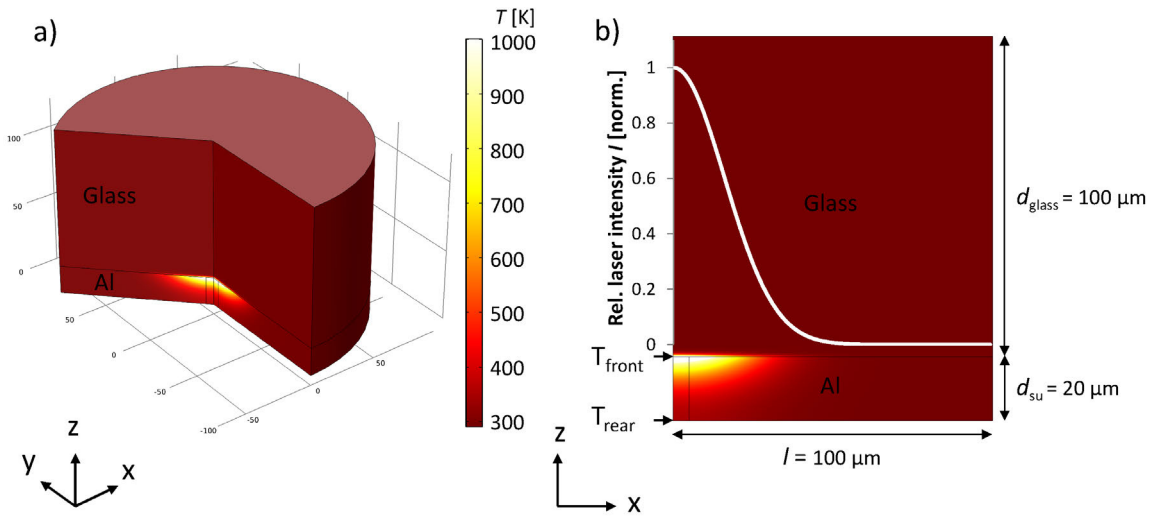


Figure 5.5: Simulation results of a 20- μm -thick Al layer on glass irradiated with 0.85 mJ, a Gaussian radius of 32 μm , and absorbed energy fraction $A = 8\%$ at 1.3 μs after the onset of the laser pulse. The simulations are performed in 2D employing the rotational symmetry. We simulate only 100 μm glass instead of 1100 μm in order to decrease simulation time. However, due to the low thermal conductivity of the glass, this does not effect the temperatures in the Al layer. The diameter of the simulated domain is 200 μm . a) shows a 3D representation of the thermal profile and b) a 2D surface plot in the x-z-plane. It also shows the points (end of arrows) where we detect the temperatures T_{front} and T_{rear} at the front and the rear side of the Al layer, respectively. The overlaid white plot is the spacial distribution of the normalized laser intensity $I(x)$, which is implemented in the simulations as a surface heat source at the boundary between the glass and the Al layer (horizontal line at the position of the arrow of T_{front} .)

We determine in the simulation the threshold pulse energy that is required for melting the layer through, i.e., the melt front has propagated through the total thickness of the Al layer. For this, we evaluate the temperature T_{rear} of the Al layer in the center of the laser spot at the rear site, see Fig. 5.5.

Figure 5.6 a) shows exemplarily the temporal behavior of the laser pulse and the temperature T_{rear} of a 3- μm -thick Al layer. The laser pulse starts at 0 μs , reaches its intensity maximum at 1.3 μs , and decreases again, see dashed line. The temperature at the bottom of the sample T_{rear} also rises, when the pulse power increase. However, T_{rear} further increases after the laser pulse power has reached it maximum. The temperature is related to the energy by the heat capacity $C(T)$ and the energy increases further after the pulse intensity has reached its maximum. Additionally, the temperature is delayed by thermal diffusion through the Al layer. In these simulations we vary the pulse energy between 0.3 mJ and 0.4 mJ. For sufficiently high pulse energies, the temperature reaches a plateau at $T_{\text{m}} = 933.5 \text{ K}$. This plateau is caused by the melting enthalpy H_{m} . Up to the melting point the temperature increases with increasing energy. At $T_{\text{m}} = 933.5 \text{ K}$ the phase transition starts and requires a certain amount of energy per mass H_{m} . Therefore, a further increase in energy at $T = T_{\text{m}}$ does not result in a further rise in temperature until H_{m} is provided, i.e., the phase transition takes place. If we further increase the energy in the system to overcome the melting enthalpy, the phase transition occurs and the temperature rises again. We assume melting, when the temperature rises above T_{m} . Figure 5.6 a) orange graph ($E_{\text{p}} = 0.34 \text{ mJ}$) shows an example of the required pules energy to overcome the melting point. Additionally, Fig. 5.6 a) shows that the molten aluminum, which is required for welding, is present only for times shorter

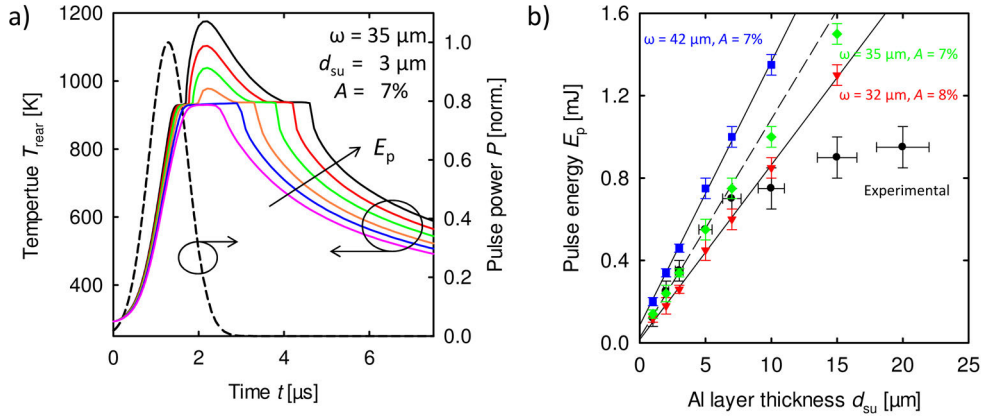


Figure 5.6: a) Example of the temperature in the center of the laser spot (solid lines) in dependence on time for an Al layer thickness $d_{\text{su}} = 3 \mu\text{m}$, a Gaussian radius $\omega = 35 \mu\text{m}$, and an absorbed energy fraction below melting of $A = 7\%$. We vary E_p from 0.3 mJ to 0.4 mJ in steps of 0.02 mJ. The dashed line shows the temporal profile of the laser pulse intensity. b) Experimentally determined threshold pulse energies in black (as given in Fig 5.4) and the simulated thresholds for a Gaussian radius $\omega = 32 \mu\text{m}$ and $42 \mu\text{m}$ and an absorbed energy fraction below melting of $A = 7\%$ and 8% .

than $10 \mu\text{s}$ after the onset of the laser pulse. The simulations are done for discrete values, which results in the uncertainty given in Fig. 5.6 b).

5.2.1 Simulation results for melt-through by thermal diffusion

Figure 5.6 b) shows the experimental data, which we have discussed in section 5.1, and the threshold energies determined by the FEM simulations. We simulate the two extreme cases based on the experimentally determined parameters, i.e., the lower limit of the absorbed laser intensity with $\omega = 42 \mu\text{m}$ and $A = 7\%$ (blue squares) and the upper limit with $\omega = 32 \mu\text{m}$ and $A = 8\%$ (red triangles). The simulated pulse energies required to melt the Al layer in dependence on the layer thickness are well approximated by a linear regression. Therefore, the results behave qualitatively equally as the experimental values for Al layer thickness up to $5 \mu\text{m}$. The slope of the linear regression of the experimental values is $0.106 \text{ mJ per } \mu\text{m}$ Al layer thickness, see section 5.1. For the simulated results, the slope is between $0.0847 \text{ mJ}/\mu\text{m}$ and $0.1279 \text{ mJ}/\mu\text{m}$ for the upper and lower limit, respectively. Thus, the experimentally determined dependence of the melting threshold on d_{su} is in the center of one determined for the upper and the lower limit (average of the two limits $0.1063 \text{ mJ}/\mu\text{m}$). The same holds within the uncertainty also for the absolute values, e.g., in the experiment we determined a threshold of $0.35 \pm 0.05 \text{ mJ}$ for $d_{\text{su}} = 3 \mu\text{m}$ and in the simulation of $0.26 \pm 0.02 \text{ mJ}$ and $0.46 \pm 0.02 \text{ mJ}$ for the upper and lower limit of input parameters, respectively. Please note, that all input parameters base on literature or experimental values. Varying the input parameter, e.g., the Gaussian radius, within the limits of the input parameters allows us also to fit the experimental values. Figure 5.6 b) shows the simulation results for $\omega = 35 \mu\text{m}$ and $A = 7\%$ (green diamonds). These values describe the experimental results well up to $d_{\text{su}} = 5 \mu\text{m}$. Since the only heat transport involved in the simulations is thermal diffusion, we conclude that experimental results for $d_{\text{su}} \leq 5 \mu\text{m}$ can be described by thermal diffusion. This confirms our hypothesis for thin layers. However, above $5 \mu\text{m}$ the

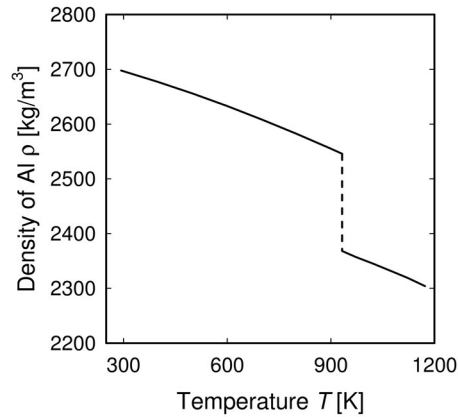


Figure 5.7: Temperature-dependent density of aluminum based on literature values [144].

experimental results show a different dependence on d_{su} than for thinner layers and, thus, the simulated results deviate from the experimental values. Therefore, we assume that for thicker layers the process is no more governed by thermal diffusion only.

5.2.2 Simulation results for onset of melting at the irradiated interface

For $d_{\text{su}} > 5 \mu\text{m}$, we observe in the SEM images (Fig. 5.3) a bulging and penetration of the Al layer's rear surface by molten aluminum, which can be caused by thermal expansion of the heated Al layer. Figure 5.7 shows the temperature dependence of the density of aluminum. It decreases for solid aluminum from room temperature (2.70 g/cm^3) to its melting point at 933.5 K (2.55 g/cm^3) by about 5.7% [144]. After the phase transition the density of liquid aluminum at 933.5 K is 2.37 g/cm^3 , which is 12.2% lower than the density of solid Al at 293 K [144]. Therefore, the phase transition results in a significant expansion of its volume. In order to correlate the phase transition with the required pulse energy, we probe T_{front} in the simulation to investigate the onset of the melting at the irradiated Al surface, i.e., the interface between the glass and the aluminum. We use again an absorbed fraction of light $A = 7\%$ and 8% and vary the Gaussian radius ω . Figure 5.8 shows the required pulse energy for the different Gaussian radii used in the simulations and the experimental values.

The simulation results for the required pulse energy to start melting at the front side ($T_{\text{front}} > T_{\text{m}}$) show qualitatively a similar dependence as the experimental results. Again the experimental values are within the results for the upper and lower limit of the simulations. However, they approach the lower limit of the input parameters ($\omega = 42 \mu\text{m}$ and $A = 7\%$; blue squares).

The green diamonds in Fig. 5.8 shows the results for the parameters $\omega = 35 \mu\text{m}$ and $A = 7\%$, which best described the experimental findings for $d_{\text{su}} \leq 5 \mu\text{m}$ in section 5.2.1. Using these parameters, the simulations approach the experimental data well without overestimating them. An overestimation by the simulation results would correspond to a pulse energy that leads to a material ejection in the experiment, but melting has not yet started in the simulations. Therefore, the underestimation of the experimental results by these simulations is reasonable and can be caused by two reasons. We observed in section 3.2 that ω is larger

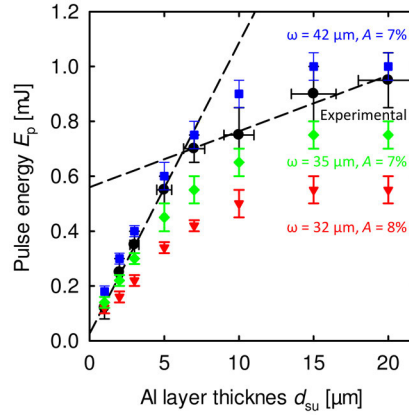


Figure 5.8: Experimentally determined threshold pulse energies are shown in black with the corresponding linear fits (as given in Figure 5.4). The colored data points show the simulated thresholds for the onset of melting on the irradiated Al surface for a Gaussian radius $\omega = 32 \mu\text{m}$ and $42 \mu\text{m}$ and an absorbed energy fraction below melting of $A = 7\%$ and 8% .

for high pulse energies than for small pulse energies ($E_p < 0.8 \text{ mJ}$). The other reason might be that an onset of melting is not sufficient to break the surface and a limited amount of material needs to melt in order to eject molten material.

The comparison of the values for the onset of the melting on the irradiated side, see Fig. 5.8, with the values of the melt-through, see Fig. 5.6 b), shows that for increasing layer thickness the difference between both thresholds becomes larger. This is caused by the faster penetration of the thermal energy through a thinner layer. For thin Al layers, both thresholds match the experimental data as well. In other words, the onset of melting and the melt-through of the thin layers require similar pulse energies. Thus, when melting starts on the front side of the Al layer its rear side is also close to melting and its ductility is drastically increased [146] such that a breakage is less probable. In the case of the thicker layers, e.g., $d_{\text{su}} = 10 \mu\text{m}$, the experimental values approach the onset of the melting as shown in Fig. 5.8. These simulations describe the experimental behavior qualitatively well in contrast to the simulation of the melt-through, see Fig. 5.6 b).

We conclude for layer thicknesses $d_{\text{su}} > 7 \mu\text{m}$ that pulse energies close to the threshold for onset of melting are required for the ejection of material. In other words the melt front has to penetrate only a small fraction of the layer thickness in order to break the surface. In contrast to this, for thinner layers the threshold for a visible surface modification is in accordance with the required energy for melting the Al layer through.

5.3 Estimation of energy losses

In the experiments in section 5.1 we observed that the glass substrate is required to direct the molten aluminum towards the rear side of the Al layer, where we aim to fuse the Al layer on the substrate and the solar cell metallization to form the weld spot. However, the substrate is also a heat sink and, thus, part of the energy induced by the laser cannot be used for welding, i.e., it is lost for the process. In the following, we want to analyze this and other processes consuming energy, which then is not available for the welding.

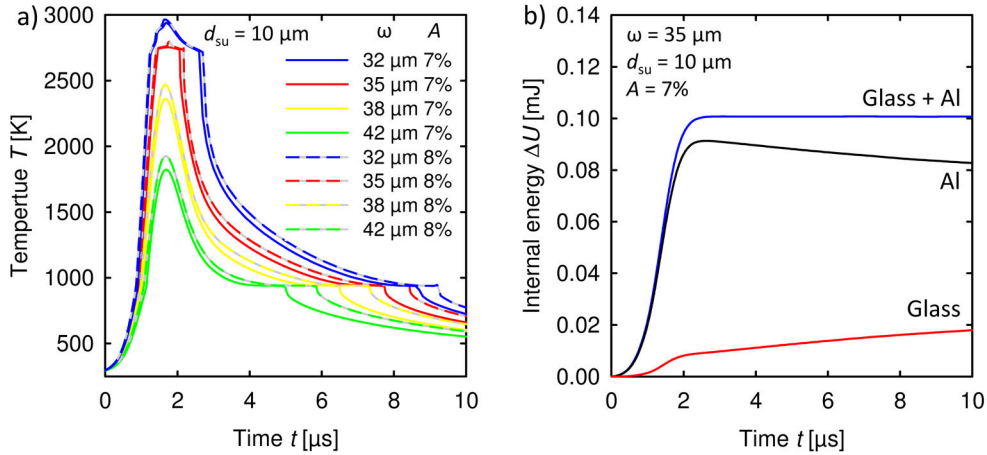


Figure 5.9: a) Temperature in dependence on time for Gaussian radii ω between $32\ \mu\text{m}$ and $42\ \mu\text{m}$ and an absorbed energy fraction below melting of $A = 7\%$ and 8% in the case of a $10\text{-}\mu\text{m}$ -thick Al layer and the limiting laser pulse energy² of $E_p = 1.3\text{ mJ}$. b) Change in internal energy ΔU within the Al layer, the glass substrate, and the sum of both in dependence on time for $E_p = 1.3\text{ mJ}$, $A = 7\%$, and $\omega = 35\ \mu\text{m}$.

The transport of thermal energy can occur by thermal conduction, radiation, convection, and also by evaporation or ejection of material. Thermal energy, which is transported out of the Al layers we want to weld, is lost for the process. The ejection of material occurs in this case only in the direction of the second Al layer, since it is hindered by the glass substrate into the other direction. Additionally, the conduction into glass substrate decreases the maximum temperature and, thus, less material is evaporated. The transfer of molten aluminum into the direction of the second layer is part of the welding process and not regarded as a loss of energy. Processes related to thermal convection are prevented by the glass substrate on the upper side of the irradiated Al layer. On the lower side, the Al layer is in contact with the second Al layer and the gap between them is evacuated. Therefore, we assume no convection for laser welding processes. It becomes only relevant for long term processes, which cool the glass substrate in times of seconds after the welding. However, this is several orders of magnitude longer than $10\ \mu\text{s}$, which is the time frame the welding process takes place.

Figure 5.9 a) shows the temporal profile T_{front} , i.e., the hottest location, for a $10\text{-}\mu\text{m}$ -thick Al layer. We irradiate the surface with the maximum pulse energy² of 1.3 mJ as determined in the section 4.2. We assume again an absorbed energy fraction $A = 7\%$ and 8% for surface temperatures below the melting point. For these laser intensities, the temperature increases up to the evaporation temperature. However, the enthalpy of evaporation is relatively large, i.e., it is 17 times higher than heating aluminum from room temperature to the melting point [144]. For the simulation parameters describing the experimental results well for $d_{\text{su}} \geq 7\ \mu\text{m}$ in Fig. 5.8 ($\omega = 35\ \mu\text{m}$ and $A = 7\%$ (green diamonds) and $\omega = 42\ \mu\text{m}$ and $A = 7\%$ (blue squares)), no evaporation is reached in the simulation, see Fig. 5.9 a). Only for increased absorption $A = 8\%$ for $\omega = 35\ \mu\text{m}$ a starting of evaporation is detected as well as for $\omega = 32\ \mu\text{m}$. However, we assume for larger pulse energies ($E_p \geq 0.8\text{ mJ}$) that

²We determined a maximum fluence $F = 47\text{ J/cm}^2$ for laser welding of a $10\text{-}\mu\text{m}$ -thick Al layer on the substrate as well as on the silicon. We use a Gaussian radius $\omega = 42\ \mu\text{m}$ to calculate the fluence. The corresponding pulse energy is 1.3 mJ .

the larger beam diameter (e.g. $\omega = 42 \mu\text{m}$) describes the beam profile best, see section 3.2. The evaporation temperature might even be larger than the assumed 2730 K in the case pressure is build up within the molten layer (e.g., $T_v = 3180 \text{ K}$ at a pressure of 5 bar) [95]. During welding the Al layer on the glass is additionally cooled by the solar cell (here not included in the simulations). Therefore, we expect that no evaporation occurs and the welding process is driven by thermal expansion in the liquid phase.

Using the temperature profile of Fig. 5.9 a) for $\omega = 35 \mu\text{m}$ and $A = 7\%$ we compute the thermal emission of the hottest location as an upper limit of the radiative losses. We use the Stefan-Boltzmann law

$$j = \sigma T^4, \quad (5.1)$$

where j is the emitted irradiance in W/m^2 and $\sigma = 5.67 \times 10^{-8} \text{ W}/(\text{m}^2\text{K}^4)$ the Stefan-Boltzmann constant. The laser welding process is finished in the first $10 \mu\text{s}$. Due to the short time of the event only $0.17 \text{ mJ}/\text{cm}^2$ are emitted in the center of the spot. For the used input parameters, we calculate using equation 3.2 a maximum irradiated fluence in the center of the spot of $F_0 = 68 \text{ J}/\text{cm}^2$. We do not include the emissivity for the thermal irradiation or the absorption of the laser light. For the laser radiation, the absorption varies with temperature between 7% and 15%, i.e., a factor of two. Nevertheless, the thermal emission is five orders of magnitude lower than the irradiated laser fluence and, thus, can be neglected³.

Thermal conductivity to the neighboring layers, i.e., the second Al layer and the glass substrate, is another path of heat transfer. The second Al layer needs to be heated up for welding, thus we concentrate on the heat transfer to the glass substrate. We simulate again the glass with the Al layer and ignore losses out of this system. Figure 5.9 b) shows the increase in internal energy for the Al layer (black line) and the glass substrate (red line) as well as for the total system (blue line). The total amount of energy absorbed by the system is 0.1 mJ , which is only 9% of the irradiated pulse energy, assuming a system efficiency of 88% for the beam line⁴.

After $10 \mu\text{s}$, when the Al layer at the interface to the glass substrate is cooled well below its melting point, 18% of the energy induced by the laser into the system is within the glass. However, the glass substrate hinders losses by convection, absorption of the laser light in Al plasma or vapor, and by ejection of molten and evaporated Al. Irradiating an Al metallized Si surface with 1.3 mJ creates a crater in the Al surface with a depth of $3 \pm 1 \mu\text{m}$ and a diameter of $48 \mu\text{m}$ as experimentally determined. Assuming a spherical cap, the evaporation of this volume leads to an energy loss of $0.10 \pm 0.03 \text{ mJ}$. Even if the absorbed energy fraction A is twice as large as in the case of the Al evaporated on a glass substrate, this is in the order of 50% of the absorbed energy. Therefore, the losses by evaporation are larger than the losses by conduction into the glass.

³Alternatively, instead of the energy irradiated per area, the comparison can be done by the power per area. The maximum laser intensity is $56 \text{ MW}/\text{cm}^2$. Compared to this, the intensity of the thermal emitted irradiance for liquid Al close to boiling (2730 K) of $315 \text{ W}/\text{cm}^2$ is marginal, assuming again an emissivity of 1 for both.

⁴The beam line efficiency is defined here as the laser power measured in the working plane divided by the laser power measured after the laser head.

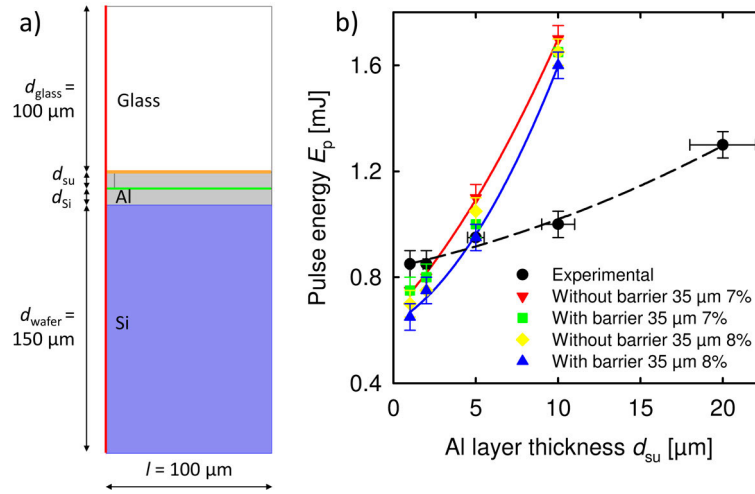


Figure 5.10: a) Cross-section of the simulation geometry. The red vertical line indicates the symmetry axis of the system, the orange horizontal line the location of the surface heat source (compare Fig. 5.5) and the green vertical line the thermal barrier. b) Experimentally determined minimum laser pulse energy for welding in black and as determined by simulation, with and without a thermal barrier in color, respectively. The dashed and contentious lines are guides to the eye for the experimental and simulation results, respectively. In the case of the simulation and $d_{\text{su}} = 20 \mu\text{m}$ the required pulse energy exceeds the maximum of the used laser system of 2 mJ.

5.4 Interface properties between the two Al layers

So far, we focused on the first Al layer in order to understand the processes that initiate the welding, i.e., the melt-through of the Al layer irradiated by the laser. For the laser interconnection, it is required that both layers, the Al layer on the glass substrate and the metallization on the Si wafer or solar cell, melt and fuse. Figure 5.10 b) shows the experimental dependence (black dots) of the minimal pulse energy required to form an interconnection that sustains a peel-off force of 1 N applied to a $1.5 \times 1.5 \text{ cm}^2$ silicon sample metallized with $10 \mu\text{m}$ Al. For thicker Al layers on glass, higher pulse energies are required. We extend the FEM simulations by the second Al layer and a silicon wafer with a thickness of $d_{\text{wafer}} = 150 \mu\text{m}$, see Fig. 5.10 a). For a first approximation, we assume perfect thermal contact between all the layers, i.e., no thermal barrier; the two layers behave as they are one solid. We define the required pulse energy for the case that both Al layers are molten at their interface. Figure 5.10 b) shows the required pulse energies to reach $T_{\text{rear}} > T_{\text{m}}$ in the simulation. The simulation results with no thermal barrier (red triangle and yellow diamonds) do not describe the experimental values. For thin layer ($d_{\text{su}} < 5 \mu\text{m}$), the simulations underestimates the experimentally determined required pulse energy for welding, whereas for thicker layers ($d_{\text{su}} \geq 5 \mu\text{m}$) it is overestimated.

As visible in Fig. 5.11 a) there is a gap in the order of single μm instead of a perfect contact between the two Al layers. Therefore, we introduce a thermal barrier in order to model the change of the interface properties due to the expansion of the first Al layer, which is pressed to the second Al layer by this expansion. Once both layers are molten and fused, the thermal contact between them is assumed to be perfect. Details of the thermal barrier are given in appendix A.6. The thickness of the thermal barrier in the simulations is 1 nm.

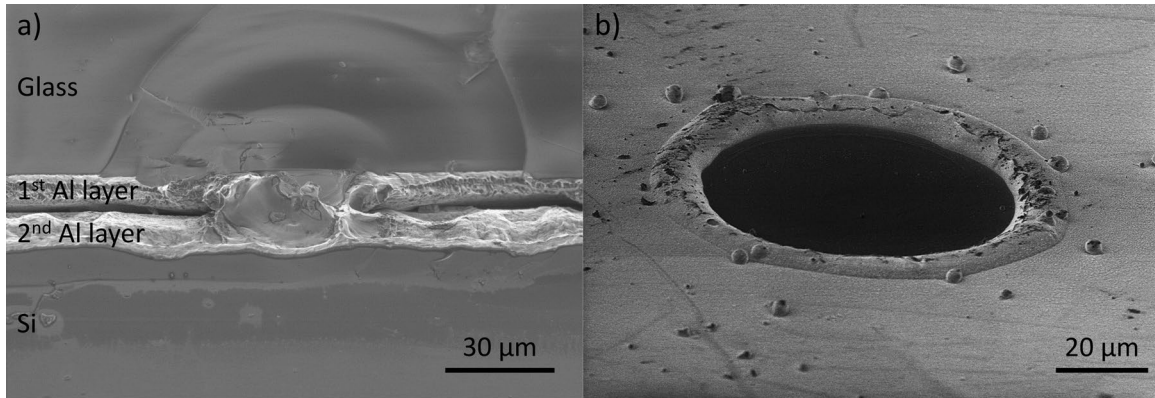


Figure 5.11: a) SEM image of a laser weld spot between an Al layer on glass and one on Si with $d_{\text{Si}} = d_{\text{su}} = 10 \mu\text{m}$ and $E_p = 1.2 \text{mJ}$. There is a gap of several μm visible between the two Al layers. b) Laser weld spot on an Al layer on glass with $d_{\text{su}} = 1 \mu\text{m}$ and $E_p = 0.85 \text{mJ}$.

The barrier has no thermal conductivity up to 400 K below the melting point⁵ and then approaches linearly the thermal conductivity of bulk Al. At the melting temperature, when we assume that molten Al is in contact with the Al layer on the silicon wafer, it is equal to the thermal conductivity of aluminum. Once the melting temperature has been reached the thermal conductivity stays equal to that of bulk Al also for lower temperatures, since we assume that the molten and resolidified aluminum of the layer on the substrate is still in contact with the Al layer on the silicon.

As shown in Fig. 5.10 b) (green squares and blue triangles) the introduction of the thermal barrier (indicated as green line in Fig. 5.10 a)) decreases the required pulse energy, since the diffusion of heat into the Si wafer is delayed and higher temperatures are reached within the Al layers. However, this does not change significantly the dependence of the simulated required pulse energy on d_{su} . The simulations still overestimate the required pulse energies for thicker layers ($d_{\text{su}} > 5 \mu\text{m}$).

The explanation for the overestimation for thicker Al layer, e.g., $d_{\text{su}} = 10 \mu\text{m}$, see Fig. 5.11 b), can be given based on the observation for the first Al layer as described above. The process is not only governed by the thermal diffusion. However, the melting of aluminum at the interface between the Al layer and the glass results in a breakage of the Al layer and ejection of the molten aluminum in the center of the laser spot.

For thin layers (e.g., $d_{\text{su}} = 1 \mu\text{m}$ and $2 \mu\text{m}$), the simulations underestimate the required pulse energy. Thus, a melt-through of the layer is not sufficient. Figure 5.11 a) shows that there is a gap in the order of micrometers between the two Al layer. The thermal expansion of the thin Al layers is not sufficient to close this gap. SEM images of the laser parameters that lead to welding (Fig. 5.11 b)) show that aluminum from the center of the weld spots is gathered in a rim. According to theory, the formation of such rim is driven by repulsion in the center of the weld spot and the surface tension within the molten layer [147]. To enable the repulse, the pulse energy needs to be sufficiently large to evaporate the Al layer in the

⁵Changing the value of onset of the thermal conductivity of the barrier to higher temperatures, does not lead to significant lower pulse energies required for the onset of melting of both Al layers. However, it leads to spatial oscillation of the barrier's properties. Locally the temperature is reached such that the barrier layer becomes thermally conductive. This cools the neighboring areas, thus, the barrier layer isolates. An example of the resulting temperature distribution is given in appendix A.6.

center of the spot. This is for example in the case of $d_{\text{su}} = 2 \mu\text{m}$, $\omega = 35 \mu\text{m}$, $A = 7\%$, and a pulse energy of $E_p = 0.7 \text{ mJ}$ according to the simulation. This is less than the pulse energy required for welding of $E_p = 0.85 \text{ mJ}$, see Fig. 5.10 b). The accumulation of aluminum in a rim is able to close the gap between the two Al layers in order to form a weld spot.

The experimental observations in the SEM images and the numerical simulations show that the gap between the two Al layers has a critical impact on the laser welding process. The gap affects the thermal transport between the two Al layers, which cannot be described by thermal diffusion only. Additionally, the gap separating the two Al layers needs to be filled by accumulation of molten Al to form a weld spot. The accumulation can be achieved due to surface tension of molten Al or by ejection of material through the broken surface as observed for thick layer ($d_{\text{su}} > 5 \mu\text{m}$).

5.5 Chapter summary and discussion

In this chapter, we investigated the thermal processes involved in the AMELI laser welding process using the μs laser. We observed in experiments using SEM two different processes for the penetration of the melt front through the Al layer on the glass substrate. For thin layers ($d_{\text{su}} \leq 5 \mu\text{m}$), we assume that the heat induced at the front side causes the irradiated layer to melt. When the energy is sufficiently large, the melt front reaches the rear side by thermal diffusion. The results of the FEM simulations using only thermal diffusion for the heat transport are in agreement with the experimental results and confirm the assumption. For thicker layer ($d_{\text{su}} > 5 \mu\text{m}$), we also assume that the Al layer melts at the front side due to the laser irradiation. The melt front propagates into the direction of the rear side. Due to the thermal expansion and the phase transition, the material expands. When enough Al is molten and the solid part between the melt front and the rear side is still too stiff, the surface of the Al layer breaks and molten material is pressed through the crack. The onset of melting also increases the absorption of the Al layer, i.e., the absorbed energy fraction A , from 7% to 10% [142]. Hence, after melting starts on the front side, significantly more energy is absorbed than below melting, resulting in a faster increase in temperature and, thus, further expansion of the material. The simulations of the start of the melt process at the front side described the experimental data well and support our hypothesis. We can conclude that the process for the penetration of the melt front through the Al layer is dominated by melting. Therefore, the AMELI process is a combination of the LIFT process and conduction welding.

Additional to the process within the Al layer on the substrate, two other relevant factors are identified. In order to achieve the ejection of the molten aluminum for $d_{\text{su}} > 5 \mu\text{m}$ the substrate is indispensable to hinder the molten or evaporated material to expand into the direction opposite to the welding partner. In the case of the absence of the substrate, a recoil pressure caused by evaporation is required [101]. The evaporation of Al extracts energy from the irradiated layer and the vapor above the surface leads to a parasitic absorption. Therefore, the use of a substrate is highly beneficial for the welding, but it absorbs, e.g., in the case of $d_{\text{su}} = 10 \mu\text{m}$, up to 18% of the total absorbed energy. This is the second largest loss we identified, but it is still less compared to the energy losses by evaporation in case no substrate is present. The largest loss is caused by the high reflectivity of the mirror-like interface between the aluminum and the glass. The application of a CrNi layer can reduce

the reflectivity of 92.5% for our Al layer down to 60% for the solid state and 40% for the liquid state [95].

The second relevant factor is the gap between the two Al layers we aim to weld. It needs to be filled by accumulation of molten Al to form a weld spot. The melt-through process is not able to close the gap for thin Al layers on the substrate. An accumulation can be achieved due to surface tension of molten Al or for thick layer by ejection of material through the broken surface. The gap is related to the surface roughness of the Al layers and should be minimized to achieve a reliable welding process.

The FEM simulations employed in this chapter focus on conduction of the thermal energy. In order to include other physical effects the model may be extended. For thin layers, dynamic effects of the molten material, e.g., convection within the melt pool and the surface tension, are of interest for the simulation of the welding processes. In contrast for the thicker layers, solid mechanical aspects like stress and strain within the glass and Al layer due to the thermal expansion may be taken into account, since they might break the surface of the Al layer. The main challenge for both simulation approaches is the drastic change of various material properties during the phase transition. For example in the case of the simulations of the strain, these are the absorption, thermal conductivity, heat capacity, elasticity, critical strain, thermal expansion coefficient, etc..

6 Module interconnection of BJBC solar cells by laser welding

In the following chapter the application of the AMELI process and the properties of the resulting modules are presented. We start with the standard geometry of 5" interdigitated back-contacted solar cells that have two busbars on the rear side. Using these cells, we investigate the influences of the laser welding on BJBC solar cells. This is followed by an evolutionary and combined development of both, the cell's contact geometry and the module interconnection scheme, here called the cell-to-module-interface, to increase the module performance. This is mainly achieved by omitting the busbars and changing the metallization geometry to decrease the resistive losses. We analyze the losses of the interconnection schemes and the longterm stability of laser-welded modules.

6.1 Two busbar modules

Most BJBC solar cells feature an interdigitated finger structure on the rear side. The fingers of each polarity are united in one busbar at an edge of the solar cell's rear side. This results in a shape of the metallization similar to a comb, see Fig. 6.1. The busbars for the two polarities are located at opposite edges and are perpendicular to the fingers. The busbars feature extended structures, which serve as solder pads in case of conventional solder-based

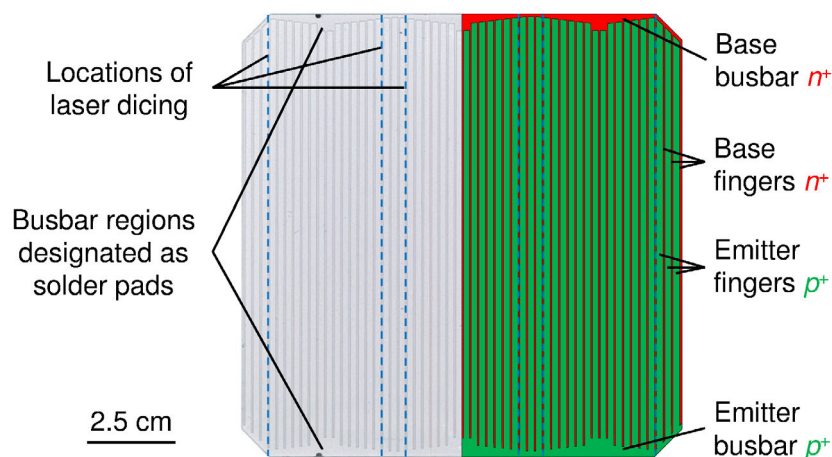


Figure 6.1: Photograph and schematic of BJBC solar cell. The Al metallization scheme coincides with the doping scheme of the solar cell. The base and emitter regions are shown in red and green, respectively. The cell features two busbars, one for each polarity, on opposite edges. The busbars have three wide pads, which are used for contacting during I - V -characterization and are designated as solder pads. The blue dashed lines indicate the locations, where we laser dice the cells in strips.

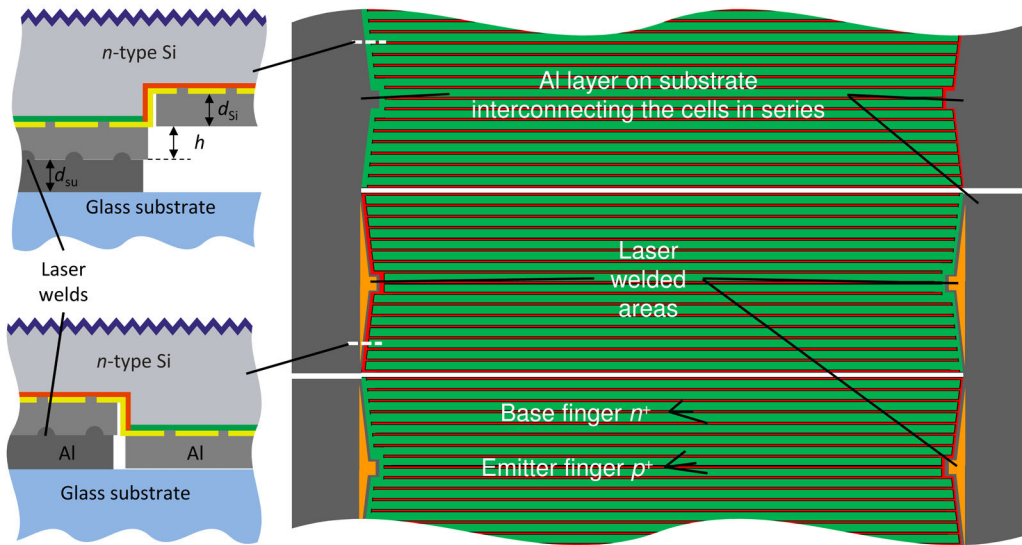


Figure 6.2: Three cell strips interconnected by an Al layer (gray) carried on a substrate (not shown here, see for example Fig. 6.3 b)) are shown. The Al layer enables a series interconnection by laser welding. On the upper cell the entire Al structure on the substrate is shown and on the other two cells the laser-welded areas are indicated in orange. In a module all cells are interconnected by laser welding. On the left-hand side cross-sections of the laser-welded areas for contacting the emitter (top) and base regions (bottom) are shown. The location of the cross-section is indicated with white dashed lines. h denotes the height difference between n^+ -regions and the p^+ -regions. The thicknesses of the Al layer on the substrate and the solar cells are d_{su} and d_{si} , respectively. The cross-sections are not in scale.

interconnection. We evaluate the laser welding process for both types of substrates, glass and lamination foil. We limit the experiments for the proof-of-concept to mini modules consisting of three to five cell strips instead of full-area solar cells. All fingers are still in contact with the busbars, when we laser dice the BJBC solar cells parallel to the fingers. Therefore, we characterize the solar cells in an I - V -tester after laser dicing (before interconnection) as well as in the fabricated module (after interconnection). This enables us to detect the changes induced by the laser welding process.

Figure 6.2 presents a sketch of the interconnection of BJBC solar cell strips with two busbars. It shows the interconnecting structure (gray Al layer) and the Al metallization of the base and emitter regions of the solar cell strips in red and green, respectively. The solar cells are interconnected in series. We form the contact between the solar cell metallization and the Al layer on the substrate by laser welding. The laser-welded areas are indicated in orange.

6.1.1 Glass substrate

Figure 6.3 a) shows a photograph of a proof-of-concept module fabricated by laser welding. The solar cells are n -type BJBC solar cells fabricated on $125 \times 125 \text{ mm}^2$ wafers. We laser dice them parallel to the fingers into cell strips, which are $27.5 \times 125 \text{ mm}^2$ in size. Dicing is done with the ns laser in the base region from the rear side of the solar cells, see blue dashed lines Fig. 6.1. In this way, all fingers are still in contact with the busbar. The thickness of the cell metallization is $d_{si} = 25 \text{ }\mu\text{m}$. These cells feature a height difference between base and

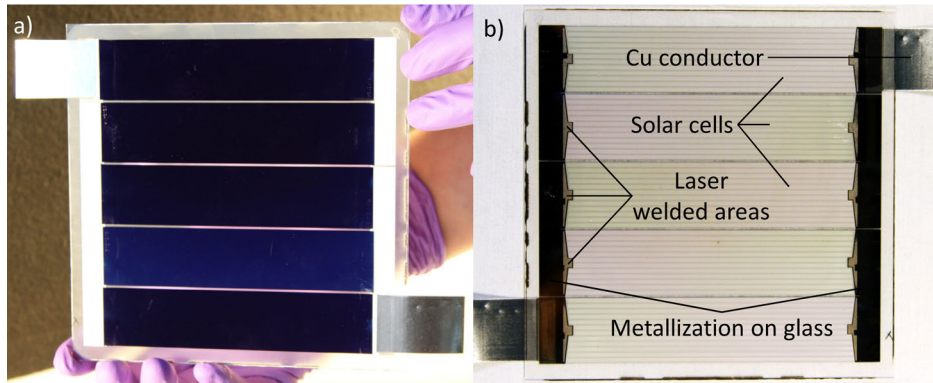


Figure 6.3: a) Front side and b) rear side of a proof-of-concept module consisting of five n -type BJBC solar cells interconnected on a glass substrate using laser welding. The metallization on the glass substrate is structured such that the cells are connected in series after the welding process. For external connection, the Al-clad copper conductors are laser welded to the Al layer on the glass.

emitter region of $h = 20 \mu\text{m}$, see Fig. 6.2. The substrate is a borosilicate glass metallized with aluminum. We choose an Al layer thickness of $d_{\text{su}} = 20 \mu\text{m}$ to compensate the height difference on the cells and to avoid a gap between the cell metallization and the Al layer on the substrate during laser welding. The Al layer is structured using μs laser 1 such that the Al coating remains only on the areas that are in contact with the busbars of the solar cells or necessary to enable a series interconnection. The described structure is visible in Fig. 6.2 and Fig. 6.3 b). The busbars are laser welded to the Al layer on the substrate using the ns laser. For external connection, we laser weld Al-clad copper conductors to the Al metallization on the substrate.

Table 6.1 gives the I - V -parameters of a module interconnected with this process. The module I - V -measurement is done using a module flasher (cetisPV by h.a.l.m. Elektronik GmbH). Assuming a damage-free interconnection in first order approximation, one would expect the open-circuit voltage V_{oc} of the module to be the same as the sum of V_{oc} of

Table 6.1: I - V -parameters measured under standard testing conditions ($100 \text{ mW}/\text{cm}^2$, 25°C) of n -type BJBC solar cells interconnected on a glass substrate using laser welding. The measurement uncertainty of the LOANA measurement tool is given for the individual cells. The uncertainty of the module flasher is only known for the power at the maximum power point (MPP). Abbreviations used: Cell area A , efficiency η , fill factor FF, open-circuit voltage V_{oc} and short-circuit current I_{sc} .

Cell/ Module	A [cm^2]	η [%]	FF [%]	V_{oc} [mV]	I_{sc} [mA]
Cell 1	34.4	19.7 ± 0.6	77.2 ± 0.8	664 ± 3	1323 ± 38
Cell 2	34.4	19.7 ± 0.6	76.4 ± 0.8	666 ± 3	1334 ± 38
Cell 3	34.4	20.3 ± 0.6	77.7 ± 0.8	667 ± 3	1347 ± 38
Cell 4	34.4	20.2 ± 0.6	77.0 ± 0.8	669 ± 3	1348 ± 38
Cell 5	34.4	20.3 ± 0.6	76.8 ± 0.8	667 ± 3	1362 ± 39
Module	172.0	20.0 ± 0.8	77.2	3328	1339
Module laminated	172.0	19.3 ± 0.8	76.8	3330	1294

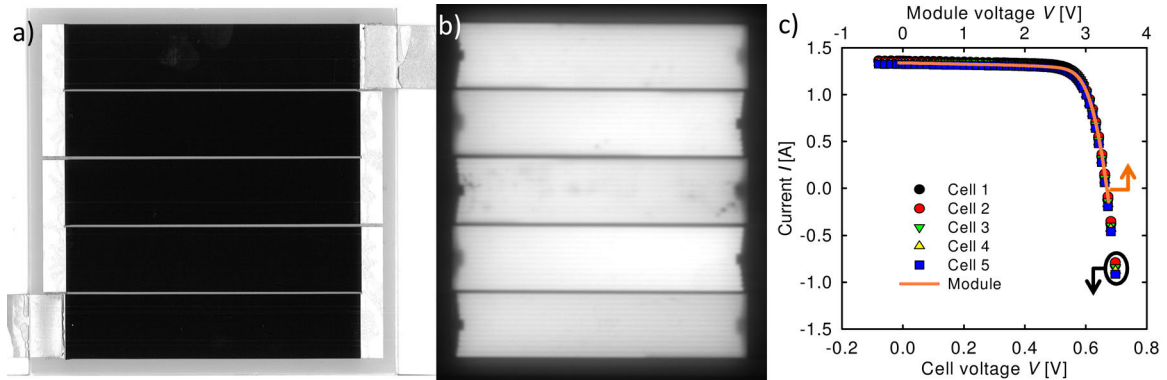


Figure 6.4: a) Photograph of the front side of a proof-of-concept module consisting of five n -type BJBC solar cells interconnected on a foil substrate using laser welding. b) An electroluminescence image of the same module at an applied voltage of $V = 3150$ mV and c) the I - V -characteristics of the individual cells before laser welding and of the module after laser welding tested under standard testing conditions.

the individual cells interconnected in series. Here, the sum of the individual cells voltages is $\Sigma V_{oc} = 3333 \pm 15$ mV. Within the uncertainty of the measurement, the open-circuit voltage of the module with $V_{oc} = 3328$ mV is unchanged after interconnection. Damage induced during laser welding would result in a degradation of the passivation layer between the Al metallization and the silicon wafer or even in crystal damage in the wafer. Both would cause higher recombination rates, which reduce the open circuit voltage. Since no significant degradation of V_{oc} is detected, this indicates a damage-free interconnection. It is also confirmed by the fill factor of the module of 77.2%, which shows no detectable degradation due to the laser welding, e.g., by series resistances or shunts. Additionally, the short-circuit current is in accordance with the expectation that in the case of a loss-free series interconnection the lowest current of the individual cells limits the current of the module. The short-circuit current of the module of 1339 mA is within the uncertainty of the measurement as high as the lowest short-circuit current of the cells, here $I_{sc} = 1323 \pm 38$ mA. The module has an efficiencies of 20% before lamination. This shows that the welding process is suitable to contact BJBC.

After lamination with a transparent front sheet and a lamination foil, absorption in these films and reflection at the front side reduce the short-circuit current to 1294 mA and thus the efficiency to 19.3%.

6.1.2 Foil substrate

We also apply the laser welding process for module interconnection using a lamination foil as substrate. Figure 6.4 a) shows a photograph of the module after lamination. An Al foil in the size of 156×156 mm² is applied to the lamination foil and structured using the μ s laser 1 such that it has the same geometry as shown in Fig. 6.2 and Fig. 6.3 b) in the case of the glass substrate.

The two initial large-area (125×125 mm²) solar cells have an efficiency of 20.4% and 20.5% before laser dicing. Table 6.2 gives the I - V -parameters of the cells after laser dicing. We dice in the same way as described above for the solar cells interconnected on the glass substrate,

Table 6.2: I - V -parameters measured under standard testing conditions (100 mW/cm^2 , $25 \text{ }^\circ\text{C}$) of n -type BJBC solar cells interconnected on a foil substrate using laser welding. The measurement uncertainty of the LOANA measurement tool is given for the individual cells. The uncertainty of the module flasher is only known for the power at the maximum power point (MPP). In the case of the laminated module a shadow mask is used with an open area corresponding to the area of the cells. Abbreviations used: Cell area A , efficiency η , fill factor FF, open-circuit voltage V_{oc} and short-circuit current I_{sc} .

Cell/ Module	A [cm ²]	η [%]	FF [%]	V_{oc} [mV]	I_{sc} [mA]
Cell 1	34.4	20.4±0.6	78.3±0.8	663±3	1350±38
Cell 2	34.4	20.8±0.6	78.5±0.8	666±3	1368±39
Cell 3	34.4	20.7±0.6	78.1±0.8	666±3	1372±39
Cell 4	34.4	20.2±0.6	77.5±0.8	664±3	1349±38
Cell 5	34.4	20.7±0.6	77.8±0.8	666±3	1377±39
Module	172.0	20.4±0.9	78.2	3326	1348
Module laminated	172.0	19.3±0.8	78.3	3320	1275

see section 6.1.1. Additionally, the I - V -parameters of the module after interconnection are given. The module is measured by the module flasher and without encapsulant and glass on the front side. Therefore, no effects due to multiple reflection as in the case of finished modules are expected. Figure 6.4 c) shows the measured I - V -characteristics of the individual cells and the module. The solar cells voltage is given on the lower x -axis and the module voltage on the upper x -axis, which has a five times larger scale. The I - V -characteristic of the module coincides well with the characteristics of the individual cells, indicating the absence of any degradation. This is confirmed by comparing the sum of the open-circuit voltages of the individual cells ($\Sigma V_{\text{oc}} = 3325 \pm 15 \text{ mV}$) with the open-circuit voltage of the module ($V_{\text{oc}} = 3326 \text{ mV}$). The short-circuit current and the fill factor do not indicate any losses, too. We observe no degradation when comparing the efficiencies of the cells before dicing and the efficiency of the module.

After lamination with a front glass and a white backsheet, the efficiency η decreases by 1.1% absolute to 19.3%. Here, we perform the measurement with a shadow mask to avoid an additional illumination of the solar cells by multiple reflections at the white backsheet on the rear side of the module. The reflectivity of about 4% at the air-glass interface results in a reduction of the short-circuit current and, thus, in a reduction of the efficiency of 0.8% absolute. The reflection at the glass front side explains the major fraction efficiency loss. The remaining 0.3% are caused by absorption in the glass and the lamination foil and by misalignment of the shadow mask to the position of the cells¹.

To identify damages or cracks induced during processing, we take an electroluminescence image of the final module after lamination. The image in Fig. 6.4 b) is taken at an applied voltage of $V = 3150 \text{ mV}$. The EL image shows a homogeneous appearance and no dark lines are observed. This demonstrates that no cracks are induced during positioning, laser welding, handling, and lamination.

¹The shadow mask is structured according to the distances used for laser structuring of the Al layer on the substrate. However, the cells are slightly misaligned (up to a 0.5 mm) with respect to the substrate in the final module due to positioning accuracy of the cells and their movement during the lamination process.

Table 6.3: I - V -parameters measured under standard testing conditions (100 mW/cm^2 , 25°C) of three full-sized $90\text{-}\mu\text{m}$ -thick n -type BJBC solar cells interconnected on a foil substrate using laser welding. The measurement uncertainty of the LOANA measurement tool is given for the individual cells. The uncertainty of the module flasher is only known for the power at the maximum power point (MPP). The values of the expected module are calculated from the I - V -characteristic of the cells 1-3. Abbreviations used: Cell area A , efficiency η , fill factor FF, open-circuit voltage V_{oc} and short-circuit current I_{sc} .

Cell/ Module	A [cm^2]	η [%]	FF [%]	V_{oc} [mV]	I_{sc} [mA]
Cell 1	156.25	20.0 ± 0.6	76.9 ± 0.8	682 ± 3	5953 ± 170
Cell 2	156.25	19.8 ± 0.6	76.6 ± 0.8	683 ± 3	5910 ± 168
Cell 3	156.25	19.7 ± 0.6	76.0 ± 0.8	684 ± 3	5918 ± 169
Module expected	468.75	19.8 ± 0.6	76.5 ± 0.8	2049 ± 9	5923 ± 169
Module laminated	468.75	19.2 ± 0.8	77.4	2046	5694

Large-area solar cells

The solar cells interconnected above have an area of 34.4 cm^2 . However, most BJBC solar cells are fabricated on full-sized $125 \times 125 \text{ mm}^2$ wafers in industry [148]. Using larger cells, larger currents are generated leading to increased fill factor losses. In the case of our small solar cells, we observe no detectable losses in fill factor. We interconnect three solar cells $125 \times 125 \text{ mm}^2$ in size on a foil substrate to investigate if the FF is also unaffected for full-sized solar cells. Here, solar cells with a thickness of $90 \mu\text{m}$ are contacted, which is challenging for a solder based process [21, 149].

Table 6.3 shows the measured cell and module I - V -parameters of the three interconnected solar cells. In order not to damage the fragile string, the module is only characterized after lamination. It is remarkable that in contrast to the other modules presented so far the fill factor is higher than the fill factors of the individual solar cells. For a better comparison of the cell and module results, we determine the theoretically resulting fill factor after interconnection of the solar cells (module expected in Tab. 6.3, no resistance due to interconnection are included). Therefore, we interpolate the I - V -characteristic and sum up the voltages for each current point². The calculated I - V -characteristic bases on the characteristics of the three individual cells and has a fill factor of $76.5\pm 0.8\%$. The finished module has a fill factor of 77.4% , which is beyond the expectations of a loss-free interconnection³.

The gain in fill factor results from the interconnection by the Al foil, which transports the current on the whole width between the cells. Therefore, the current transport within the busbars in the direction perpendicular to the fingers is omitted. Figure 6.1 shows the shape of the busbar with areas intended to be used as solder pads. These are also in contact with the contact needles during the I - V -measurements of the cells. Thus, the current of

²The cell tester records the I - V -characteristic by measuring the current for a defined voltage. However, for series interconnected solar cells the voltages at defined currents need to be added up.

³For comparison, the interconnection of three standard screen-printed and bifacially-contacted solar cells by solder-based tabbing and stringing process results in a drop of the fill factor by about 4% absolute. For this, we interconnect three $156 \times 156 \text{ mm}^2$ cells with three 1.5 mm wide ribbons. The average of the fill factor before interconnection is 77.5% . The fill factor of the module after interconnection is 73.4% . Similar values are reported in Ref. [150, 151].

the individual fingers has to flow along the busbar to the pads. Omitting this current path reduces the resistive losses.

Again, we observe no changes in the open-circuit voltage between the measured and expected values of the module. The reduction of the short-circuit current of 4% is caused by the reflection at the front side of the module glass.

Even though the interconnected solar cells have a thickness below 100 μm , the interconnection by the AMELI laser welding process is possible without significantly damaging the cells. We showed this also for 34 μm thick solar cells in reference [152]. The advantage of the AMELI process is that the heat is only applied locally and not in the whole interconnect. The thermomechanical stress due to the difference in thermal expansion coefficients is much lower and does not induce any damage during interconnection.

6.1.3 Artificial aging

The interconnection of BJBC solar cells using both types of substrates shows no damage. However, the modules have to sustain the environmental conditions for 25 years. In order to investigate failures that could occur during the lifetime of a module, we artificially age the modules. Additionally to the variation of the substrate type (glass or lamination foil), we use two different processes for cell metallization.

Impact of the cell metallization process on reliability

We apply two types of Al cell metallization to our BJBC solar cells:

- Evaporation by electron beam - We use a BAK-EVO system (Unaxis) with a calotte rotating at 20 rpm. The deposition rate is 5 nm/s. We measure a maximum temperature of approximately 125 $^{\circ}\text{C}$ and a pressure below 6×10^{-6} mbar. The thickness of the Al layer is 25 μm on the finished cell.
- Thermal evaporation - This is performed in the same high rate in-line metallization system as used for the metallization of the glasses. However, in order not to reach too high temperatures⁴, we use a dynamic deposition rate of 5 $\mu\text{m} \times \text{m}/\text{min}$ at a tray speed of 3 m/min and twelve oscillations for the 20- μm -thick Al metallization. This evaporation process leads to a maximum Si-wafer temperature of about 350 $^{\circ}\text{C}$.

Figure 6.5 shows SEM images of the surface of the two metallizations. The difference in surface morphology can be explained by the zone models for the growth of physical vapor deposition (PVD) of metal films [154]. Lower temperatures ($< 0.5 \cdot T_m = 467 \text{ K} = 193 \text{ }^{\circ}\text{C}$) during deposition lead to a growth process dominated by surface diffusion. This results in a growth of columnar grains separated by distinct intercrystalline boundaries, which is the case for the electron beam deposition. However, for higher temperature regimes ($> 0.5 \cdot T_m$) bulk diffusion governs the growth process. As in the case of the thermal evaporation process, it results in less distinct intercrystalline boundaries, a more compact structure, and a smoother surface.

⁴Too high temperatures have the potential to affect the passivation properties of the dielectric layers or even result in solution of Si in Al by the formation of an Al-Si eutectic [153]. The latter effect can cause shunting of the solar cell.

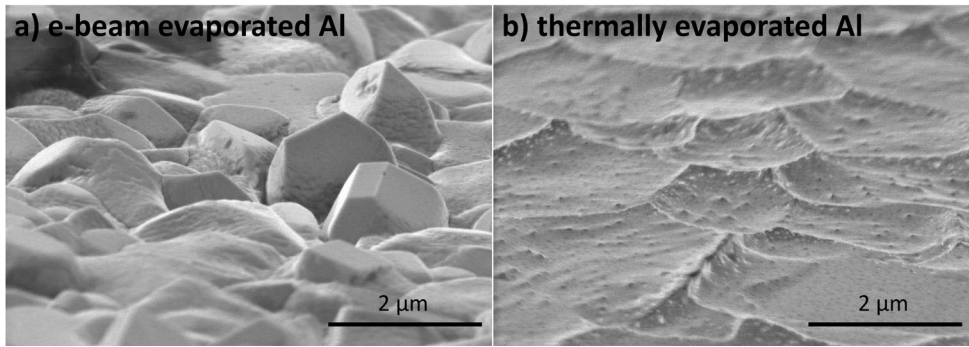


Figure 6.5: SEM image of 20- μm -thick Al films on a silicon substrate deposited a) by electron beam evaporation and b) by thermal evaporation. The samples are tilted such that the image is at an angle of 15° of the incident electron-beam relative to the sample's surface.

We fabricate modules with BJBC solar cells metallized by electron beam and thermal evaporation and use glass substrates. The finished modules are laminated using a silicone encapsulant on the front side and a transparent frontsheet (Isovoltaic 2754T). Figure 6.6 depicts the dependence of the characteristic I - V -parameters on the number of humidity-freeze cycles. In the case of the cold deposition of the aluminum by electron beam, a fast degradation of the fill factor and the short-circuit current can be observed in Fig. 6.6 a). After ten cycles, the efficiency decreases by 7% relative to the initial value. This is mainly due to a reduction of the fill factor. After 100 cycles the module does not generate power any more. Figure 6.6 b) shows a photograph of the rear side of the module after 100 humidity-freeze cycles. The bright areas on the Al metallization of the solar cell appear similar to the initial state before aging. The dark areas however, which cover almost the entire surface, show a high level of degradation, i.e., chemical corrosion. The aluminum is lifted off from the cell's surface (rippled structure) and the contact between the Al on the cell and the silicon is lost.

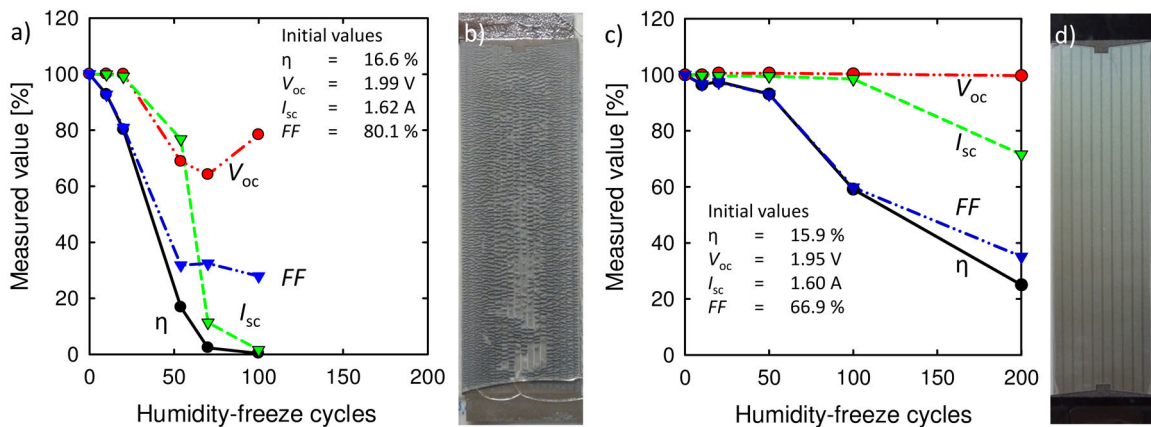


Figure 6.6: Relative module parameters compared to initial values in dependence on the number of humidity-freeze cycles. a) Module fabricated on glass substrate using BJBC solar cells with electron beam evaporated Al and with a cell area of 155 cm^2 ; and c) module fabricated on glass substrate and using BJBC solar cells with thermal evaporated Al and with a cell area of 131 cm^2 . The photographs show the rear sides of the solar cells b) metallized by electron beam evaporation and d) metallized by thermal evaporation after 100 and 200 cycles, respectively.

The short-circuit current of the module fabricated with cells metallized by thermal evaporation is constant up to 100 humidity-freeze cycles and decrease to 72% after 200 cycles, as shown in Fig. 6.6 c). The open-circuit voltage is unaffected by the aging (maximum variation 0.5% relative). However, the fill factor decreases with an increasing number of cycles down to 35% of the initial values. This results in a reduction of the efficiency η of 75% relative to the initial value after 200 cycles. The rear side of the solar cell shown in Fig. 6.6 d) reveals that the cell metallization appears unchanged compared to the initial state. No sign of corrosion is visible. These efficiency losses exceed the 5% tolerated for 200 thermal cycles by the IEC 61215 norm.

Comparing the two modules fabricated on glass reveals that the aluminum layer deposited by thermal evaporation at about 350 °C is more resistant to degradation than the one deposited at lower temperature using the electron beam evaporation. This can be explained by the different growth processes leading to different properties of the Al layers. However, a degradation of the modules on the glass substrate even with thermally evaporated Al is detected. We observe a significant decrease of the fill factor after 200 cycles of 75% relative.

Impact of the substrate type on reliability

One explanation for the degradation of the modules fabricated on glass substrates with stable Al metallization is the thermomechanical stress induced due to the difference in thermal expansion coefficients for the silicon of the solar cell and the glass substrate. Eitner et al. [155] show for solar cells ($125 \times 125 \text{ mm}^2$) and the same temperature cycles as used for aging here that the absolute difference in expansion between the glass and the solar cell is about 70 μm . This results in fatigue and damage of the laser welds bonding the cells to the glass. As a consequence, the series resistance increases and, thus, the fill factor drops.

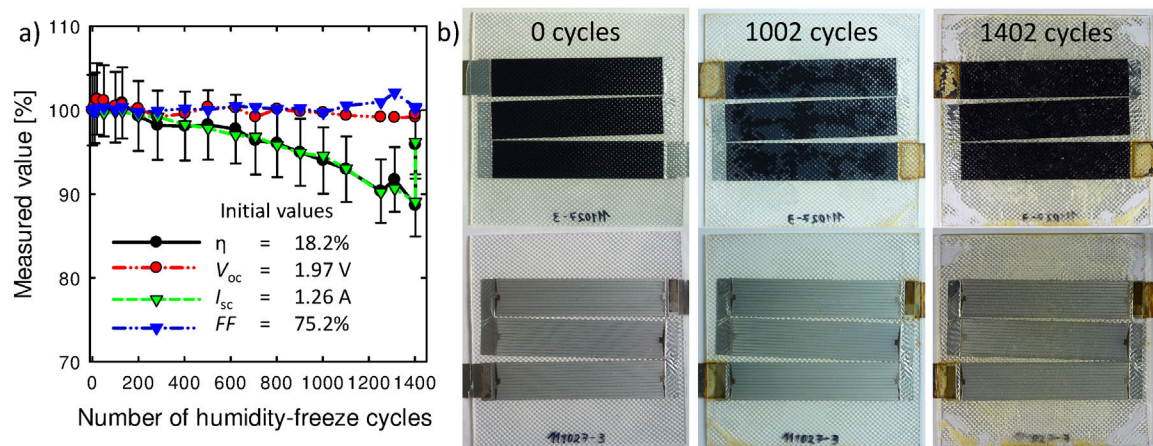


Figure 6.7: a) Relative module parameters compared to initial values in dependence on the number of humidity-freeze cycles of a module fabricated on foil substrate and using BJBC solar cells with thermal evaporated Al having a cell area of 103 cm^2 . The measurement uncertainty of the module flasher is 4.2% relative in power. After 1402 cycles the transparent front sheet is fully laminated. We measure the module with the front sheet and without the front sheet. The latter measurements shows a increase in current of 7%. b) Photographs of the front (upper row) and rear side (lower row) of the same module after 0, 1002, and 1402 humidity-freeze cycles. The photographs at 1402 cycles are without the front sheet.

To avoid this effect, we use the lamination foil as alternative substrate and fabricate a module using BJBC solar cells with thermally evaporated aluminum. In this case, the cells are fully embedded by encapsulant. We use the same transparent front sheet at the front side and a glass on the rear side for mechanical support and sealing.

Figure 6.7 a) shows the dependence of the characteristic module parameters relative to the initial values. After 200 humidity-freeze cycles no degradation (relative changes $> 0.75\%$) is detected for all module parameters. Even after 802 humidity-freeze cycles the relative change of the efficiency is only 4%. This is less than the 5% limit required for the test sequence after 200 thermal cycles.

The reduction in efficiency is only caused by a reduced current. Figure 6.7 b) shows the front and rear side of the module after different numbers of humidity-freeze cycles. A yellowing and delamination of the encapsulant is visible, which causes additional absorption and reflection and, thus, explains the reduced current [57]. A loss of 4% in I_{sc} is expected for delamination [57]. Additionally, a reaction of the encapsulant with the copper is also visible leading to a browning of the encapsulant around the Al-clad copper conductors. The reduction of the short-circuit current is not related to the interconnection process. After 1402 cycles the front side is fully delaminated. Measuring the module with the front sheet and without it shows an increase of 7%, which quantifies the impact of the delamination and degradation of the sheet in front of the solar cells. When measuring the module without front sheet, the cells are still covered by encapsulant. The efficiency of the module without front sheet after 1402 cycles is only 4% lower than the initial value before the artificial aging test. The 1402 humidity-freeze cycles exceed combined test sequence used at ISFH by a factor of 7 and the 10 humidity-freeze cycles according to IEC 61215 by orders of magnitude. Therefore, a degradation of individual module components (lamination foil and front sheet) after more than 200 cycles is acceptable.

For the development of the laser welding process, the stability of the cell interconnection is important. A degradation of the interconnection would result in a change of the fill factor due to increased series resistance. Here, the fill factor is constant (variations between -0.2% and $+2\%$) over the 1402 cycles. This proves the stability of the laser-welded interconnections. Such a high stability is also achieved by mechanically decoupling the cell from the glass by separating them using the lamination foil. The cells are also fully surrounded by the encapsulant such that no humidity can accumulate between cell and glass, which has a positive impact on the stability of the solar cells.

6.2 Single busbar modules

The AMELI process has proven to transfer the high efficiencies of the BJBC solar cells into modules, which are also stable under artificial aging when using a lamination foil as substrate. In order to improve the module efficiency, cells and module interconnection are jointly modified.

Identifying regions decreasing the cell performance of BJBC solar cells

As described in section 2.1, the busbars of the BJBC solar cells have an impact of the cell performance. In order to quantify this impact and to improve the design of our BJBC solar



Figure 6.8: Sketch of the masks used for determination of the effect of busbar and edge regions on the cell performance. The cells are measured in the I - V with the shadow masks on their front side. Here, the rear side of a BJBC solar cell is shown to illustrate the location of the mask with respect to the doping geometry, which coincides to the metallization geometry for this cells.

cells, we investigate which areas decrease the cell efficiency.

Table 6.4 shows the characteristic I - V -parameters of a BJBC solar cell measured on total area or using shadow masks excluding various parts of the cell from illumination. The first mask shades the base busbar and the remaining areas, designated area 1 (d.a.1), are illuminated, see Fig. 6.8 and Tab. 6.4. Compared to the total area measurement, the main change is an increase in the short-circuit current density. This can be explained by the absence of electrical shading, i.e., the recombination of the minority charge carriers underneath the base busbar, see section 2.1. Shading the emitter busbar (d.a.2) leads to a reduction in the series resistance R_s and, thus, an increase in fill factor. Shading the non-busbar edges (d.a.3) has only a minor effect on the cell performance compared to the total area measurement. In the case all four edges are shaded (d.a.4), the effects accumulate and the efficiency increases by more than 1% absolute to $\eta = 21.3\%$. The efficiency gains by shading the base or emitter busbar are similar with 0.6% and 0.5% absolute, respectively. However, these BJBC solar cells suffer mainly from a reduced fill factor and, therefore, we omit the emitter busbar in the next development step. Omitting the emitter busbar requires that each emitter finger is contacted individually.

Table 6.4: I - V -parameters measured under standard testing conditions (100 mW/cm^2 , 25°C) of a n -type BJBC solar cell with different parts of the cell illuminated during the measurement. The excluded areas are shaded by different shadow masks. Abbreviations used: Designated area d.a., cell area A , emitter busbar emit. bb, base busbar base bb, non-busbar edges non-bb edge, efficiency η , fill factor FF, series resistance R_s , open-circuit voltage V_{oc} , and short-circuit current density J_{sc} . \checkmark means the area is included, \times the area is excluded.

	A [cm ²]	emit. bb	base bb	non-bb edge	η [%]	FF [%]	R_s [Ωcm^2]	V_{oc} [mV]	J_{sc} [mA/cm ²]
d.a.1	152.1	\checkmark	\times	\checkmark	20.8	77.0	1.2	667	40.5
d.a.2	152.1	\times	\checkmark	\checkmark	20.7	77.7	0.9	667	40.0
d.a.3	153.3	\checkmark	\checkmark	\times	20.2	76.2	1.2	667	39.8
d.a.4	147.2	\times	\times	\times	21.3	77.9	0.8	667	40.9
total	155.1	\checkmark	\checkmark	\checkmark	20.2	76.0	1.4	668	39.8

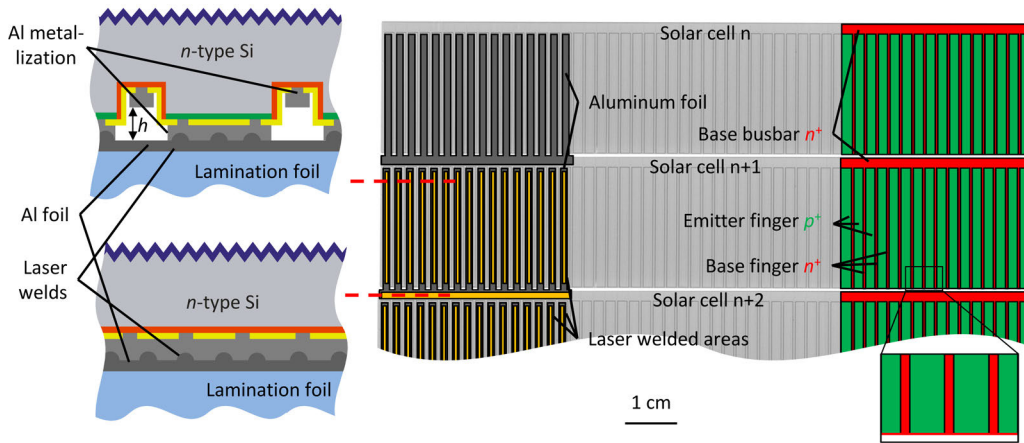


Figure 6.9: Schematic of the interconnection of BJBC solar cells with one busbar by laser welding. On the right side, the rear side of the solar cells is shown, where the n^+ -regions (red) and the p^+ -regions (green) are schematically indicated. Additionally, the structure of the Al foils is given (dark gray) and in orange the laser-welded areas. The laser-welded areas are indicated for the solar cells n+1 and n+2 such that the Al foil is visible on solar cell n. In a module all cells are laser welded. The magnification indicates the remaining base area at the end of the emitter finger, which serves as tolerance area during laser dicing of the cells. The dashed red lines indicate the locations of the two cross-sections (left side), where the base and emitter regions are contacted, respectively. h denotes the height difference between n^+ -regions and the p^+ -regions. The cross-sections are not in scale.

Module interconnection by contacting individual fingers

To show that the interconnection of the individual fingers is possible, we fabricate solar cells that are adapted to the interconnection process. Five cells are fabricated on one wafer. The cells have a final size of $24 \times 125 \text{ mm}^2$. The process is changed such that the height difference h between base and emitter region is reduced to $6 \mu\text{m}$ (formerly $20 \mu\text{m}$), see Fig. 6.9. This is required since the base and emitter regions that are laser welded to the Al foil, i.e., the base busbar and the emitter finger, are close to each other, see Fig. 6.9. A too large height difference could result in a gap between the metal layers and, thus, in reduced quality of the laser weld. Since the cell strips are now laser diced perpendicular to the fingers and, thus, the finger length is reduced to 23 mm, we use a cell metallization with a thickness d_{Si} of $10 \mu\text{m}$ instead of $25 \mu\text{m}$. A direct comparison to the base line cells is not possible due to these changes.

The Al foil on the encapsulant is structured into a comb structure using μs laser 2, see section 3.2. The same Al foil piece that contacts the base busbar of one cell is in contact with the individual emitter fingers of the next cell, see Fig. 6.9. We also use the μs laser 2 for laser welding. We weld the individual fingers using a pitch between the weld spots of $100 \times 100 \mu\text{m}^2$ and a fluence of 55 J/cm^2 .

We first fabricate a mini-module with five single busbar cells, as shown in Fig. 6.10. For external connection, Al-clad copper conductors are laser welded to the Al foil. Since the cells have no emitter busbar, they cannot be measured before interconnection using our I - V -tester. Table 6.5 shows the I - V -parameters of the module after interconnection. The mini-module reaches a fill factor of 78.1%. This indicates that the omission of the busbar increases the fill factor as expected. An efficiency of 20.1% is reached before lamination. This efficiency is mainly limited by the low value of $I_{\text{sc}} = 1169 \text{ mA}$, which corresponds to

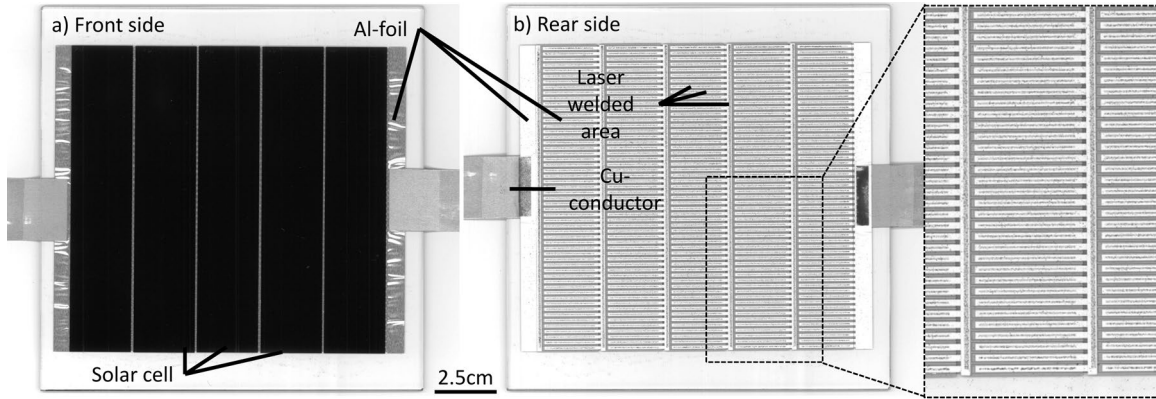


Figure 6.10: Photograph of the a) front side and b) rear side of a module consisting of five single busbar BJBC solar cells. Additionally, a magnification of the structure is given.

a short-circuit current density of 39 mA/cm^2 . Reasons for this might be the non-optimized base busbar with an area fraction of more than 4% as well as losses at the laser-diced edges.

After lamination, the module shows a decreased efficiency due to absorption and reflection reducing the current. Additionally, the fill factor is reduced. We observe similar, but more pronounced, effects for other modules (not shown here). There, we detect local shunts at a small area of the base region on the edge opposite to the base busbar. It is the location, where the Al foil contacting the emitter fingers passes over the cell edge, see magnification of the cells in Fig. 6.9. This area serves as a tolerance area to avoid a damage of the emitter region during laser dicing through the base busbar. Nevertheless, a shunt between this small base region and the Al foil can be omitted by etching the Al metallization at this area during contact separation. This would avoid that the Al foil is in contact with both polarities.

Table 6.5: I - V -parameters measured under standard testing conditions (100 mW/cm^2 , 25°C) of modules fabricated with single busbar n -type BJBC solar cells interconnected on a foil substrate using laser welding. The uncertainty of the module flasher is only known for the power at the maximum power point (MPP). Abbreviations used: Cell area A , efficiency η , fill factor FF, open-circuit voltage V_{oc} and short-circuit current I_{sc} .

	Number of cells	A [cm^2]	η [%]	FF [%]	V_{oc} [mV]	I_{sc} [mA]
Module	5	150	20.1 ± 0.8	78.1	3305	1169
Module laminated	5	150	19.3 ± 0.8	77.6	3306	1132
Module	12	389	18.9 ± 0.8	78.1	7831	1105
Module laminated	12	389	18.2 ± 0.8	76.2	7822	1095

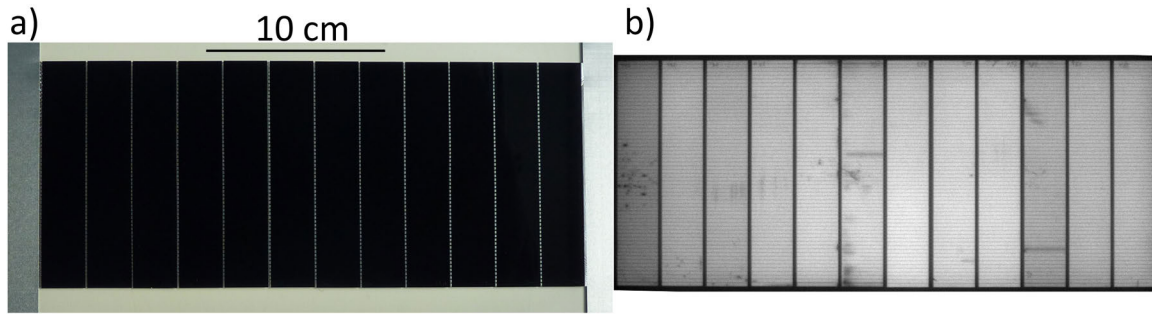


Figure 6.11: a) Photograph of the front side of a module consisting of twelve single busbar BJBC solar cells and b) the corresponding EL image taken at an applied voltage of 6.8 V. Both images are in the same scale.

Reproducibility of module interconnection by contacting individual fingers

So far, we presented modules consisting of up to five cells. In order to show the reproducibility of the welding method and a step towards upscaling of the AMELI process, we produce a module of twelve single busbar cells. Figure 6.11 a) shows a photograph of the module consisting of twelve cells. Additionally, the electroluminescence image taken at an applied voltage of 6.8 V is shown. One observes that all emitter fingers are bright in the EL image, indicating that all fingers are contacted. Two black lines are visible in the image. For both of these, the emitter fingers below and above emit light. Therefore, we assume that finger interruptions in the metallization of two base fingers cause the dark lines. Together with a fill factor as high as in the case of the five cell module, see Tab. 6.5, this proves the reproducibility of the laser welding process, even in the case of contacting 720 individual fingers (12 solar cells, each with 60 fingers).

6.3 Busbar-free modules

After we have shown that it is possible to contact the individual finger of the solar cell, we now interconnect busbar-free BJBC solar cells to avoid also the electrical shading effect due to the base busbar. The starting point are full-square n -type BJBC solar cells ($125 \times 125 \text{ mm}^2$) fabricated with two busbars and a metallization thickness of $d_{\text{Si}} = 25 \mu\text{m}$. Since we contact here the base fingers on their whole length, it is favorable that the base and not the emitter regions protrudes from the rear side. A cross-section of the cell structure is shown in 6.13. This requires a change in the process flow [119]. The solar cells are measured with the I - V -tester on total area (t.a., 156.25 cm^2) and on designated area (d.a., 132.67 cm^2) using a shadow mask, which excludes the two busbars and the two non-busbar edges, similarly to the cell measurement on designate area 4 (d.a.4) in Fig. 6.8.

By laser dicing, we cut off the busbars of the solar cells and divide the remaining central part in four cell strips perpendicular to the fingers. These cell strips have an area of $25 \times 125 \text{ mm}^2$ and are free of busbars. Four solar cells (initial efficiency between 20.4% and 21.2%) are laser diced in order to fabricate four modules. The four cell strips out of each cell are interconnected in series into the same module. This enables a comparison of the large

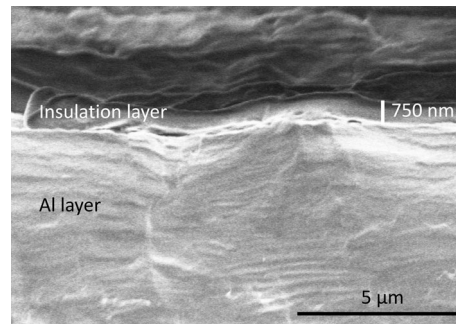


Figure 6.12: Example of an SEM image showing the cross-section of an Al layer covered with a thin insulating layer. A fast scan instead of a high resolution image is used in order to minimize a electrical charging of the insulating polymer layer.

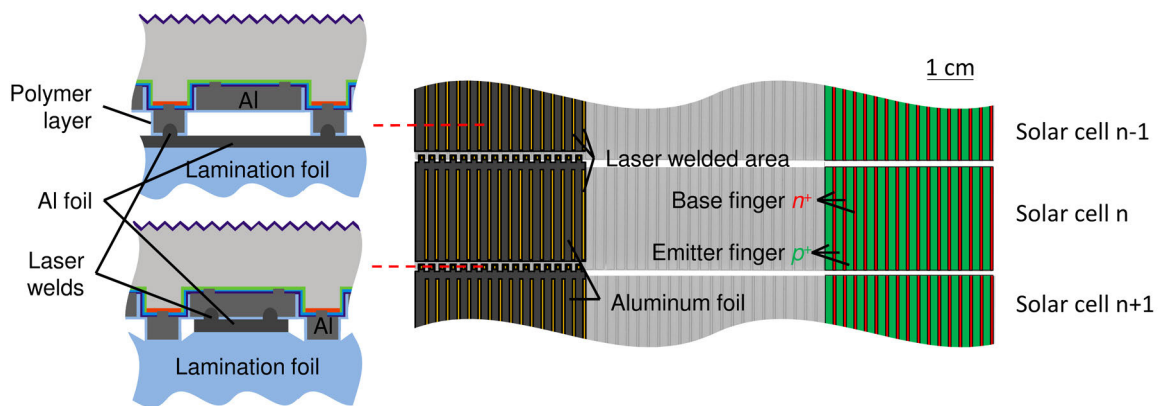


Figure 6.13: Schematic of interconnection of busbar-free solar cells by laser welding. On the right side the rear side of the solar cells is shown. The two polarities are schematically indicated in red (n^- -regions) and in green (p^+ -regions). Additionally, the structure of the Al foils is given (dark gray) and of the laser welded areas (orange). The dashed red lines indicate the locations of the two cross-sections (left side), where the base and emitter regions are contacted, respectively. The cross-sections are not to scale.

area cell before laser dicing and the resultant module. We deposit a SiN_x layer at a low temperature⁵ in order to reduce the recombination losses at the laser-diced edges. However, we perform no etch-back of the laser damage. A thin polymer layer is applied to the rear side of the solar cells. It acts as an insulating layer between the cell metallization and the Al foil and enables a sealing of the rear side after lamination. The polymer is an encapsulant (Tectosil, Wacker) dissolved in isopropanol and applied in liquid state. The thickness of this layer after drying under ambient conditions is 750 ± 350 nm as determined using SEM images. Figure 6.12 shows an example of a cross-section through such an insulating layer on top of the Si wafer (not shown) with an Al layer deposited by thermal evaporation.

Figure 6.13 shows a schematic of the interconnection in the case of busbar-free BJBC solar cells. The structure of the Al foil on the lamination foil substrate is shown in gray. The ratio between base and emitter finger width is 5:18 and the period of the finger structure p_f is $2300 \mu\text{m}$. Since the doping and metallization geometry coincide, the metal fingers trans-

⁵The solar cells are placed during SiN_x deposition on a heating plate with a set temperature of 360°C in a PECVD reactor from Oxford Plasma Technology.

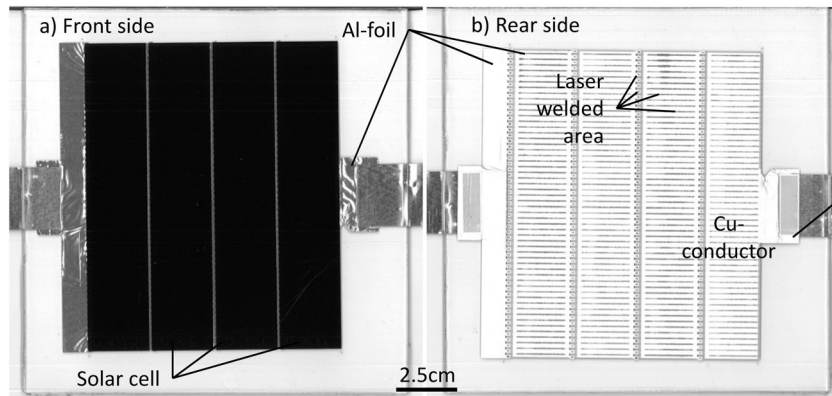


Figure 6.14: Photograph of a) the front side and b) the rear side of a module consisting of four busbar-free BJBC solar cells.

porting the current collected in the base region are much narrower than the metallization carrying the current collected in the emitter regions. The Al foil covers nearly the whole rear side of the solar cell and contacts the base fingers, as shown in Fig. 6.13. Thereby, the interconnection structure supports the current flow of the base region in order to reduce the resistive losses within the narrow fingers. Shunts in this region between the emitter Al fingers and Al foil are avoided by the thin insulation polymer layer. The same piece of Al foil that contacts the base fingers of one cell is in contact with the emitter fingers of the next cell. Here, the Al foil is structured in such a way that it is only on top of the emitter metallization and fits in between the base fingers, see lower cross-section on left-hand side in Fig. 6.13. We laser weld using μs laser 2 with a fluence of $F = 73 \text{ J/cm}^2$ and a pitch of $100 \times 100 \mu\text{m}^2$. The laser welds pierce through the polymer layer as well as the dielectric layers⁶ on the cell metallization to form the weld spots. The finished modules are characterized before and after lamination using the module flasher. Figure 6.14 a) and b) show the front and rear side of the module after lamination, respectively. Darker areas are visible on the rear side, where the laser welded the Al layers.

Table 6.6 gives the I - V -parameters of a BJBC cell with two busbars before laser dicing and interconnection. Additionally, it shows the parameters of the module fabricated with the strips diced out of that cell. The I - V -parameters of the module are related to the open-circuit voltage and the short-circuit current density of the individual cells for a convenient comparison. We assume a loss-free interconnection of the cells in series and an equal performance of all cells. Therefore, we divide the open-circuit voltage of the module by the number of cells to obtain the $V_{\text{oc}}/\text{cell}$. Since the current is constant over all cells in the case of series interconnection, but the current density in the module is related to the cell area of all cells interconnected, the short-circuit current density is multiplied by the number of cells to obtain the $J_{\text{sc}}/\text{cell}$.

Comparing the open-circuit voltage of BJBC cells before dicing on total area with the module before lamination, the changes are below 2 mV and, thus, within the measurement uncertainty, see Tab. 6.6. The short-circuit current density in the case of the module before lamination (40.1 mA/cm^2) is as high as in the case of the cell measurement on total area (40.2 mA/cm^2). Recalling however the effects of electrical shading, see section 2.1, an in-

⁶ SiO_x layer required for contact separation, see section 3.3.2, and SiN_x layer for passivation of laser-diced edge, see above.

Table 6.6: I - V -parameters measured under standard testing conditions (100 mW/cm^2 , 25°C) of n -type BIBC solar cells before and after module integration on a foil substrate using laser welding. The cell and module values correspond to module 1 in Fig. 6.15. Abbreviations used: Total area t.a., designated area d.a., cell area A , efficiency η , fill factor FF, open-circuit voltage V_{oc} , and short-circuit current density J_{sc} . The cells are measured using the LOANA system and the modules using the module flasher with their corresponding measurement uncertainties.

	A [cm ²]	η [%]	FF [%]	V_{oc} [mV]	V_{oc}/cell [mV]	J_{sc} [mA/cm ²]	J_{sc}/cell [mA/cm ²]
Cell t.a.	156.25	21.2±0.6	77.0±0.8	686±3		40.2±1.1	
Cell d.a.	132.67	22.1±0.7	78.1±0.8	684±3		41.4±1.2	
Module	125	22.1±0.9	80.5	2740	685	10	40.1
Module laminated	125	21.0±0.9	80.8	2728	682	9.52	38.1

crease of the short-circuit current density is expected by omitting the base busbar, i.e., it is supposed to be as high as for the designated area measurement. Comparing the cell measurement on designated area (41.4 mA/cm^2) with the module measurement (40.1 mA/cm^2) there is a relative reduction of 3%.

The fill factor of the cell measured on total area is 77.0%. After laser dicing and interconnection it is increased to 80.5%. This corresponds to a relative increase of 5% and compensates the losses in the short-circuit current. The efficiency of the module before lamination is as high as the efficiency of the cell measured on designated area. Compared to the total area measurement there is a relative increase in efficiency of 4%.

The relative change of the module I - V -parameters compared to the cell measurements as well as between the unlaminated and laminated module are also given in Fig. 6.15. Module 1 corresponds to the same module as given in Tab. 6.6. Additionally, the relative changes of the other three modules are given. In the following subsections, we are going to analyze and discuss the change of the individual module I - V -parameters in detail.

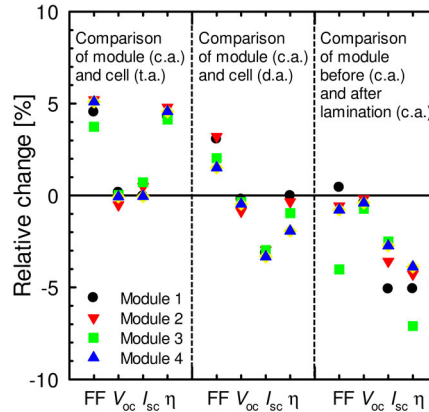


Figure 6.15: Relative changes of the I - V -parameters between the non-laminated modules taking into account the active cell area (c.a.) and the initial cell measured on the total area (t.a.), designated area (d.a.), and the module after lamination for the four modules we produced. Positive values correspond to an increase in the I - V -parameters of the module compared with the initial cell. In the case of the comparison of the modules before and after lamination, the negative values correspond to losses after the lamination process.

6.3.1 Fill factor

The most significant change in the I - V parameters due to the module integration of the busbar-less cell strips is in the fill factor. Comparing the cell measurements (t.a.) and the module before lamination reveals a relative increase of 3.7% to 5.2% (an absolute increase of 2.9% to 4.0%), see Fig. 6.15. We identify two main reasons for the reduction of the series resistance leading to an increase in fill factor:

- The absence of the emitter busbar:
The majority charge carriers, which are generated above the emitter busbar, have to travel a certain distance to the next base region and experience an additional resistance on their path. This has a negative impact on the fill factor. Comparing the fill factor of the cell measurement on designated and total area shows a relative gain of 1.1%, see Tab. 6.6. According to Tab. 6.4, this change can largely be attributed to the emitter busbar. In the case of the cell used for module 1, the change in series resistance between the total and designated area measurement is $320 \text{ m}\Omega \text{ cm}^2$. This is mainly caused by the current generated above the emitter busbar⁷.
- The reduction of absolute current and path length in the metallization:
In the case of the standard interconnection by soldering of BJBC solar cells, the current is conducted within the busbars to the solder pads (see Fig. 6.1), where the cell is contacted during measurements. Here, all fingers are connected to the Al foil on the full width. The conductive losses, which would appear in the busbars to the solder pads perpendicular to the fingers, are omitted. The current path is only parallel to the fingers. Additionally, the length of the fingers is reduced from 120 mm to 25 mm. This results in a relative increase of the fill factor of 3.1% (2.4% absolute) when comparing the cell measurements on designated area and the module before lamination, see Tab. 6.6.

Since the latter effect has the larger impact and is directly related to the interconnection and not to the cell structure, we focus on the resistive losses in the metallization in the following. We approximate the variation of the fill factor due to a change in series resistance ΔR_s under the assumption that the series resistance reduces the voltage at a constant current. Hence, it holds at the maximum power point (MPP)

$$\Delta V_{\text{mpp}} = J_{\text{mpp}} \cdot \Delta R_s \quad (6.1)$$

with V_{mpp} and J_{mpp} being the voltage and current density at MPP. Here, R_s is the area-weighted series resistance in units of $\Omega \text{ cm}^2$. The change in fill factor ΔFF can then be calculated via

$$\Delta \text{FF} = \frac{\Delta V_{\text{mpp}} \cdot J_{\text{mpp}}}{V_{\text{oc}} \cdot J_{\text{sc}}} = \frac{\Delta R_s \cdot J_{\text{mpp}}^2}{V_{\text{oc}} \cdot J_{\text{sc}}}. \quad (6.2)$$

In the case of the finger metallization, we assume a continuously increasing current, since the contact openings of the passivation under the metallization are continuous. We determine

⁷The change in fill factor due to the absence of the emitter busbar is influenced by changes in series and shunt resistance. Since the shunt resistance decreases when measuring the cell with shaded parts (d.a.), the increase in FF is lower than what is calculated from the series resistance above according to equation 6.2.

the series resistance by [156, 157]

$$R_s = \frac{1}{3} \rho \frac{p_f l_f^2}{A_f}, \quad (6.3)$$

where ρ is the resistivity of the conducting layer. The resistivity of evaporated aluminum is $\rho = 3.2 \mu\Omega\text{cm}$, see section 4.2.3 or reference [138]. The geometry of the finger is given by its cross-section A_f perpendicular to the current flow, the finger length l_f , and the period of the finger structure p_f . This period is also the width of the unit cell from which the current is collected.

In the case of the resistive loss within the busbars towards the solder pads, a continuous increase of the current cannot be assumed. Only nine fingers⁸ sequentially transfer their current to the busbar. Therefore, the resulting power losses of the n individual segments between the fingers $P_{\text{loss},k}$ add up to the total loss in the busbars

$$\Delta P_{\text{bb}} = R_{\text{sa}} \cdot I^2 = \sum_{k=0}^n P_{\text{loss},k}, \quad (6.4)$$

where I is the total current in the busbar and R_{sa} is the total absolute resistance in units of Ω . The loss in the k^{th} segment of the busbar is

$$P_{\text{loss},k} = (k j l_f p_f)^2 \rho \frac{p_f}{A_{\text{bb},k}}, \quad (6.5)$$

with j the current density and $A_{\text{bb},k}$ the cross-section area of the corresponding busbar segment perpendicular to the direction of the current flow.

Table 6.7 summarizes the calculated values for the series resistance of the initial cell and the cell strips contacted with the Al foil. In the case of the cell strips, the base fingers are laser welded to the Al foil that contributes to the current transport. As an upper limit the resistivity of the Al foil is assumed to be the same as the resistivity of the evaporated layers.

Table 6.7: Series resistance R_s calculated on cell level assuming the initial cell ($125 \times 125 \text{ mm}^2$) with busbars and 120-mm-long fingers. Additionally, the series resistance for the cell strips ($25 \times 125 \text{ mm}^2$) on module level is given. The fingers are 25 mm long and the impact of the Al foil welded to the base fingers is included. The given uncertainties take the uncertainties of the geometry into account.

		R_s [$\text{m}\Omega \text{ cm}^2$]
Cell level	Base busbar	86 ± 4
	Emitter busbar	78 ± 4
	Base finger ($l_f = 120 \text{ mm}$)	297 ± 20
	Emitter finger ($l_f = 120 \text{ mm}$)	80 ± 3
	Total cell	541 ± 31
Module level	Base finger ($l_f = 25 \text{ mm}$)	4.5 ± 0.1
	Emitter finger ($l_f = 25 \text{ mm}$)	3.5 ± 0.1
	Total module	7.9 ± 0.1

⁸The solar cells have a width of 125 mm and feature three solder pads per busbars of each polarity, see Fig. 6.8. The current flows from tow sides towards the pads, i.e., the busbar can be separated into six segments. Using $p_f = 2.3 \text{ mm}$ each segment carries the current of nine fingers.

Comparing the sum of the series resistances on cell and module level shows a difference $\Delta R_s = 533 \pm 31 \text{ m}\Omega\text{cm}^2$. According to equation 6.2, the resulting increase of the fill factor ΔFF is $2.7 \pm 0.2\%$ under the assumption of the I - V -parameters given in Tab. 6.6 for the cell (t.a.) and its current density at MPP of $J_{\text{mpp}} = 37.4 \text{ mA/cm}^2$. For module 1, the measured absolute differences in fill factor between the cell (d.a.) and the modules before lamination is $2.4 \pm 0.8\%$ ⁹, see Tab. 6.6. The comparison is done with respect to the designated area measurements because they omit the effects due to charge carrier generation and conduction above the busbars. The calculations are in good agreement with the measured value for module 1. This holds also for the other three modules with a difference in FF between the cell (d.a.) and the module before lamination between 1.2% and 2.5% (relative changes of 1.5 – 3.2%, see Fig. 6.15).

However, the minor variations between calculation and measurements may result from the following effects:

- The laser dicing of the cell may lead to shunt-like defects that have an impact on the fill factor of the solar cells.
- The contribution to the series resistance by the interconnects between the cells are not included in the calculations, in order to keep the components comparable to the large area cell. However, these contributions are small compared to the series resistance effects due to the cell metallization. In detail the minor contribution (see also Fig. 6.14 b)) to the series resistance are¹⁰:
 - the Cu conductors for external connection on both sides ($\approx 3 \text{ m}\Omega \text{ cm}^2$),
 - the Al foil between the outer cells and the Cu conductors¹¹ ($\approx 8 \text{ m}\Omega \text{ cm}^2$),
 - the Al foil between individual cells ($\approx 1 \text{ m}\Omega \text{ cm}^2$), and
 - the contact resistance between the Al foil and the cell metallization assuming a laser-welded area of about 0.5% for the emitter region and 10% for the base regions ($\approx 2 \text{ m}\Omega \text{ cm}^2$).

In sum their effect on the fill factor is only minor ($\Delta\text{FF} = 0.07 \pm 0.02\%$ absolute).

- The fill factor is affected by different parameters, i.e., series resistance, shunt resistance, recombination processes, and other. Their interaction is not always linear so the different effects may also not sum up linearly.

Nevertheless, the enhanced fill factor can be attributed to a large extent to the decrease of the series resistance within the metallization of the cell strips interconnected on the Al foil.

⁹We consider as a lower limit of the uncertainty in fill factor only the uncertainty of the I - V -tester of 0.8% absolute, since the uncertainty of the module flasher is unknown, but probably as high as for the I - V -tester.

¹⁰The resistive components that are related to the current conduction on module level are rescaled to cell level for a better comparability.

¹¹As visible in Fig. 6.14 b), the structure of this foil parts are not optimized and the contribution by them in a large-scale module will be much smaller by reducing the distance between the last cell and a thick string interconnect. Current crowding and current flow perpendicular to the fingers is not included.

Comparison to device simulations

In order to evaluate the upper limiting contributions to the fill factor in the used solar cell design, especially due to the internal series resistance within the bulk Si, we perform numerical 2D simulations using SENTAURUS DEVICE [158]. The model presented by Ohrdes et al. [159] takes into account the measured Si wafer properties, doping profiles, passivation properties of the dielectric layers, and the geometric dimensions. The detailed input parameters are given in appendix A.7. The simulation domain is a unit cell including half of a base and half of an emitter finger. Therefore, we simulate the central area of the solar cells and ignore edge effects and effects due to the busbars. We choose the optical generation in such a way that the short-circuit current density matches the measurements on designated area from Tab. 6.6. The simulations with the given input parameters lead to an open-circuit voltage of 691 mV that is in agreement with the measured values, which is reduced by marks and scratches on the undiffused cell front side.

The simulations of the J_{sc} - V_{oc} -characteristics of the cell under illumination result in a pseudo fill factor (pFF) of 83.7%, which is not affected by the series resistance. This value is higher than the measured pseudo fill factor of the cell (d.a.) pFF = 82.7%. Explanations for the difference are for example shunt effects occurring on the real solar cell and effects due to the shaded region of the solar cells on designated area, which are ignored in the simulations. The simulated I - V -characteristics, which include only the internal series resistances within the bulk Si of the solar cells, result in a fill factor of 81.8% and a total series resistance $R_s = 361 \text{ m}\Omega \text{ cm}^2$. Including the contact resistance between the silicon and the Al results in a FF = 81.3% and a total series resistance $R_s = 433 \text{ m}\Omega \text{ cm}^2$. The series resistance contribution of the Al Si contact is therefore $72 \text{ m}\Omega \text{ cm}^2$. Here we use the measured area fraction of the contacts and a contact resistance of $0.27 \text{ m}\Omega \text{ cm}^2$. We use the 2D simulation to determine the order of magnitude of the internal resistance and do not process different cell structures to validate the simulations. Therefore, the gained results serve well as approximation, but uncertainty is unknown.

Since the simulated fill factor neither includes edge and busbar effects nor resistive losses within metallization, it represents an upper limit for the used solar cell concept. The difference between the pseudo fill factor and the fill factor of the simulated results is pFF - FF = 83.7% - 81.3% = 2.4%. A comparison of the measured difference of the pseudo fill factor of the total cell on designated area and the fill factor on module level for module 1 (pFF - FF = 82.7% - 80.5% = 2.2%) shows that the values match well. One also has to take into account that we use different measurement tools. We attribute the absolute difference between simulated and measured results to the influence of the shunt resistance in the real solar cell. This supports the observation that the losses due to series interconnection using the AMELI process are marginal.

6.3.2 Open-circuit voltage

There are only minor changes for all given comparisons in the open-circuit voltages V_{oc} (< 1% relative change) assuming equal voltages for all cells in the module, see Fig. 6.15. The changes are within the uncertainty of the measurements done with two different measurement devices, the I - V -test of the LOANA system and the module flasher. This is in accordance with the results presented above for the two and one busbar designs, which

neither show any change in the open-circuit voltages.

Even though no significant changes in the open-circuit voltage are observed, the following minor effects may occur, which we state here for completeness. However they are difficult to quantify.

- The rear side of the solar cell is passivated by Al_2O_3 , which does not passivate the BSF and the emitter region equally well. The saturation current density determined for the emitter area is 24 fA/cm^2 , whereas on the BSF regions it is 364 fA/cm^2 . Therefore, omitting the wide base busbars may enhance the voltage.
- The laser-diced edges may not be passivated well, since we do not remove the laser damage. This has the potential to decrease the voltage.
- Inhomogeneities present on the initial cell may result in a decrease of the voltage of the whole cell. The individual cell strips are on their own voltage level after laser dicing. The voltages of the strips add up after interconnection. Thus, this could also influence the voltage.

However, compared to the changes in the fill factor and in the short-circuit current density, the variation of the open-circuit voltage due to these effects is only marginal.

6.3.3 Short-circuit current density

The short-circuit current density J_{sc} of the module before lamination shows no significant variation compared to the initial cell measured on total area ($\Delta J_{\text{sc}} < 1\%$ relative). However, since the electrical shading effects of the base busbar are omitted on module level, one would expect the current increases for cells without busbars compared to cells with busbars. Therefore, the short-circuit current density of the module with busbar-free BJBC solar cells is expected to be as high as J_{sc} measured on the designated area of the initial solar cells. However, a comparison between the cell (d.a.) and the module before lamination shows a reduction of the short-circuit current density of 3.0% to 3.3%, see Fig. 6.15.

This reduction of the current is not caused by non-contacted fingers. Such would appear in the EL image as dark horizontal lines and in the PL image as bright lines. This is not the case as shown in the example of module 1 in Fig. 6.16 a) and b). The dark marks, which are visible in the EL image, are also visible in the PL image and, thus, originate most probably from scratches on the cells.

One possible source of current loss are regions with increased charge carrier recombination. Such losses may lead to a decrease of the current density. In those regions the energy dissipation by recombination would result in an increase of the local temperature. This can be detected by infrared light-modulated lock-in thermography. Figure 6.16 c) shows an ILIT image of module 1. The same features as in the EL and PL images due to scratches, cell marking, and residuals from handling are visible. An increased signal can also be detected at the four edges of the cells, indicating heat-dissipating defects. The horizontal line scan highlights the relative increase of the ILIT signal towards the laser-diced edges and indicates the recombination there. A part of the loss in the current density can be attributed to these defects located at the non-perfect passivated edges. For the cell strips, the edge-to-area ratio is three times larger than in the case of the initial full-area cell. Furthermore, the cells are marked after laser dicing adding defects that are not present on the initial cell.

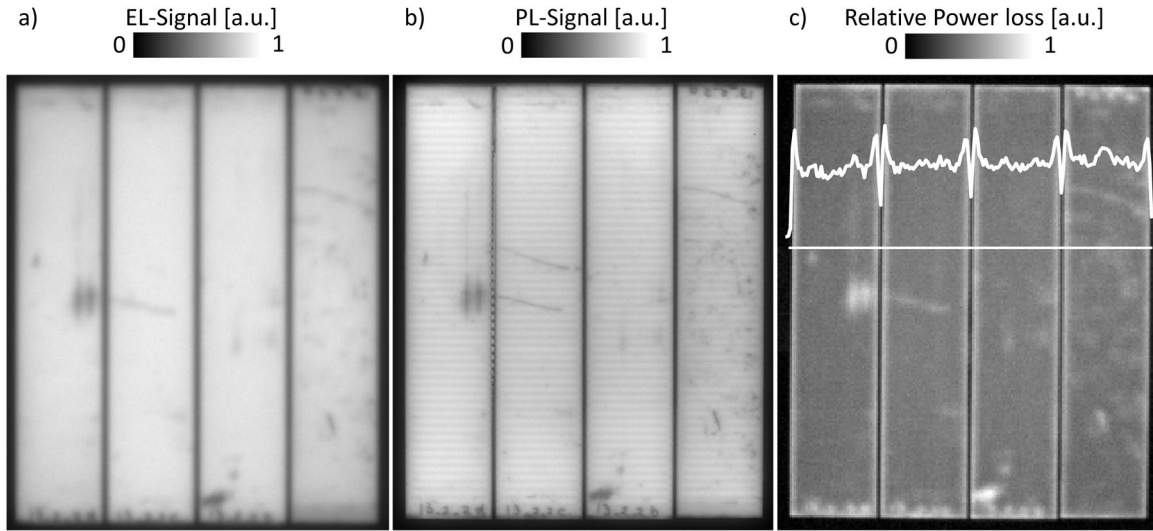


Figure 6.16: a) Electroluminescence image of the module before lamination at an applied voltage of 2.74 V. b) Photoluminescence image of the same module after lamination at open-circuit voltage. c) Infrared light-modulated lock-in thermography measurements cosine image of the four interconnected cell strips at a photon flux corresponding to one sun at open-circuit voltage. The white straight line indicates the location of the line scan, which is given in arbitrary units. All three images are on a linear scale. The three vertical lines in the EL, PL and ILIT images correspond to the interconnection gaps (Al foil) between the four cell strips of the module.

LBIC analysis of modules

The losses due to these damages, e.g., laser dicing and marking, can be quantified by laser beam induced current measurements. The technique is used in the field of crystalline Si PV to characterize individual solar cells. Here, we analyze a module, where only one cell in the string is illuminated locally and the others are in dark condition. LBIC analysis of modules is used in the field of thin film PV. It is known that the proportionality between the externally measured J_{ext} signal and photo generated current J_{ph} of the individual cells is only valid under certain conditions [160, 161]. In order to investigate if for our modules the assumption of the proportionality between J_{ext} and J_{ph} holds, we perform network simulations based on LTspice using the graphical user interface developed by Eidelloth et al. [162]. The simulated network consists of four solar cells in series, each described by the two-diode model, see Fig. 6.17 a). One cell is illuminated by a laser and generates a current J_{ph} and three other cells are in dark condition. The input parameters are based on the cell measurements before laser dicing. For the input of the photo generated current density J_{ph} , we relate the current generated by the laser spot to the total area of the irradiated solar cells. The external short-circuit current density refers to the area of one cell, too.

Figure 6.17 b) and c) show the results of the network simulation. As shown in Fig. 6.17 b) J_{ext} depends linearly on J_{ph} with an proportionality factor of 0.25. This behavior can be explained by the fact that close to 0 V the I - V -characteristic is dominated by the shunt resistance. Since in the case of n solar cells n shunt resistances are interconnected in series, it holds for small voltages ($V \approx 0$ V) $J_{\text{ext}} = J_{\text{ph}}/n$. Here, we determine J_{ext} under short-circuit condition, i.e., $V = 0$ V. Figure 6.17 c) shows that the linear dependence holds over several orders of magnitude. We observe only for values above of $J_{\text{ph}} = 10^{-5}$ A/cm² a deviation

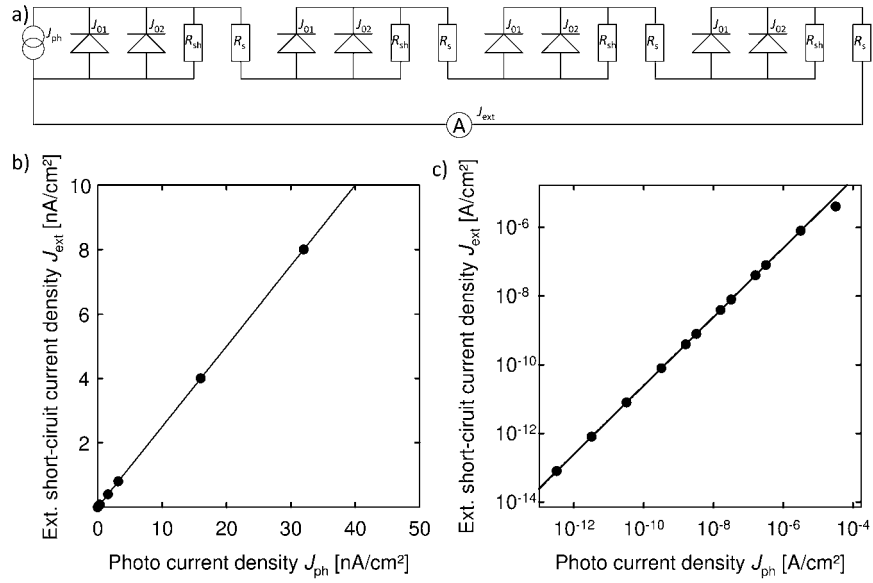


Figure 6.17: Spice network simulation of the external short-circuit current density J_{ext} for a module consisting of four solar cells in dependence on the photo generated current density J_{ph} of one solar cell. a) shows a diagram of the simulated equivalent circuit. J_{ph} is averaged over the total area of the illuminated solar cell. The used input parameters for each solar cell are extracted from the I - V -measurements of the solar cells before laser dicing. They are the dark saturation current densities $J_{01} = 9 \cdot 10^{-14} \text{ A/cm}^2$, $J_{02} = 6 \cdot 10^{-9} \text{ A/cm}^2$, the series resistance $R_s = 1.24 \Omega \text{ cm}^2$, the shunt resistance $R_{sh} = 33 \text{ k}\Omega \text{ cm}^2$, and the cell area of each solar cell $A = 31.25 \text{ cm}^2$. b) shows a linear plot of the simulation results for $J_{ext} < 10^{-8} \text{ A/cm}^2$, which is the range of the determined current density in the experiments. c) gives the simulation results in a logarithmic representation to show the dependence of J_{ext} over several orders of magnitude.

from the linear behavior. The relevant range of the detected external short-circuit current density of the LBIC measurement is between 10^{-9} to 10^{-8} A/cm^2 . Consequently, we are well within the linear regime. For values of J_{ph} above 10^{-5} A/cm^2 , the behavior of the diode is no longer dominated by the shunt resistance and the exponential behavior of the diode becomes more relevant. For larger currents, the linear relation is therefore not valid any more. Due to this, a measurement of the spectral response of the cell is not possible, since it is done with our instruments by illuminating the cell with a larger spot under, for example, 0.3 suns illumination. Hence, the given measured signal cannot be converted into absolute values of J_{sc} and is therefore treated as a relative signal in arbitrary units (a.u.).

Determination of current losses by LBIC

Since the proportionality of the detected LBIC signal to the local photo generated current is validated, we can use the technique to quantify the local current losses of the module. Figure 6.18 a) shows an example of an LBIC image at 830 nm after lamination. We make a line scan parallel to the direction of the fingers, see Fig. 6.18 b), to quantify the current loss due to the laser-diced edges. Since the module is laminated, effects that are caused by multiple reflections especially in the area between the cells occur. Therefore, we determine the dimensions of the solar cells and the gaps in a high resolution scan using a copying machine.

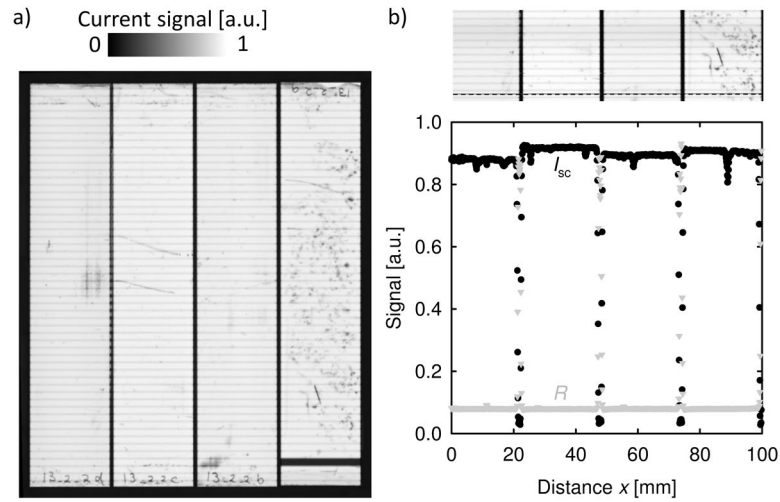


Figure 6.18: a) Light beam induced current image using laser light at 830 nm of the module after lamination. The three vertical lines correspond to the interconnection gaps (Al foil) between the four cell strips of the module. The single finger of the left cell appearing dark is decontacted only after lamination. b) High resolution LBIC image using laser light at 830 nm with a line scan of the LBIC (proportional to the short-circuit current I_{sc}) and reflectivity R . The dashed line indicates the location of the line scan in arbitrary units. All images are on a linear scale.

We quantify the relative losses due to the laser-diced edges by dividing the average signal of the whole cell width by the average signal of the central 60% of the solar cell assuming that in this region the effect due to the edge is negligible. For all wavelengths and all complete cells in the line scan, the maximal losses are $1.6 \pm 0.2\%$ relative and in the average losses are $1.1 \pm 0.2\%$ relative. The uncertainty is caused by possible misalignment of the evaluated region.

The effect of the marking is evaluated by comparing the average signal of the whole cell area with an area without the regions close to the upper and lower edges of the cells, see Fig. 6.18 a). These edges are the outer edges of the initial cell on total area before laser dicing, too. Over all cells and wavelengths, the average loss due to these parts is 0.6% relative. Two thirds (0.4%) can be attributed to the cell part that includes the marking and its neighboring edge. The remaining one third (0.2%) is related to the edge, which is on the opposite side of the marking. Under the assumption that both edges are equal, 0.2% are related to the marking. The error due to misalignment of the averaging areas is between 0.03% to 0.3% absolute depending on the homogeneity of the cells. However, the effect of the marking seems to be marginal.

The most dominant effect is the mismatch of the cells, see for example Fig. 6.18 b). Each cell strip has its own current level. Before laser dicing the cell strips are "interconnected" in parallel (they are one cell), i.e., the currents of the individual cell parts add up. However, after laser dicing and interconnection the cell strips are connected in series. In this case, an inhomogeneous current generation of the individual cell strips on module level results in a decrease of the current, since the total current of the module is limited in first order approximation by the lowest current of the individual cells in series. The relative current mismatch, which is determined on the total cell area as shown in Fig. 6.18 a), between the cell with the lowest current (first cell from left) and the one with the highest current (third cell from left) is in average over all wavelengths $5.1 \pm 0.6\%$. However, before laser dicing

Table 6.8: Overview of effects resulting in a reduction of the short circuit current density. We determine the effects on the cells by LBIC and the reflection of the glass by measuring its transmission using a spectrophotometer (Agilent Cary 5000).

	ΔJ_{sc} [%]
Cell marking	0.2 ± 0.2
Wafer edge	0.4 ± 0.2
Laser-diced edge	1.1 ± 0.2
Cell current mismatch	$1.9 - 3.1 \pm 0.6$
Reflection glass front side	3.7 ± 0.5
Reflection glass front side with ARC	1.9 ± 0.5

all cell strips are connected parallel and the short-circuit current density corresponds to the average of the individual parts. Hence, the difference in short-circuit current due to the mismatch is the difference between the average current generation of the interconnected cell strips and the one of the cell with the lowest current generation. In this case, the mismatch leads to a reduction of the short-circuit current of $1.9 \pm 0.6\%$. In fact, the effect should be larger, since the disconnected finger of the right cell influences the result. Assuming that the right cell strip has the same current generation as the cell strip with the highest current, the effect would be $3.1 \pm 0.6\%$.

These three effects (edge losses, marking, and mismatch) explain the losses of 3.3% relative comparing the solar cell (d.a.) and the module 1 before lamination. The largest of them is the cell mismatch, which can be avoided with enhanced measurement devices that are able to characterize busbar-free cells. Furthermore, cell dicing has only a minor effect on the performance of the module, enabling the reduction of resistive loss by using small cells. Table 6.8 summarizes the various effects that lead to a change in short-circuit current density.

Current losses after encapsulation

In contrast to the open-circuit voltage and the fill factor¹², the short-circuit current density and, thus, the efficiency are also affected by the lamination process, see Fig. 6.15 right side. A large fraction of the decrease in J_{sc} can be attributed to the reflection on the front side of the glass. This can be reduced to its half by using anti-reflection coatings (ARC). We apply in-house an ARC¹³ to the module 2 of Fig. 6.15. In the wavelength range between 400 nm and 1100 nm, we determine a reduction of the reflectivity of the borosilicate glass

¹²The relative change in V_{oc} and FF are less than 1%; except for the FF of module 3.

¹³It consists of a system of six sputtered layers of titanium oxide and silicon oxide (9 nm TiO₂, 54 nm SiO₂, 19 nm TiO₂, 50 nm SiO₂, 15 nm TiO₂, and 122 nm SiO₂).

from $3.7 \pm 0.5\%$ ¹⁴ to $1.9 \pm 0.5\%$ absolute due to the ARC¹⁵. We measure a relative increase of 1.4% in the short-circuit current and the module efficiency rises from 20.9 to 21.3% (1.9% relative increase). The losses due to front side reflection are partially compensated by the multiple reflection within the module. Additional losses in J_{sc} are observed for decontacting of individual fingers during lamination as in the case of module 1 and 2, see for example Fig. 6.18 a) right cell. The process needs further improvement in order to avoid any decontacting of fingers after lamination.

6.3.4 Efficiency

The four cells have an initial efficiency η on total area between 20.4% and 21.2%. After laser dicing and module interconnection, the comparison shows an increase of 0.9% to 1.0% absolute, corresponding to a relative change between 4.1% and 4.8%. This is mainly caused by the increase in fill factor. However, comparing the changes in efficiency between the designated area measurements of the initial cell and of the module before lamination, there is a decrease of 0% up to 1.9% relative, see Fig. 6.15. This is caused by the decrease of short-circuit current density resulting from the discussed effects, see Tab. 6.8.

6.4 Two dimensional contact structure

So far, the interconnected BJBC solar cells have had a finger structure on the rear side in order to transport the current to the edges of the solar cell. However, it is favorable in order to reach high efficiencies:

1. to maximize the emitter fraction so that electrical shading loss due to the BSF is reduced and the current density increases [44],
2. to minimize the distance between the neighboring BSF contacts, which reduces the lateral transport losses [163],
3. and to have equally large cross-sections of the metallizations for the two polarities in order to minimize resistive losses [47, 49].

The first two aspects can be resolved by a BJBC solar cell design having point-shaped BSF areas with a small structure size and a small pitch [48]. The third aspect can be addressed by decoupling the metallization scheme from the doping geometry [47, 49]. This can be done by buried emitter structures or insulating dielectric layers. However, the first concept requires double-diffused $p^+ - n^+$ -junctions having the potential to cause junction shunting via trap assisted tunneling [47]. In the case of the latter concept, ensuring a sufficiently high insulation on large area has proven to be challenging with commonly used dielectric layers [48–50]. As an alternative, one can apply the multi-level metallization, which is a

¹⁴The index of refraction n of the used borosilicate glass [113] is between 1.485 (400 nm) and 1.465 (1000 nm) and, hence, the theoretical reflection is between 3.81% and 3.55%, respectively.

¹⁵We measure the transmission of the glass by a spectrophotometer (Agilent Cary 5000) and assume negligible absorption within the borosilicate glass. Further, we assume in the case without ARC that both glass surfaces contribute equally to the total reflection. Hence, the reflection of the glass surfaces without coating R_{NC} is determined by $R_{NC} = (1 - T)/2$, where T is the transmission. For the glass with ARC coating, the reflection R_{AC} is determined by $R_{AC} = 1 - T - R_{NC}$.

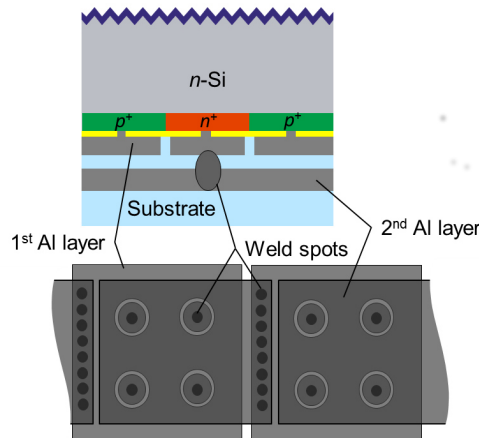


Figure 6.19: Multilayer metallization for contacting point-contacted solar cells with simultaneous module integration as done in this thesis.

rather complex process, see section 2.2.3.

We showed in the previous section 6.3 that the laser welding process is able to contact one dimensional structures of $500\ \mu\text{m}$ in size. Additionally, we implement an insulation layer between the Al foil and the cell metallization. This enables us to further engineer the cell-to-module-interface to overcome some limitations of the solar cells, e.g., by interconnection of point-contacted solar cells. Figure 6.19 shows the schematic of a multi-level metallization method, which simultaneously enables module interconnection. The first Al layer is deposited on the entire cell rear side and the p^+ - and n^+ -regions are separated by laser ablation and subsequent wet chemical etching [164]. This results in a continuous Al layer covering the whole rear side of the cell, except for the disjunct metal pads contacting the BSF areas. The layer carries the current of the emitter regions. We apply the dissolved encapsulant on the whole metal surface as described above. After drying, it insulates the two metal layers from each other. The second Al layer, carrying the current of the base regions, is realized by an Al foil that is laser welded to the individual BSF contacts. The same Al foil is contacted to the emitter metallization on the next cell, too. This enables the series interconnection.

6.4.1 Application of the multi-level metallization

For a proof-of-concept¹⁶, we use point-contacted solar cells with ion implanted emitter and BSF regions. The details of the cells are given in [166]. They feature circular BSF metal pads with a diameter of about $400\ \mu\text{m}$. Since we require a laser system with high precision, we use the ns laser. Therefore, the cell is interconnected on a glass substrate being transparent for UV light metallized with $10\ \mu\text{m}$ Al. Due to the fact that the cells have a non-continuous base metallization, see Fig. 6.19, they cannot be measured before interconnection. Table 6.9 gives the I - V -data of a $50 \times 50\ \text{mm}^2$ -large cell measured by the module flasher before and after lamination without a shadow mask. The module reaches an effi-

¹⁶Here, the results of a single cell are shown to prove the contacting of small feature sizes. A module consisting of two point-contacted solar cells of another cell type contacted to an Al foil on an encapsulant substrate is presented in [165]. That cell features larger sizes of the BSF structures.

Table 6.9: I - V -parameters measured under standard testing conditions (100 mW/cm², 25 °C) of a point-contacted n -type BJBC solar cell laser welded to a glass substrate. Abbreviations used: Cell area A , efficiency η , fill factor FF, open-circuit voltage V_{oc} , and short-circuit current density J_{sc} .

	A [cm ²]	η [%]	FF [%]	V_{oc} [mV]	J_{sc} [mA/cm ²]
Module	25	20.6±0.8	78.1	668	40.6
Module laminated	25	20.4±0.8	74.8	668	41.0

ciency of 20.6% before lamination.

It is crucial to avoid any shunting during contacting 15000 or more structures as it is the case for a 156 × 156 mm²-large solar cell. Here, we have to contact roughly 1750 individual BSF contacts on the 50 × 50 mm²-large solar cells. Figure 6.20 a) shows an ILIT image of the contacted cell. An increased signal intensity is only observed at the laser-diced edges of the solar cell. This is caused by the increased recombination due to the laser-induced damage as well as due to the absence of passivation layers at the edges. However, in the center of the cell, no local shunt due to misalignment of laser weld spots or damage due to the process is observed.

It is also important to contact all BSF contacts in order to collect the generated current. The I - V -measurements show a current density of 40.6 mA/cm². This indicates that the generated current is efficiently collected by the multi-level metallization, especially taking into account that the laser-diced edges may reduce the current. Figure 6.20 b) and c) show the measured EL signal before and after lamination, respectively. We can resolve inhomogeneous regions with reduced EL intensity in the center of the cell and at the lower right side. These are caused by an imperfect contacting rather than by an increased non-radiative recombination path, since they are not visible in ILIT images. Reasons for these poorly contacted regions might be particles present on the sample prior to laser welding. This can lead to an increased gap between the cell and the metallized glass resulting in an imperfect welding and, hence, in locally increased contact resistance. This issue also explains the rather low fill factor of the module.

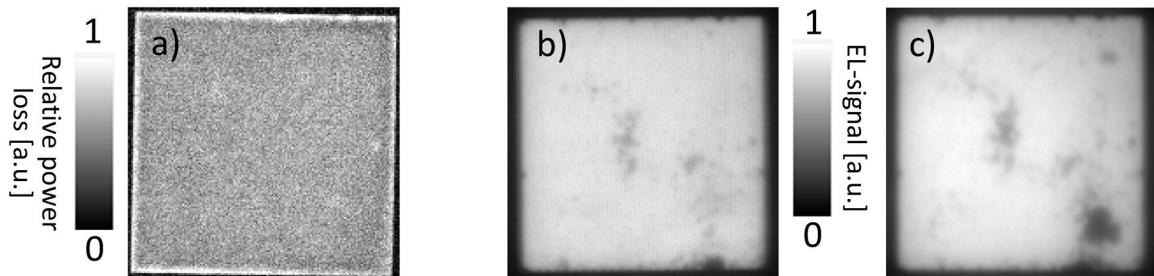


Figure 6.20: a) ILIT cosine image at an illumination intensity of 1 sun of the point-contacted BJBC solar cell after interconnection. b) and c) EL images of the connected point-contacted BJBC solar cell at an applied voltage of 0.7 V before and after lamination, respectively. The images are in linear scale.

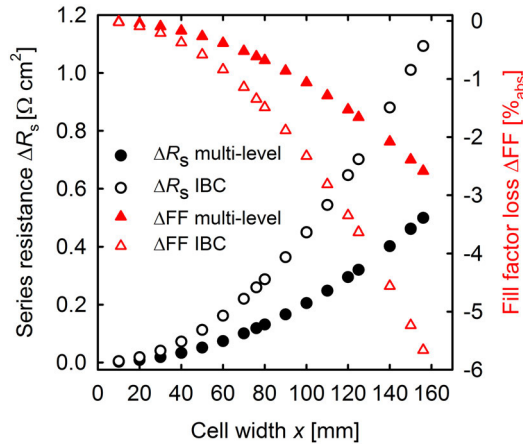


Figure 6.21: Series resistance contributions (circles, black) and fill factor losses (triangles, red) for a one-level IBC concept (open symbols) and the multi-level metallization (closed symbols) under the assumption of $10\ \mu\text{m}$ Al layers, $V_{oc} = 680\ \text{mV}$, $J_{sc} = 41\ \text{mA}/\text{cm}^2$, and $J_{mpp} = 38\ \text{mA}/\text{cm}^2$. Note that the contribution of the busbar metallization, which might be significant in the case of the one-layer concept, is not taken into account here.

6.4.2 Reduction of series resistance by the multi-level metallization

The multi-level metallization is one way to decouple the doping geometry from the metallization scheme. However, comparing it to an interdigitated back-contact (IBC) structure with equally wide fingers for both polarities, the deposited metal layer on the cell rear side carries only half of the current. The other half is transported in a second layer, which does not need to be evaporated to the rear side of the solar cells. Figure 6.21 shows a comparison between the presented two-layer metallization and the IBC structure using equations 6.2 and 6.3. We assume a metal coverage of 95% and an Al layer thickness on the solar cell of $10\ \mu\text{m}$ for both structures. The resistivity of the evaporated Al layer is $\rho = 3.2\ \mu\Omega\ \text{cm}$ [138]. In the case of the multi-level metallization, the thickness of the Al foil covering the whole rear side is also $10\ \mu\text{m}$ with a resistivity of $\rho = 2.7\ \mu\Omega\ \text{cm}$ [167]. Contact resistances, busbar effects in the case of standard IBC cells, and resistances of the interconnects between the cells are not taken into account.

In the case of a solar cell with $V_{oc} = 680\ \text{mV}$, $J_{sc} = 41\ \text{mA}/\text{cm}^2$, and $J_{mpp} = 38\ \text{mA}/\text{cm}^2$, the multi-level metallization reduces the calculated resistive losses by a factor of 2.2. In Fig. 6.21 the resultant absolute values for the change in resistance ΔR_s and in fill factor ΔFF are given as a function of the cell width x parallel to the current transport direction. For a full-area $156 \times 156\ \text{mm}^2$ solar cell, the calculated series resistance due to the finger metallization is $1092\ \text{m}\Omega\ \text{cm}^2$ for an IBC solar cell and $498\ \text{m}\Omega\ \text{cm}^2$ for the multi-level metallization. This leads to significant fill factor losses of 5.7% and 2.6% absolute. A reduction of the power loss can be achieved by increasing the metal thickness, which is not feasible in production regarding the process throughput and wafer bow. Alternatively, the width of the solar cells can be reduced. In the case of the multi-level metallization, halving the cells to a size $78 \times 156\ \text{mm}^2$ results in an acceptable series resistance of $125\ \text{m}\Omega\ \text{cm}^2$ corresponding to a fill factor loss ΔFF of only 0.65% absolute.

A layer thickness of $10\ \mu\text{m}$ evaporated Al is still challenging for industrial implementation and a reasonable thickness is supposed to be $2\ \mu\text{m}$. In chapter 4, we have shown that our

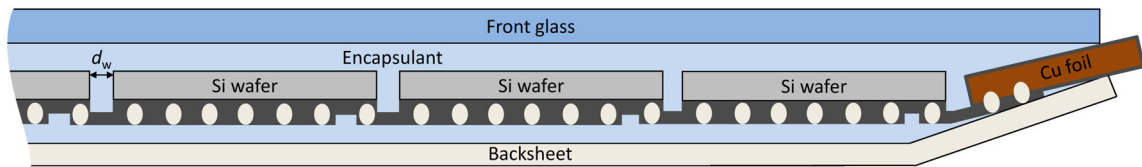


Figure 6.22: Schematic of the test modules used for determination of the mechanical reliability of the Al foil interconnects. One end of the string is fixed with respect to the front glass by laser welding the last Al foil piece to an Al-clad copper conductor, which is permanently pressed to the front glass by the lamination process. d_w is the gap width between two wafers.

laser welding process is able to contact such thin layers. Assuming $2\ \mu\text{m}$ Al evaporated on the solar cell and an Al foil with $10\ \mu\text{m}$ thickness in the case of $39\ \text{mm}$ cell width (a quarter of $156\ \text{mm}$), the series resistance in the metallization is $99\ \text{m}\Omega\ \text{cm}^2$ resulting in a reduction of the fill factor of 0.52% absolute.

6.4.3 Mechanical aspects in dependence on solar cell size

Apart from the electrical resistance, it is also important to take into account the mechanical stress induced due to the different thermal expansion coefficients of the various materials within the module under thermal cycling. They result in a change of the gap width between two solar cells when the temperature changes [155]. This may lead to fatigue and damage of the Al foil between the cells, which has to follow the movement of the solar cells. Therefore, we fabricate different dummy strings of five 156-mm -wide wafers, ten 78-mm -wide wafers, 15 52-mm -wide wafers, and 20 39-mm -wide wafers. The laser pattern and process is the same as used for interconnection of point-contacted solar cells. One side of the string is fixed to the module glass (see Fig. 6.22) in order to obtain effects similar to full sized strings, i.e., ten solar cells in the case of the 156-mm -wide wafers. The wafers are metallized with $10\ \mu\text{m}$ Al.

Due to variations in the positioning of the wafers, the gap width d_w changes between 0.6 and $2\ \text{mm}$. After 200 thermal cycles (temperature change between $-40\ ^\circ\text{C}$ and $+85\ ^\circ\text{C}$), the Al foil between the wafers does not show any damage, except when using 156-mm -wide wafers and a gap between them of $0.6\ \text{mm}$. Large gap sizes in the case of the 156-mm -wide wafers are not damaged, because the same displacement acts on a wider foil strip. This results in reduced strain within the foil and a lower damage risk. Therefore, when using an appropriate distance between the solar cells, e.g. $1\ \text{mm}$, the thermo-mechanical stress under thermal cycles will not be critical according to these experiments. However, final devices need to be tested because a change in the laser welding pattern, the Al foil, or other parameters may affect the mechanical properties within the module [168].

6.5 Chapter summary and discussion

The development of the AMELI process focuses on the common goal in photovoltaics research to contribute to a more economical electrical power generation from solar irradiation. This requires, as described in the introduction chapter 1, minimizing the production costs, ensuring a longterm functionality, and maximizing the energy conversion efficiency. In this

chapter, we discuss how the laser welding process improves all three of them with the focus on techniques to increase module performance.

Cost reduction by decreasing the material consumption

For standard PV modules, the material costs contribute more than 60% of the total module costs [30]. Among these, the silicon wafers and the metal pastes are the most and second-most expensive materials, respectively. The costs for the silicon wafers can be significantly decreased by reducing the wafer thickness [29, 30, 169]. However, this has the risk of increasing the yield loss, especially during cell interconnection [21, 26]. The cell breakage is caused by mechanical stress induced during soldering and the subsequent lamination process. During soldering the entire cell and a thick interconnect are heated through. In contrast to this, during laser welding the thin Al foil and the cell metallization are only locally heated by the short laser pulses. This reduces the thermomechanical stress. Additionally, we interconnect the cells on their total width using a thin Al foil ($\approx 10 \mu\text{m}$). Thereby, we avoid the stress induced by the commonly used thick Cu interconnects ($\approx 150 - 200 \mu\text{m}$) that are pressed on a few points to the cell rear side during lamination [24, 170]. As an example, we show in this work that the AMELI process is able to contact thin ($< 100 \mu\text{m}$) large-area solar cells, which has the potential for significant cost reduction. In another work we presented the successful contacting of 34- μm -thick solar cells based on macroporous Si by the AMELI process [152].

The high costs of the screen-printed metallization are mainly caused by the silver content of the pastes. The laser welding process is able to contact aluminum without the need of an oxide-free metal surface, which is typically a fluxed silver layer. The material costs of the metallization can be reduced by replacing silver with aluminum. Depending on the cell geometry, the thickness of the Al layer can be decreased from $10 \mu\text{m}$ to $2 \mu\text{m}$, which additionally lowers the material cost. Furthermore, we replace the solder-coated Cu interconnects with Al foil, which is a widely-used material. It requires less production steps and less cost-intensive materials than the solder-coated Cu ribbons. Therefore, the AMELI process contributes to a significant reduction of usage of the most expensive materials within a PV module.

Longterm stability proven by accelerated aging test

The longterm reliability is highly dependent on the involved material components and the history of the module [57]. However, standard modules based on bifacially contacted solar cells with failures, which are returned out of the field to the installer, show issues related to the interconnection in 66% of all cases [58]. A failure in interconnection causes higher series resistances and, thus, a decrease in fill factor. The modules interconnected by laser welding do not show any degradation ($\Delta P < 1\%$) after the required 200 humidity-freeze cycles¹⁷, when a lamination foil as substrate and thermal evaporation of Al for cell metallization are employed. Commercial modules with BJBC solar cells by the company SunPower are well known for their reliability [58]. After 200 humidity-freeze cycles, they show a degradation of only 3% in power relative to the initial values [171], which is in the order of the degradation

¹⁷We use humidity-freeze cycles with a reduced humidity time of 6 instead of 20 hours, see section 3.4.7.

we observe for our laser-welded module. Typically, a significant degradation is observed even after 200 thermal cycles, where only the temperature is varied and the impact of the humidity is omitted [57, 75, 172, 173]. Recently, the company Trina presented its new BJBC concept, which shows a reduction of the output power of 4.3% after 20 humidity-freeze cycles [73]. According to TÜV Rheinland, between 2007 and 2009, 14% of the tested crystalline silicon modules lost more than 5% output power after 10 humidity-freeze cycles [174]. We show that the fill factor is unaffected after 1402 humidity-freeze cycles when using the AMELI process to interconnect the solar cells. This proves that our interconnection by laser welding is highly stable under artificial aging. Testing this amount of humidity-freeze cycles took us about three and a half years. The highest number of humidity-freeze cycles a terrestrial PV module was tested, which we find to the best of our knowledge in literature, are 300 cycles by SunPower [171].

Increase in conversion efficiency by an enhanced module design

We investigate in detail the effect of the laser welding process on the cell and module performance. As shown in chapter 4, we determine suitable laser parameters for a damage-free welding of solar cells. This is also proven in application, since we observe no change in open-circuit voltages for all modules, indicating that the interface between the metallization and the passivated silicon surface is unaffected. However, we observe changes in the short-circuit current density, mainly after lamination due to the reflection at the glass-air interface. This can be significantly reduced by the application of an anti-reflection coating on the glass front side. In the wavelength range between 400 and 1100 nm, we determine a reduction of the reflectivity from $3.7 \pm 0.5\%$ to $1.9 \pm 0.5\%$ absolute due to the ARC. Additional losses by absorption in the lamination foil can be reduced by using an encapsulant that is transparent for ultra-violet light [175–177].

Compared to the initial cells, we observe no variation in short-circuit current density in the case of the busbar-free solar cells after interconnection. However, the expected gain in J_{sc} due to the absence of electrical shading caused by the base busbars is not observed. The relative losses compared to the designated area measurements of 3.0% to 3.3% are caused by the additional marking of the cells, edge effects, and current mismatch of the individual cells. The effect due to the cell marking, which reduces the short-circuit current density by $0.2 \pm 0.2\%$, can be eliminated by marking the cells before their passivation. The outer edges, which are also present before laser dicing, cause $0.4 \pm 0.2\%$ relative current reduction and the laser-diced and passivated edges reduce the current by $1.1 \pm 0.2\%$. Recalling that the laser-diced edges are five times longer, their effect per length is not larger than the one of the non-diced edges, which are the outer edges of the wafer during processing. Therefore, the laser dicing of the solar cells can be regarded as a suitable process for our BJBC solar cells. The smaller cell size after laser dicing has the potential to harvest more sunlight per active cell area, since the modules benefit more from multiple reflections between backsheet and front glass [150, 151, 178].

The largest effect however is caused by the cell mismatch reducing the module current for the presented module by up to 3%. This effect could be eliminated by measuring the busbar-free solar cells before interconnection and matching them by their current. However, there is still a lack of I - V -testers that are able to contact each individual finger, although research groups work on such cell types [6, 52].



Figure 6.23: Interconnect as used for laser soldering of $125 \times 125 \text{ mm}^2$ BJBC solar cells.

We achieve a significant enhancement of the cell performance due to the increase in the fill factor. In the case of the busbar-free solar cells, the fill factor increases relatively by 3.7% to 5.2% (2.9% to 4.0% absolute). Typically, the fill factor decreases during module integration of solar cells depending on the interconnection technology. It decreases by about 3 to 7% absolute in case of standard bifacially contacted solar cells [150, 151]. Even for advanced module concepts like for MWT solar cells, it is reduced by about 1 to 4% absolute [74, 75, 179]. Sunpower BJBC solar cells show a change in fill factor between the cells and their record module of 1 to 2% absolute [8].

We mainly influence the fill factor by reducing the series resistance R_s . There are three main contributions to the series resistance [157]:

1. The bulk resistance of the silicon.
2. The resistances within the metallization and interconnects.
3. The contact resistances between the silicon and the cell metallization as well as between the cell metallization and the interconnects.

Aspect 3 has only marginal impact in the case of our modules. The largest contribution to the total series resistance is the contact resistance between the silicon and the aluminum with $R_s \approx 72 \text{ m}\Omega \text{ cm}^2$. The series resistance between the cell metallization and the Al foil is below $8.7 \mu\Omega \text{ cm}^2$. For the point-contacted solar cells as well as the busbar-free solar cells, the emitter region is contacted only at one edge. Therefore, it limits contact resistance between the two metal layers. In the case of the busbar-free solar cells, the contact area to the emitter metallization is only about 0.5% of the cell area. However, the contribution to the series resistance due to this contact is only in the range of a few $\text{m}\Omega \text{ cm}^2$ and still one order of magnitude lower than the contribution of the Si-Al contact. The same also applies to the other contributions of the module interconnection (included in aspect 2), e.g., resistive losses within the Al-clad copper conductor and the Al foil next to the cells.

In the case of the interconnection between two full-sized BJBC solar cells using on-laminate laser soldering [55, 70], solder-coated copper interconnects are used, see Fig. 6.23. The contribution of the interconnection to the area-weighted series resistance¹⁸ is $R_s = 36 \text{ m}\Omega \text{ cm}^2$. This results in a reduction of the fill factor $\Delta\text{FF} = 0.2\%$ absolute. For the interconnection of busbar-free BJBC solar cells, the resistance between two cells, which is caused by the contact resistance between the two metal layers and the resistance of Al foil between two cells, is $R_s = 3 \text{ m}\Omega \text{ cm}^2$. This results in a change in fill factor of $\Delta\text{FF} = 0.014\%$ absolute, which is an order of magnitude lower than for the soldering process in the case of full sized cells.

¹⁸The series resistance between two soldering lugs of the interconnect is $0.5 \text{ m}\Omega$ as measured by 4-point probes method. The area of the lugs is about 10 mm^2 and the contact resistance of the solder joints is about $0.01 \text{ m}\Omega \text{ cm}^2$ [55], i.e., the total contact resistance is $0.1 \text{ m}\Omega$ per polarity. Therefore, the interconnection between two neighboring cells causes a resistance of $0.7 \text{ m}\Omega$ per pad, i.e., in the case of three solder pads per busbar, it results in a series resistance contribution related to the cell area of $R_s = 36 \text{ m}\Omega \text{ cm}^2$.

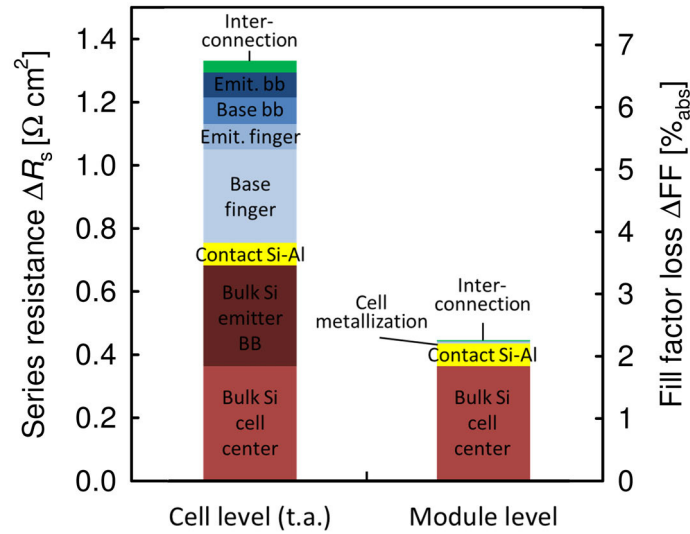


Figure 6.24: Series resistance of the BJBC solar cell on total area and of the busbar-free BJBC solar cells interconnected in the module. We calculate the contributions of the metallization analytically, the contact resistance and the bulk resistance are numerically simulated using 2D device simulations, and the influence of the emitter busbar is deduced by comparing the total with the designated area I - V -measurements. Additionally, the series resistances between two neighboring solar cells caused by the interconnection are given. Emit. stands for emitter and bb for busbar.

The series resistance within the metallization (aspect 2) is reduced by various factors. In the case of the multi-level metallization, it is reduced by increasing the area fraction of each polarity on the cell rear side. Comparing the multi-level metallization with an IBC solar cell, which has equally wide fingers for base and emitter, the series resistance decreases by a factor of two. Compared to IBC cells, as we used for example for the modules with two busbars having non-symmetrically finger widths, see section 6.1, this factor is even three. We further reduce the series resistance of the metallization by omitting the busbars and by using shorter finger lengths. In the case of the busbar-free solar cells, this decreases the contribution of the metallization from $R_s = 533 \text{ m}\Omega \text{ cm}^2$ for the initial cells to $8 \text{ m}\Omega \text{ cm}^2$ in the case of the interconnected cell strips. Additionally, eliminating the emitter busbar with the large solder pads reduces the series resistance within the silicon by $320 \text{ m}\Omega \text{ cm}^2$ as determined by comparing the designated area with the total area measurement.

Figure 6.24 summarizes the series resistance contribution of the initial cell on total area and the cell as it is interconnected in the module. The depicted Si bulk resistance (aspect 1) includes the Si base material, the emitter, and the BSF region. These and the contact resistance between the silicon and aluminum are extracted from the 2D device simulations of a unit cell including half a BSF and half an emitter finger. The $1.3 \Omega \text{ cm}^2$ of the BJBC solar cells calculated from the sum of the individual contributions to the solar cell's series resistance (without interconnection) is in good agreement with the measured values between $R_s = 1.1 \Omega \text{ cm}^2$ and $1.6 \Omega \text{ cm}^2$ of the solar cells used for the four modules investigated in this work. The series resistance values of the cells on module level are in agreement with the experimental results, too. A resistance of $R_s = 441 \text{ m}\Omega \text{ cm}^2$ results in a decrease of the fill factor of $\Delta \text{FF} = 2.2\%$ absolute. This agrees well with the measured difference between the pseudo fill factor of the cell on designated area and the measured module fill factor ($\Delta \text{FF} = \text{pFF} - \text{FF} = 2.2\%$ absolute).

The total series resistance of the cell (t.a.) is reduced by a factor of three compared to the busbar-free solar cells on module level. In the case of the cell on module level, the contributions by the metallization are marginal and additional contributions by the interconnection are in the same order. However, the cell is limited by the resistance within the silicon. This can be significantly reduced by using a smaller index [5, 159, 163, 180, 181], which also requires contacting of finer structures. As we prove successfully for the point-contacted solar cells, it is possible to contact structures in the order of 100 μm by laser welding. Therefore, the laser welding offers the possibility to reduce all major contributions of the series resistance while simultaneously minimizing current losses due to electrical shading.

In summary, the application of the AMELI process addresses all three factors for a more economical electrical power generation from solar irradiation. It has the potential to reduce the material costs, enables a longterm functionality of the PV modules, and results in an increase in the efficiency of the solar cells and, thus, of the modules.

7 Summary and Outlook

In this work a novel interconnection process based on laser welding is developed as an alternative to soldering or conductive adhesives. The AMELI process interconnects solar cells with Al metallization using a thin Al layer. We analyze this laser welding process with respect to its mechanical properties as well as to the laser-induced damage at the interface between the Al metallization and the passivated silicon surface. For the investigated laser sources with pulse durations of 20 ns and 1.3 μs , we find process windows that ensure a sufficiently strong mechanical contact without inducing detectable laser damage. In the case of the ns laser and a thermally deposited Al layer on a glass substrate with a thickness of 10 μm , the metallization thickness on the silicon wafer can be reduced down to 1 μm . For the same substrate and the μs laser, the limiting thickness is 2 μm . Alternatively to the glass substrate, an encapsulant layer, to which an Al foil is thermally attached, can be used. Further, we determine the contact resistance of the laser-welded area to be below 10 $\mu\Omega\text{ cm}^2$ for tested samples.

The welding process is driven by the melting dynamics within the irradiated Al layer in the case of the μs lasers. The heat transport to the interface between the two Al layers can be described by thermal diffusion in the case of thin layers. For thicker layers ($d_{\text{su}} > 7 \mu\text{m}$), however, the process is governed by the breaking of the Al layer due to the thermal expansion of the underlying material and subsequent ejection of molten aluminum. Evaporation of the irradiated aluminum does not dominate the laser welding process.

In order to prove the applicability of the process, we employ it to interconnect BJBC solar cells. We start with cell strips that we can characterize before interconnection using our *I-V*-tester, i.e., cells featuring two busbars. Using the two laser systems no significant decrease of the cell voltage, fill factor, current and, subsequently, its performance is observed after contacting. Module efficiencies of 20% are reached. As shown during accelerated aging tests, modules consisting of cells metallized with thermally evaporated Al and a flexible substrate show no detectable degradation of the fill factor even after 1402 humidity-freeze cycles. This shows that the laser-welded interconnection of BJBC solar cells is highly stable under artificial aging.

Since the laser weld spots are about 50 μm in size, they are able to contact smaller feature sizes compared to the commonly used solder pads, which are in the order of a few square millimeters [25, 70]. This offers the possibility to contact for example the individual emitter fingers and, thus, to avoid the fill factor loss related to the emitter busbar. The reproducibility of the process is experimentally demonstrated by contacting twelve solar cell strips with a total of 720 emitter fingers. The process also enables us to interconnect solar cells free of busbars by directly contacting the individual fingers of both polarities. We are therefore able to omit both busbars. Such modules with busbar-free solar cells show an increase in efficiency of the module by 4 to 5% relative to the initial cell performance. This results in module efficiencies of 21.4%. The gain is mainly achieved by increasing the fill factor due to the absence of the busbars, shorter current paths, and the support of the

conducting layer of the narrow base fingers. The largest remaining contribution to the series resistance originates from the internal resistance of the cell structure calling for improved cell designs. Point-contacted BJBC solar cells with small feature sizes allow to reduce the series resistance and the current losses by electrical shading simultaneously. We successfully contact such a cell using a multi-level metallization with a lean process sequence that is developed within this work. We thereby open new possibilities for interconnecting improved cell structures and simplifying the back end process of BJBC solar cells. In total the AMELI process contributes to the reduction of material consumption with simultaneous efficiency improvement and proves its longterm stability. Therefore, it appears attractive to transfer the AMELI process from the laboratory to production.

The next step towards an industrial application of the AMELI process is to investigate the major challenges for up-scaling. Topics like the dielectric properties of the insulation layer at elevated voltages as they occur in solar power plants need to be analyzed in order to determine its required thickness. Further, the tolerance of the gap between the cell metallization and the interconnecting Al layer, as well as the limits of the surface roughness, need to be investigated. These are critical parameters for the interconnection and stringing process during which it is required to press the cell to the Al layer. For each geometry of the weld spots, type of Al foil, and encapsulant, the reliability of the interconnecting Al foil with respect to the mechanical properties needs to be investigated.

Throughout this work, we focus on the interconnection of BJBC solar cells metallized with evaporated Al. However, bifacially contacted solar cells currently dominate the PV market and back-contacted solar cells have only a limited share [3]. The bifacially contacted solar cells fabricated on *p*-type Si are typically metallized on the front side by screen-printed silver and on the rear side by screen-printed aluminum with inlaid silver pads. Omitting these silver pads has the potential of reducing the total Ag consumption by about one fourth [182] and to improve the efficiency by reducing recombination. An increased recombination occurs underneath the Ag pads since no aluminum BSF is formed there [183, 184]. Avoiding Ag pads has shown an efficiency advantage of 0.1 to 0.4% absolute [185]. This can be achieved by application of solderable contacts using tin [185] or tin alloys [186] by ultra-sonic soldering to the Al paste. As an alternative, we presented in another work [187] that laser welding an Al foil to the screen-printed Al rear side is also suitable for interconnection of these cells. The tab on the front side can be soldered to the silver grid. That, however, may result in high mechanical stress in the solar cell [74, 75]. This can be reduced by using conductive adhesives on the front side [74, 79]. The laser welding of screen-printed metallization is also highly interesting for contacting back contacted solar cells like metal wrap through solar cells [71, 188–190].

Although screen printing has already been used for several decades [191], it leads to a significant reduction of the open-circuit voltage in the case of bifacially contacted PERT solar cells on *n*-type Si [192, 193]. This can be avoided by using evaporated or sputtered Al for contacting the rear-side emitter of such solar cells [192, 194]. Record PERT cell efficiencies of up to 22.5% on 6" CZ-wafer are achieved with this metallization scheme [195, 196]. However, the Al metallization cannot be soldered without applying a stack of different metal layers before soldering [60]. As shown in this work, the laser welding process eliminates the need for additional layers and is able to directly contact the evaporated Al layer.

Therefore, screen-printed MWT solar cells or PERT solar cells with evaporated Al metallization are highly suitable cell technologies for the intermediate-term application of the AMELI process. For future PV markets, BJBC solar cells with small-sized finger struc-

tures offer the largest potential for our laser welding process. Such solar cells benefit most from contacting with high spatial resolution by the AMELI process due to the increase in efficiency and the potential in cost reduction.

A Appendix

A.1 Comparison of conductivities and prices for Al, Ag, and Cu

Table A.1: Price range between 1.1.2014 and 31.12.2014 and electrical resistivity for aluminum, silver, and copper. A small product of the resistivity and price is favored. We use the (maximum + minimum)/2 of the price for this product. The prices are taken from [197] and the resistivity at room temperature from [198].

Metal	Maximal	Minimum	Resistivity	Product price \times resistivity
	€/kg	€/kg	$\times 10^{-6} \Omega \text{ cm}$	$\times 10^{-6} \Omega \text{ cm} \text{ €/kg}$
Aluminum	1.68	1.21	2.82	4.09
Silver	515	396	1.63	742
Copper	5.48	4.65	1.72	8.71

A.2 Additional experimental details to section 3.3.2

For detecting laser-induced damage, we use lifetime samples, i.e., well passivated Si wafers. In order to be sensitive to surface damage, wafers with high minority charge carrier lifetimes are required. Float-zone silicon (FZ-Si) wafers, which have a low concentrations of impurities, are suitable for this. However, these are cost-intensive wafers. Alternatively, *n*-type, e.g., phosphorous doped, Czochralski-grown (Cz-Si) wafer can be used. The charge carrier lifetime of P-doped wafers have shown to be less prone to impurities [199, 200].

For first experiments with the ns laser, 270 μm -thick $125 \times 125\text{mm}^2$ boron-doped *p*-type float-zone silicon (FZ-Si) wafers with a resistivity of $240 \Omega \text{ cm}$ are employed. Later we use 160- μm -thick $125 \times 125\text{mm}^2$ phosphorous doped *n*-type wafers with a resistivity of $4 \Omega \text{ cm}$ for the experiments the μs laser 2 .

The mechanical experiments are performed on Cz-Si wafers. Their thickness is about 170 μm after damage removal. Through out this work, different wafers have been used. In additional tests, we could not detect any significant influence of the wafer material, its doping or passivation layers underneath the Al metallization.

A.3 Comparison of interconnect resistances

Compared to standard cell interconnects for bifacially contacted solar cells, a 10- μm -thick Al layer leads to a similar series resistance related to the distance between the solar cells. In the case of 6" solar cells, three interconnector ribbons each with a cross-section of $1.5 \times 0.2 \text{ mm}^2$ of copper ($\rho = 1.67 \mu\Omega\text{cm}$ [201]) are used. The resistance between two cells per length of such interconnects is $186 \mu\Omega/\text{cm}$. Using 10 μm Al ($\rho = 2.65 \mu\Omega\text{cm}$ [201]) on a length of 156 mm leads to a similar resistance of $170 \mu\Omega/\text{cm}$. The same applies for 5" bifacially contacted solar cells, where the interconnector ribbons (two with a cross-section of $2.5 \times 0.15 \text{ mm}^2$) lead to a resistance of $223 \mu\Omega/\text{cm}$ and the 10- μm -thick Al layer on the whole width results in $212 \mu\Omega/\text{cm}$.



Figure A.1: Interconnect as used for laser soldering of $125 \times 125 \text{ mm}^2$ BJBC solar cells.

5" BJBC solar cells are interconnected by interconnects with varying width and strain reliefs, see Fig. A.1. They are soldered to the busbar of the cell at three points. Between these contact points of two neighboring cells, we measure a series resistance of $500 \mu\Omega$ by 4-point probe method for such cell interconnects. Assuming 10- μm -thick Al layer on a width of 42 mm ($\approx 125\text{mm}/3$) and a distance between the contact of 4 mm (2 mm cell spacing and 1 mm tolerance to each cell edge) results in a resistance of $254 \mu\Omega$.

A.4 Qualitative correlations between the mechanical and electrical properties of the weld spots

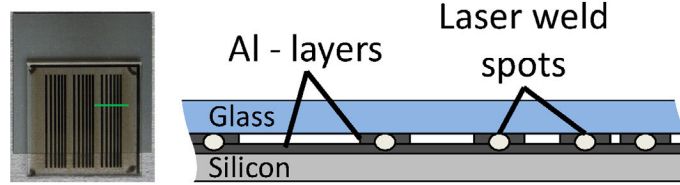


Figure A.2: Photograph and a schematic cross-section of the test sample used for an estimation of the qualitative dependence of the contact resistivity. The green line in the photograph indicates the location of the cross-section.

Additionally, to the quantitative measurements of the contact resistance for the ns laser, see section 4.1.2, we use a simplified test to evaluate correlations between the mechanical and electrical properties of the weld spots qualitatively. This simplified test does not correct the series resistances due to the Al layers and has no well defined contact area. However, it qualitatively shows the influence of the laser parameters. Figure A.2 shows a photograph and a schematic cross-section of the test sample. The sample structure is similar to that of the transmission line method [202, 203].

Figure A.3 a) shows the dependence of the resistance on the laser parameters and b) the mechanical properties. Most parameters that do not lead to a mechanical contact could also not be measured electrically. However, for example 4 pulses with $53 \mu\text{J}$ lead to no detectable mechanical contact and the series resistance is several order of magnitudes higher than for the parameters that lead to a mechanical contact. Even samples that do not show detectable contacts could also have a relatively low series resistance, e.g., single pulses with $112 \mu\text{J}$. Nevertheless, the experiments show that if there is a mechanical contact, the electrical

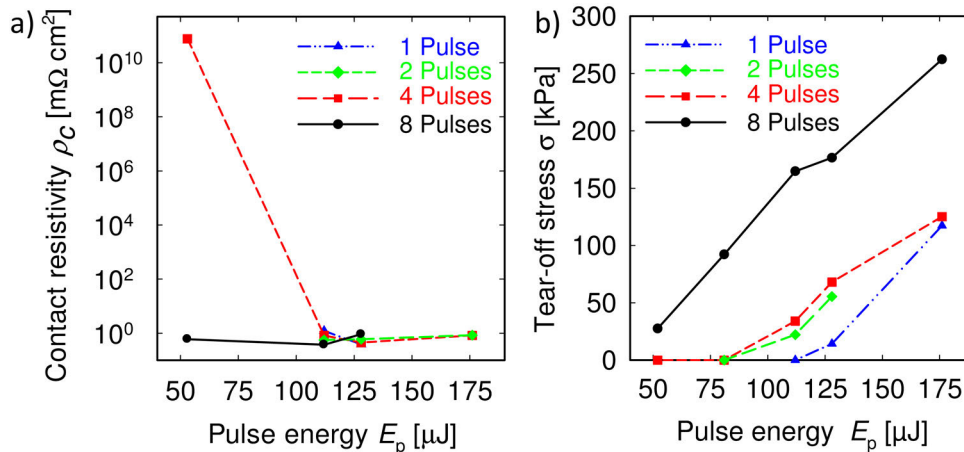


Figure A.3: a) Rough estimation of the qualitative dependence of the contact resistivity ρ_c in dependence of the laser parameters. The aluminum thicknesses are $d_{\text{Si}} = 20 \mu\text{m}$ and $d_{\text{Si}} = 10 \mu\text{m}$. b) The corresponding perpendicular tear-off stresses σ . The laser system was maintained and modified within the time of this work, including changes of the laser source as well as of the beam line. This might result in changes of the beam profile. Since different experiments are done at different times, the fluences might not coincide and, therefore, here only the pulse energy E_p is given.

contact resistivity is low. The quantitative values of the contact resistance are shown in section 4.1. We perform these experiments only once, therefore, they lack of statistics. They are repeated later with an improved design, see section 4.1.

A.5 Input parameters for the FEM simulations using COMSOL in section 5.2

We use Comsol 4.3 [145] with the heat transfer module for the FEM simulation of the thermal distribution within the glass substrate, the Al layers, and the silicon wafer. For meshing we use a quadratic free quad mesh. We implement the enthalpy of melting H_m and evaporation H_v with a triangular function ¹ that we add to the heat capacity. The phase transition between solid and liquid is stretched in the case of aluminum over a temperature range which is between 1 and 10 K. The width is set to small values when investigating the onset of melting and to larger values for example for verifying the presence of evaporation. The enthalpy of evaporation is spread over a temperature range of 40 K.

Table A.2: Input parameters for the FEM simulations using COMSOL.

Name	Symbol	Value	Source
Laser pulse energy	E_p	2 mJ	Experimentally determined
Transmission of beam line including scanner system		0.88	Experimentally determined
Pulse duration of laser		1.286 μ s	Measured by laser manufacturer
Room temperature	T_r	293.15 K	
Fraction of absorbed laser light	A	Fig. A.4 b)	
Al melting temperature	T_m	933.5 K	[144]
Al evaporation temperature	T_v	2730 K	[87]
Al melting enthalpy	H_m	397 J/g	[144]
Al evaporation enthalpy	H_v	10750 J/g	[87]
Al heat capacity	C	Fig.A.4 a)	
Al thermal conductivity	k	Fig. A.4 a)	
Al density	ρ	2700 kg/m ³	[87]
Glass heat capacity	C	Fig. A.5 a)	
Glass thermal conductivity	k	Fi. A.5 a)	
Glass density	ρ	2200 kg/m ³	[113]
Si heat capacity	C	Fig. A.5 b)	
Si thermal conductivity	k	Fig. A.5 b)	
Si density	ρ	2329 kg/m ³	[145]

¹Only in case to determine the internal energy (Fig. 5.9 b)), we use a Gaussian shaped profile, since high changes in material parameters lead to oscillations in U

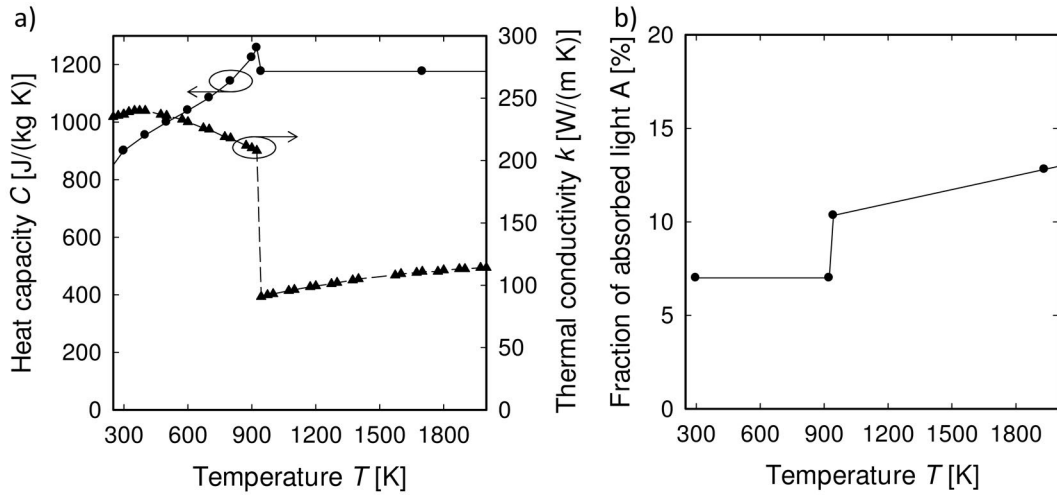


Figure A.4: a) Heat capacity C of aluminum taken from Hatch [144] ($T < 933.5$ K) and McDonald ($T > 933.5$ K) and the thermal conductivity k also taken from Hatch [144]. b) Absorbed fraction of energy A , i.e., the emissivity, of the Al layer for $T < 933.5$ K experimentally determined, see Fig. 4.16, and varied in the simulations between 7 and 8%, for $T > 933.5$ K taken from Hüttner [142].

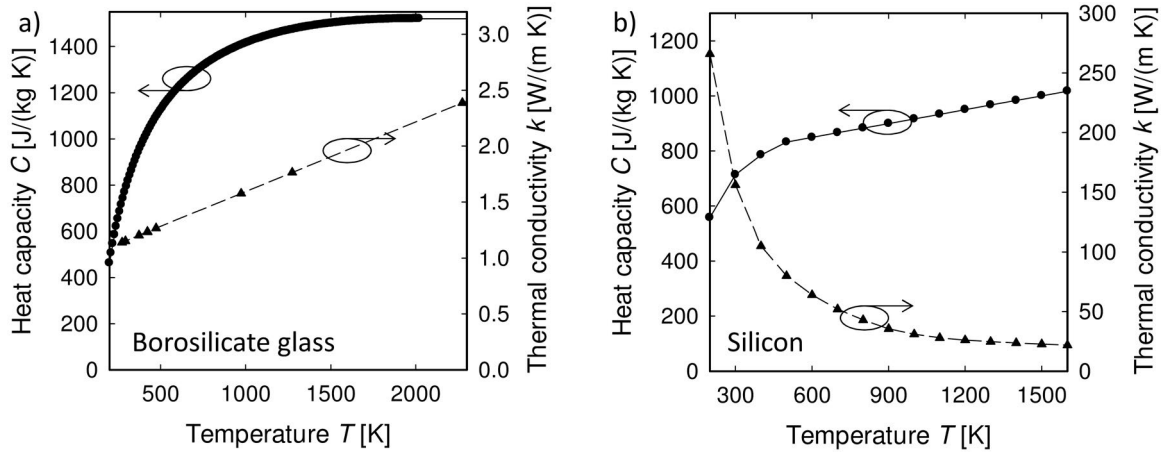


Figure A.5: a) Heat capacity C of borosilicate glass calculated according to Richet [204] using its composition [113] and its thermal conductivity k using the parametrization of Mann [205]. b) Heat capacity C of silicon taken from Hull [206] and its thermal conductivity k taken from Glassbrenner and Slack [207].

A.6 Oscillating temperature effect due to the thermal barrier in the FEM simulations

In section 5.4, we investigate the properties of the interface between the two Al layers. In order to imitate the gap that hinders the thermal conductivity between the two layers, we insert a thermal barrier. Its conductivity is given in Fig.A.6 a). The width of the transition a between 0 and the conductivity of liquid Al has an impact on the distribution of the temperature within the Al layers. Figure A.6 b) shows the temperature above and below the barrier for $a = 50$ K and 400 K in dependence on the distance from the center of the laser spot, i.e., the radius r . In the case of the narrow transition, the temperature shows oscillations. These are caused by the onset of conductivity at one point leading to a cooling of the neighboring regions where the conductivity of the barrier is again 0 W/(m K). We investigate impact of the cooling by changing the thermal conductivity only in the radial direction within the Al and keep it constant in the vertical direction. For higher conductivities, the distance between the two maxima increased due to the change in the cooling effect, which supports our hypothesis.

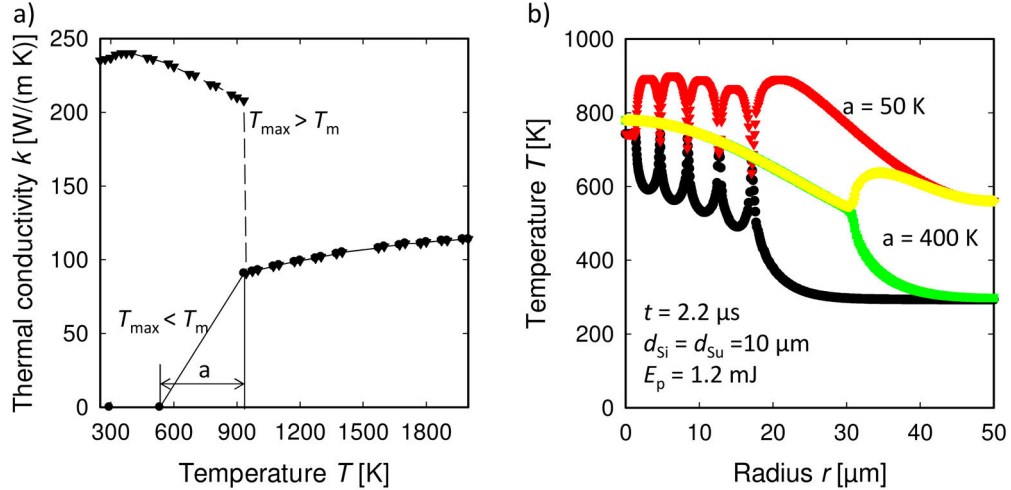


Figure A.6: a) Thermal conductivity k of the thermal barrier layer as used in section 5.4. From room temperature up to a temperature a below the melting temperature T_m the conductivity is 0 W/(m K) and then increases linearly to the thermal conductivity of molten Al. Once T_m is reached the thermal conductivity is equal to the one of Al and follows the upper branch. If T_m is not reached, the conductivity in dependence on temperature follows the lower branch. b) Temperature above and below the thermal barrier for different onset of the thermal conductivity. In the case of $a = 400$ K, the boundary starts conduction at 533.5 K and for $a = 50$ K it starts at 883.5 K.

A.7 Input parameters for numerical device simulations using SENTAURUS DEVICE in section 6.3.1

Table A.3: Input parameters for numerical device simulations using SENTAURUS DEVICE. We use a unit cell consisting of half a BSF finger and half an emitter finger. Abbreviations used: photo conductance decay PCD and electrochemical capacitance-voltage ECV.

Name	Symbol	Value	Source
Period of the finger structure	p_f	2300 μm	input laser processing
Width base finger	w_{bf}	500 μm	input laser processing
Width emitter finger	w_{ef}	1800 μm	input laser processing
Cell thickness	d	165 μm	dial gauge
Phosphorous concentration base	N_D	$2.4 \times 10^{15} \text{cm}^{-3}$	wafer resistivity determined by 4-point probes method
Phosphorous doping profile BSF	$N_D(x)$	import profile	ECV profiler measurements
Boron doping profile emitter	$N_A(x)$	import profile	ECV profiler measurements
Charge carrier lifetime Si bulk	τ	2.4 ms	PCD measurements
Front surface recombination velocity	S_f	30 cm/s	[159]
Emitter region surface recombination velocity	S_e	16 cm/s	see 1.
BSF region surface recombination velocity	S_b	1×10^5 cm/s	see 2.
Metallized surface recombination velocity	S_{met}	2×10^6 cm/s	default of SENTAURUS
Contact opening emitter region	A_{ec}	1.3%	optical microscope
Contact opening BSF region	A_{bc}	2.4%	optical microscope
Contact resistance between Si and Al	R_c	0.27 $\text{m}\Omega \text{cm}^2$	see 3.

1. The surface recombination velocity of the emitter S_e is determined using a parametrization technique from Altermatt et al. [208] and is based on experimental data from [209]. The resulting saturation current density of $J_0 = 25 \text{ fA/cm}^2$ matches well with the experimental data of $J_0 = 24 \text{ fA/cm}^2$ determined by photo conductance decay.
2. We choose the surface recombination velocity of the BSF S_b in order to obtain the saturation current density of $J_0 = 260$ to 300 fA/cm^2 , which is in accordance with the measured values by PCD of 364 fA/cm^2 taking into account the overestimation of this method [210].
3. We determine the contact resistance R_c for the emitter region by the parametrization of Mader et al. [211] and the determined boron surface concentration using ECV measurements. The same contact resistivity is also used for the back surface field, which is for the determined phosphorous surface concentration in accordance with the measurements by Yu [212]. However, literature values between 1×10^{-6} [213] to $1 \times 10^{-3} \Omega \text{cm}^2$ [159] are stated as input parameters for simulations of BSF regions with similar sheet resistances.

Bibliography

- [1] B. Sahan, “Wechselrichtersysteme mit Stromzwischenkreis zur Netzanbindung von Photovoltaik-Generatoren,” Ph.D. dissertation, Kassel. [Online]. Available: <http://d-nb.info/1016850891/34>
- [2] C. R. Osterwald and T. J. McMahon, “History of accelerated and qualification testing of terrestrial photovoltaic modules: A literature review,” *Progress in Photovoltaics: Research and Applications*, vol. 17, no. 1, pp. 11–33, 2009.
- [3] SEMI Europe, “International technology roadmap for photovoltaic (ITRPV) 2013 results,” 2014. [Online]. Available: itrpv.net/.cm4all/iproc.php/Reports%20downloads/ITRPV_2014_Roadmap_140314_web.z.pdf?cdp=a
- [4] K. Masuko, M. Shigematsu, T. Hashiguchi, D. Fujishima, M. Kai, N. Yoshimura, T. Yamaguchi, Y. Ichihashi, T. Mishima, N. Matsubara, T. Yamanishi, T. Takahama, M. Taguchi, E. Maruyama, and S. Okamoto, “Achievement of more than 25% conversion efficiency with crystalline silicon heterojunction solar cell,” *IEEE Journal of Photovoltaics*, vol. 4, no. 6, pp. 1433–1435, 2014.
- [5] D. D. Smith, P. Cousins, S. Westerberg, R. D. Jesus-Tabajonda, G. Aniero, and Y.-C. Shen, “Toward the practical limits of silicon solar cells,” *IEEE Journal of Photovoltaics*, vol. 4, no. 6, pp. 1465–1469, 2014.
- [6] J. Nakamura, N. Asano, T. Hieda, C. Okamoto, T. Ohnishi, M. Kobayashi, H. Tadokoro, R. Suganuma, Y. Matsumoto, H. Katayama, K. Higashi, T. Kamikawa, K. Kimoto, M. Harada, T. Sakai, H. Shigeta, T. Kuniyoshi, K. Tsujino, L. Zou, N. Koide, and K. Nakamura, “Development of heterojunction back contact Si solar cells,” in *Proceedings of the 29th European Photovoltaic Solar Energy Conference and Exhibition*, 2014, pp. 373–375.
- [7] M. A. Green, K. Emery, Y. Hishikawa, W. Warta, and E. D. Dunlop, “Solar cell efficiency tables (version 44),” *Progress in Photovoltaics: Research and Applications*, vol. 22, no. 7, pp. 701–710, 2014.
- [8] D. D. Smith, P. J. Cousins, A. Masad, S. Westerberg, M. Defensor, R. Ilaw, T. Dennis, R. Daquin, N. Bergstrom, A. Leygo, X. Zhu, B. Meyers, B. Bourne, M. Shields, and D. Rose, “Sunpower’s maxeon gen III solar cell: High efficiency and energy yield,” in *Proceedings of the 39th IEEE Photovoltaic Specialists Conference*, 2013, pp. 0908–0913.
- [9] W. Luft, “Solar cell interconnector design,” *IEEE Transactions on Aerospace and Electronic Systems*, vol. 7, no. 5, pp. 781–791, 1971.
- [10] D. J. Curtin and W. J. Billerbeck, “Development of advanced interconnectors for solar cells,” *COMSAT Technical Review*, vol. 4, no. 1, pp. 53–68, 1974. [Online]. Available: http://www.comara.org/legacy/ctr/CTR_V04-1_Spring_1974.pdf
- [11] P. Verlinden, Z. YingBin, and F. ZhiQiang, “Cost analysis of current PV production and strategy for future silicon PV modules,” in *Proceedings of the 28th European Photovoltaic Solar Energy Conference and Exhibition*, 2013, 2BP.1.2.
- [12] J. R. Davis, A. Rohatgi, R. H. Hopkins, P. D. Blais, P. Rai-Choudhury, J. R. McCormick, and H. C. Mollenkopf, “Impurities in silicon solar cells,” *IEEE Transactions on Electron Devices*, vol. 27, no. 4, pp. 677–687, 1980.

- [13] J. Schmidt, "Temperature- and injection-dependent lifetime spectroscopy for the characterization of defect centers in semiconductors," *Applied Physics Letters*, vol. 82, no. 13, pp. 2178–2180, 2003.
- [14] P. Rosenits, T. Roth, S. W. Glunz, and S. Beljakowa, "Determining the defect parameters of the deep aluminum-related defect center in silicon," *Applied Physics Letters*, vol. 91, no. 12, 122109, 2007.
- [15] R. Bock, P. P. Altermatt, J. Schmidt, and R. Brendel, "Formation of aluminum–oxygen complexes in highly aluminum-doped silicon," *Semiconductor Science and Technology*, vol. 25, no. 10, 105007, 2010.
- [16] J. Schmidt, N. Thiemann, R. Bock, and R. Brendel, "Recombination lifetimes in highly aluminum-doped silicon," *Journal of Applied Physics*, vol. 106, no. 9, 093707, 2009.
- [17] O. Krause, H. Ryssel, and P. Pichler, "Determination of aluminum diffusion parameters in silicon," *Journal of Applied Physics*, vol. 91, no. 9, pp. 5645–5649, 2002.
- [18] E. R. Weber, "Transition metals in silicon," *Applied Physics A Materials Science & Processing*, vol. 30, no. 1, pp. 1–22, 1983.
- [19] M. Hourai, K. Murakami, T. Shigematsu, N. Fujino, and T. Shiraiwa, "Behavior of defects induced by metallic impurities on Si(100) surfaces," *Japanese Journal of Applied Physics*, vol. 28, no. 12, pp. 2413–2420, 1989.
- [20] S. M. Myers, M. Seibt, and W. Schröter, "Mechanisms of transition-metal gettering in silicon," *Journal of Applied Physics*, vol. 88, no. 7, pp. 3795–3819, 2000.
- [21] A. M. Gabor, M. Ralli, S. Montminy, L. Alegria, C. Bordonaro, J. Woods, and L. Felton, "Soldering induced damage to thin Si solar cells and detection of cracked cells in modules," in *Proceedings of the 21st European Photovoltaic Solar Energy Conference and Exhibition*, 2006, pp. 2042–2047.
- [22] J. Wendt, M. Träger, M. Mette, A. Pfennig, and B. Jäckel, "The link between mechanical stress induced by soldering and micro damages in silicon solar cells," in *Proceedings of the 24th European Photovoltaic Solar Energy Conference and Exhibition*, 2009, pp. 3420–3422.
- [23] M. Sander, B. Henke, H. Schwarz, S. Dietrich, S. Schweizer, M. Ebert, J. Bagdahn, N. G. Dhere, J. H. Wohlgemuth, and K. Lynn, "Characterization of PV modules by combining results of mechanical and electrical analysis methods," in *SPIE Solar Energy + Technology*, ser. SPIE Proceedings, vol. 7773, 2010, pp. 777 308–1–12.
- [24] S. Dietrich, M. Pander, M. Sander, U. Zeller, M. Ebert, N. G. Dhere, J. H. Wohlgemuth, and K. W. Lynn, "Stress analysis of encapsulated solar cells by means of superposition of thermal and mechanical stresses," in *SPIE Solar Energy + Technology*, ser. SPIE Proceedings, vol. 8825, 2013, pp. 882 505–1–882 505–10.
- [25] A. S. Budiman, G. Illya, V. Handara, W. A. Caldwell, C. Bonelli, M. Kunz, N. Tamura, and D. Verstraeten, "Enabling thin silicon technologies for next generation c-Si solar PV renewable energy systems using synchrotron X-ray microdiffraction as stress and crack mechanism probe," *Solar Energy Materials and Solar Cells*, vol. 130, pp. 303–308, 2014.
- [26] S. A. Mann, M. J. de Wild-Scholten, V. M. Fthenakis, W. G. J. H. M. van Sark, and W. C. Sinke, "The energy payback time of advanced crystalline silicon PV modules in 2020: a prospective study," *Progress in Photovoltaics: Research and Applications*, vol. 22, no. 11, pp. 1180–1194, 2014.
- [27] T. Tiedje, E. Yablonovitch, G. D. Cody, and B. G. Brooks, "Limiting efficiency of silicon solar cells," *IEEE Transactions on Electron Devices*, vol. 31, no. 5, pp. 711–716, 1984.
- [28] Y. Schiele, F. Book, S. Seren, G. Hahn, and B. Terheiden, "Screen-printed Al-alloyed rear junction solar cell concept applied to very thin (100 μm) large-area n-type Si wafers," *Energy Procedia*, vol. 27, pp. 460–466, 2012.

- [29] M. Taguchi, A. Yano, S. Tohoda, K. Matsuyama, Y. Nakamura, T. Nishiwaki, K. Fujita, and E. Maruyama, "24.7% record efficiency HIT solar cell on thin silicon wafer," *IEEE Journal of Photovoltaics*, vol. 4, no. 1, pp. 96–99, 2014.
- [30] D. M. Powell, M. T. Winkler, H. J. Choi, C. B. Simmons, D. B. Needleman, and T. Buonassisi, "Crystalline silicon photovoltaics: a cost analysis framework for determining technology pathways to reach baseload electricity costs," *Energy & Environmental Science*, vol. 5, no. 3, pp. 5874–5883, 2012.
- [31] G. Raisbeck, "The solar battery," *Scientific American*, vol. 193, no. 6, pp. 102–110, 1955.
- [32] M. A. Green, "Silicon photovoltaic modules: a brief history of the first 50 years," *Progress in Photovoltaics: Research and Applications*, vol. 13, no. 5, pp. 447–455, 2005.
- [33] R. Sinton and R. Swanson, "Simplified backside-contact solar cells," *IEEE Transactions on Electron Devices*, vol. 37, no. 2, pp. 348–352, 1990.
- [34] E. van Kerschaver and G. Beaucarne, "Back-contact solar cells: a review," *Progress in Photovoltaics: Research and Applications*, vol. 14, no. 2, pp. 107–123, 2006.
- [35] E. Franklin, K. Fong, K. McIntosh, A. Fell, A. Blakers, T. Kho, D. Walter, D. Wang, N. Zin, M. Stocks, E.-C. Wang, N. Grant, Y. Wan, Y. Yang, X. Zhang, Z. Feng, and P. J. Verlinden, "Design, fabrication and characterisation of a 24.4% efficient interdigitated back contact solar cell," *Progress in Photovoltaics: Research and Applications*, p. n/a, 2014.
- [36] J. Nakamura, N. Asano, T. Hieda, C. Okamoto, H. Katayama, and K. Nakamura, "Development of heterojunction back contact Si solar cells," *IEEE Journal of Photovoltaics*, vol. 4, no. 6, pp. 1491–1495, 2014.
- [37] P. N. Dejong, "Solar cell contact design," Patent US3 903 428 A, 1975. [Online]. Available: <http://www.google.com/patents/US3903428>
- [38] D. R. Lillington, J. R. Kukulka, A. V. Mason, B. L. Sater, and J. Sanchez, "Optimization of silicon 8 cm*8 cm wrapthrough space station cells for 'on orbit' operation," in *Proceedings of the 20th IEEE Photovoltaic Specialist Conference*, 1988, pp. 934–939.
- [39] J. M. Gee, W. K. Schubert, and P. A. Basore, "Emitter wrap-through solar cell," in *Proceedings of the 23rd IEEE Photovoltaic Specialist Conference*, 1993, pp. 265–270.
- [40] M. D. Lammert and R. J. Schwartz, "The interdigitated back contact solar cell: A silicon solar cell for use in concentrated sunlight," *IEEE Transactions on Electron Devices*, vol. 24, no. 4, pp. 337–342, 1977.
- [41] R. M. Swanson, S. K. Beckwith, R. A. Crane, W. D. Eades, Y. H. Kwark, R. A. Sinton, and S. E. Swirhun, "Point-contact silicon solar cells," *IEEE Transactions on Electron Devices*, vol. 31, no. 5, pp. 661–664, 1984.
- [42] A. Goetzberger and V. U. Hoffmann, *Photovoltaic solar energy generation*, ser. Springer series in optical sciences. Berlin: Springer, 2005, vol. 112.
- [43] C. Reichel, F. Granek, M. Hermle, and S. W. Glunz, "Investigation of electrical shading effects in back-contacted back-junction silicon solar cells using the two-dimensional charge collection probability and the reciprocity theorem," *Journal of Applied Physics*, vol. 109, no. 2, 024507, 2011.
- [44] M. Hermle, F. Granek, O. Schultz-Wittmann, and S. W. Glunz, "Shading effects in back-junction back-contacted silicon solar cells," in *Proceedings of the 33rd IEEE Photovoltaic Specialist Conference*, 2008, pp. 412–415.
- [45] N.-P. Harder, V. Mertens, and R. Brendel, "Numerical simulations of buried emitter back-junction solar cells," *Progress in Photovoltaics: Research and Applications*, vol. 17, no. 4, pp. 253–263, 2009.

- [46] P. Engelhart, N.-P. Harder, A. Merkle, R. Grischke, R. Meyer, and R. Brendel, "RISE: 21.5% efficient back junction silicon solar cell with laser technology as a key processing tool," in *Proceedings of the 4th World Conference on Photovoltaics Energy Conversion*, 2006, pp. 900–904.
- [47] N.-P. Harder, V. Mertens, and R. Brendel, "Buried emitter solar cell structures: Decoupling of metallisation geometry and carrier collection geometry of back contacted solar cells," *physica status solidi (RRL) - Rapid Research Letters*, vol. 2, no. 4, pp. 148–150, 2008.
- [48] C. Reichel, F. Granek, M. Hermle, and S. W. Glunz, "Back-contacted back-junction n -type silicon solar cells featuring an insulating thin film for decoupling charge carrier collection and metallization geometry," *Progress in Photovoltaics: Research and Applications*, vol. 21, no. 5, pp. 1063–1076, 2013.
- [49] J. Robbelein, B. Vermang, T. Janssens, and N. P. J. Posthuma, "Passivation layers for large area interdigitated back junction cells and their electrical isolation properties," in *Proceedings of the 26th European Photovoltaic Solar Energy Conference and Exhibition*, 2011, pp. 1008–1013.
- [50] R. Keding, R. Bock, A. Bochow, K. Katkhouda, D. Stüwe, C. Reichel, F. Clement, R. Woehl, H. Reinecke, and T. Geppert, "Study of the electrical insulation of dielectric passivation layers and stacks for back-contact back-junction silicon solar cells," in *Proceedings of the 28th European Photovoltaic Solar Energy Conference and Exhibition*, 2013, pp. 961–966.
- [51] A. Merkle, H. Schulte-Huxel, S. Blankemeyer, I. Feilhaber, R. Bock, V. Steckenreiter, S. Kajari-Schroeder, N.-P. Harder, and R. Brendel, "From high-efficiency n-type solar cells to modules exceeding 20% efficiency with aluminum-based cell interconnection," *Progress in Photovoltaics: Research and Applications*, vol. 21, no. 6, pp. 1354–1362, 2013.
- [52] P. Hacke, B. Murphy, D. Meakin, J. Dominguez, J. Jaramillo, M. Yamasaki, and J. Gee, "Busbarless emitter wrap-through solar cells and modules," in *Proceedings of the 33rd IEEE Photovoltaic Specialist Conference*, 2008, pp. 1–5.
- [53] G. Humpston and D. M. Jacobson, *Principles of soldering*. Materials Park, Ohio: ASM International, 2004.
- [54] A. H. Fritz and G. Schulze, *Fertigungstechnik*, 10th ed., ser. Springer-Lehrbuch. Berlin, Heidelberg: Springer, 2012. [Online]. Available: <http://dx.doi.org/10.1007/978-3-642-29786-1>
- [55] M. Gast, M. Köntges, and R. Brendel, "In-laminate laser soldering – a gentle method to assemble and interconnect silicon solar cells to modules," in *Proceedings of the 21st European Photovoltaic Solar Energy Conference and Exhibition*, 2006, pp. 2133–2136.
- [56] U. Eitner and L. C. Rendler, "The mechanical theory behind the peel test," *Energy Procedia*, vol. 55, pp. 331–335, 2014.
- [57] M. Köntges, S. Kurtz, C. Packard, U. Jahn, K. A. Berger, K. Kato, T. Friesen, H. Liu, and M. Iseghem, *Performance and Reliability of Photovoltaic Systems: Subtask 3.2: Review of Failures of Photovoltaic Modules*. International Energy Agency (IEA), 2014.
- [58] E. Hasselbrink, M. Anderson, Z. Defreitas, M. Mikofski, Y.-C. Shen, S. Caldwell, A. Terao, D. Kavulak, Z. Campeau, and D. DeGraaff, "Validation of the PVLife model using 3 million module-years of live site data," in *Proceedings of the 39th IEEE Photovoltaic Specialists Conference*, 2013, pp. 0007–0012.
- [59] M. Heimann, P. Klaerner, C. Luechinger, A. Mette, J. Mueller, M. Traeger, T. Barthel, O. Valentin, and P. Wawer, "Ultrasonic bonding of aluminum ribbons to interconnect high-efficiency crystalline-silicon solar cells," *Energy Procedia*, vol. 27, pp. 670–675, 2012.
- [60] V. Jung and M. Köntges, "Al/Ni:V/Ag metal stacks as rear-side metallization for crystalline silicon solar cells," *Progress in Photovoltaics: Research and Applications*, vol. 21, no. 5, pp. 876–883, 2012.

-
- [61] G. P. Willeke and E. R. Weber, *Advances in Photovoltaics*. Burlington: Elsevier Science, 2013. [Online]. Available: <http://gbv.ebib.com/patron/FullRecord.aspx?p=1495637>
- [62] J.-H. Kim, J. Park, D. Kim, and N. Park, "Study on mitigation method of solder corrosion for crystalline silicon photovoltaic modules," *International Journal of Photoenergy*, vol. 2014, no. 7, pp. 1–9, 2014.
- [63] "Directive 2002/95/EC of the european parliament and of the council of 27 january 2003 on the restriction of the use of certain hazardous substances in electrical and electronic equipment (ROHS)." *Official Journal of the European Union*, no. L 37, pp. 19–23, 2003. [Online]. Available: <http://eur-lex.europa.eu/LexUriServ/LexUriServ.do?uri=OJ:L:2003:037:0019:0023:en:PDF>
- [64] I. Duerr, C. Peike, S. Hoffmann, M. Koehl, and K.-A. Weiß, "X-ray study on damp-heat induced cell degradation (DHID)," in *Proceedings of the 28th European Photovoltaic Solar Energy Conference and Exhibition*, 2013, pp. 3300–3302.
- [65] W. Palitzsch and U. Loser, "Economic PV waste recycling solutions - results from R&D and practice," in *Proceedings of the 38th IEEE Photovoltaic Specialists Conference*, 2012, pp. 628–631.
- [66] E. Klugmann-Radziemska, P. Ostrowski, K. Drabczyk, P. Panek, and M. Szkodo, "Experimental validation of crystalline silicon solar cells recycling by thermal and chemical methods," *Solar Energy Materials and Solar Cells*, vol. 94, no. 12, pp. 2275–2282, 2010.
- [67] R. B. Roberts, "Thermal expansion reference data: silicon 300-850 K," *Journal of Physics D: Applied Physics*, vol. 14, no. 10, pp. L163–L166, 1981.
- [68] M. Mayr, *Technische Mechanik: Statik, Kinematik, Kinetik, Schwingungen, Festigkeitslehre*, 2nd ed., ser. Hanser-Lehrbuch. München: Hanser, 1999.
- [69] D. Rose and S. Daroczi, "Development and manufacture of reliable PV modules with >17% efficiency," in *Proceedings of the 20th European Photovoltaic Solar Energy Conference*, 2005, pp. 2406–2409.
- [70] M. Köntges, M. Gast, R. Brendel, R. Meyer, and A. M. P. Giegerich, "A novel photovoltaic-module assembly system for back contact solar cells using laser soldering technique," in *Proceedings of the 23rd European Photovoltaic Solar Energy Conference*, 2008, pp. 2709–2712.
- [71] A. van der Heide, D. Griebeski, and J. Szlufcik, "Fabrication of multi-crystalline MWT cells with interconnection flexibility of 16.5% efficiency," in *Proceedings of the 24th European Photovoltaic Solar Energy Conference and Exhibition*, 2009, pp. 942–945.
- [72] J. Libal, F. Fizzotti, F. Traverso, V. Mihailetchi, G. Galbiati, A. Halm, R. Roescu, L. Koduvellikulathu, C. Comparotto, R. Kopecek, and K. Peter, "High efficiency n-type IBC solar cells for industrial production," *presented at 2nd nPV-Workshop 2012, Amsterdam, The Neatherlands*, 2012.
- [73] X. Zhang, Y. Yang, W. Liu, K. Zhang, Y. Chen, Z. Li, G. Xu, H. Jiao, S. Zhang, Z. Feng, and P. J. Verlinden, "Development of high efficiency interdigitated back contact silicon solar cells and modules with industrial processing technologies," in *Proceedings of the 6th World Conference on Photovoltaic Energy Conversion*, 2014, pp. 509–510.
- [74] J. H. Bultman, D. W. K. Eikelboom, R. Kinderman, A. C. Tip, C. J. J. Tool, M. A. C. J. van den Nieuwenhof, C. Schoofs, F. M. Schuurmans, and A. W. Weeber, "Fast and easy single step module assembly for back-contacted c-Si solar cells with conductive adhesives," in *Proceedings of the 3rd World Conference on Photovoltaic Energy Conversion*, 2003, pp. 979–982.
- [75] U. Eitner, D. Eberlein, and M. Tranzitz, "Interconnector-based module technology for thin MWT cells," in *Proceedings of the 27th European Photovoltaic Solar Energy Conference and Exhibition*, 2012, pp. 3461–3464.

- [76] P. C. de Jong, D. W. K. Eikelboom, R. Kinderman, A. C. Tip, H. J. Bultman, M. H. H. Meuwissen, and M. A. C. J. Nieuwenhof, "Single-step laminated full-size pv modules made with back-contacted mc-Si cells and conductive adhesives," in *Proceedings of the 19th European Photovoltaic Solar Energy Conference*, 2004, pp. 2145–2148.
- [77] A. Metz, D. Adler, S. Bagus, H. Blanke, M. Bothar, E. Brouwer, S. Dauwe, K. Dressler, R. Droessler, T. Droste, M. Fiedler, Y. Gassenbauer, T. Grahl, N. Hermert, W. Kuzminski, A. Lachowicz, T. Lauinger, N. Lenck, M. Manole, M. Martini, R. Messmer, C. Meyer, J. Moschner, K. Ramspeck, P. Roth, R. Schönfelder, B. Schum, J. Sticksel, K. Vaas, M. Volk, and K. Wangemann, "Industrial high performance crystalline silicon solar cells and modules based on rear surface passivation technology," *Solar Energy Materials and Solar Cells*, vol. 120, pp. 417–425, 2014.
- [78] T. Geipel and U. Eitner, "Cure kinetics of electrically conductive adhesives," *Energy Procedia*, vol. 38, pp. 340–347, 2013.
- [79] T. Geipel, M. Z. Huq, and U. Eitner, "Reliable interconnection of the front side grid fingers using silver-reduced conductive adhesives," *Energy Procedia*, vol. 55, pp. 336–341, 2014.
- [80] J. M. Gee, S. E. Garrett, and W. P. Morgan, "Simplified module assembly using back-contact crystalline-silicon solar cells." in *Proceedings of the 26th IEEE Photovoltaic Specialists Conference*, 1997, pp. 1085–1088.
- [81] S. Schwertheim, M. Scherff, T. Mueller, W. R. Fahrner, and H. C. Neitzert, "Lead-free electrical conductive adhesives for solar cell interconnectors," in *Proceedings of the 33rd IEEE Photovoltaic Specialist Conference*, 2008, pp. 1–6.
- [82] M. W. P. E. Lamers, C. Tjengdrawira, M. Koppes, I. J. Bennett, E. E. Bende, T. P. Visser, E. Kossen, B. Brockholz, A. A. Mewe, I. G. Romijn, E. Sauar, L. Carnel, S. Julsrud, T. Naas, P. C. de Jong, and A. W. Weeber, "17.9% metal-wrap-through mc-Si cells resulting in module efficiency of 17.0%," *Progress in Photovoltaics: Research and Applications*, vol. 20, no. 1, pp. 62–73, 2012.
- [83] I. J. Bennett and N. Loiseaux, "Measurement of strains in MWT modules during manufacture," *Energy Procedia*, vol. 27, pp. 697–702, 2012.
- [84] S. W. Britten, R. S. B. Sundaram, A. Olowinsky, and A. Gillner, "Quasi-simultaneous laser soldering for the interconnection of back-contact solar cells with composite foils," in *Laser-based Micro- and Nanoprocessing VIII, 8968*, ser. SPIE Proceedings, 2014, 89680V.
- [85] P. Verlinden, R. Sinton, and R. Swanson, "High efficiency large area back contact concentrator solar cells with a multilevel interconnection," *International Journal of Solar Energy*, vol. 6, no. 6, pp. 347–366, 1988.
- [86] P. Verlinden, R. Swanson, R. Sinton, and D. Kane, "Multilevel metallization for large area point-contact solar cells," in *Proceedings of the 20th IEEE Photovoltaic Specialist Conference*, 1988, pp. 532–537.
- [87] D. Bäuerle, *Laser Processing and Chemistry*. Berlin and Heidelberg: Springer, 2011.
- [88] R. J. Harrach, "Analytical solutions for laser heating and burnthrough of opaque solid slabs," *Journal of Applied Physics*, vol. 48, no. 6, pp. 2370–2383, 1977.
- [89] H. S. Carslaw, *Introduction to the theory of Fourier's series and integrals*, 2nd ed. London: Macmillan, 1921.
- [90] T. R. Goodman, "Application of integral methods to transient nonlinear heat transfer," *Advances in Heat Transfer*, vol. 1, pp. 51–122, 1964.
- [91] R. J. Harrach, "Estimates on the ignition of high-explosives by laser pulses," *Journal of Applied Physics*, vol. 47, no. 6, pp. 2473–2482, 1976.

-
- [92] W. M. Steen and J. Mazumder, *Laser material processing*, 4th ed. London: Springer-Verlag London, 2010. [Online]. Available: <http://dx.doi.org/10.1007/978-1-84996-062-5>
- [93] G. Heise, M. Englmaier, C. Hellwig, T. Kuznicki, S. Sarrach, and H. P. Huber, "Laser ablation of thin molybdenum films on transparent substrates at low fluences," *Applied Physics A*, vol. 102, no. 1, pp. 173–178, 2011.
- [94] F. J. Adrian, "A study of the mechanism of metal deposition by the laser-induced forward transfer process," *Journal of Vacuum Science & Technology B: Microelectronics and Nanometer Structures*, vol. 5, no. 5, pp. 1490–1494, 1987.
- [95] V. Schultze and M. Wagner, "Blow-off of aluminium films," *Applied Physics A Solids and Surfaces*, vol. 53, no. 3, pp. 241–248, 1991.
- [96] K. Feldmann, V. Schöppner, and G. Spur, Eds., *Handbuch Fügen, Handhaben, Montieren*, 2nd ed., ser. Handbuch der Fertigungstechnik. München: Hanser, 2014, vol. 5.
- [97] T. Hirano, M. Demura, K. Kishida, K. Minamida, and Y. Xu, "Laser spot welding of cold-rolled boron-free Ni₃Al foils," *Metallurgical and Materials Transactions A*, vol. 38, no. 5, pp. 1041–1047, 2007.
- [98] D. P'ng and P. Molian, "Q-switch Nd:YAG laser welding of AISI 304 stainless steel foils," *Materials Science and Engineering: A*, vol. 486, no. 1-2, pp. 680–685, 2008.
- [99] V. A. Ventrella, J. R. Berretta, and W. d. Rossi, "Pulsed Nd:YAG laser welding of Ni-alloy Hastelloy C-276 foils," *Physics Procedia*, vol. 39, pp. 569–576, 2012.
- [100] A. Patschger, J. Bliedtner, and J. P. Bergmann, "Approaches to increase process efficiency in laser micro welding," *Physics Procedia*, vol. 41, pp. 592–602, 2013.
- [101] M. Ehrhard and K. Zimmer, "Laser micro joining of thin metal films on flexible substrates for mechanical and electrical connections," in *Laser-based Micro- and Nanopackaging and Assembly V, 7921*, ser. SPIE Proceedings, 2011, 792109.
- [102] M. Ehrhardt, P. Lorenz, C. Scheit, A. Wehrmann, K. Zimmer, and L. Gerlach, "Low-damage micro-interconnection with nanosecond laser pulses for high-efficient gaas solar cells," in *11th International Conference on Laser Ablation*, 2011, PMO79.
- [103] M. I. S. Ismail, Y. Okamoto, A. Okada, Y. Uno, and K. Ueoka, "Direct micro-joining of flexible printed circuit and metal electrode by pulsed Nd:YAG laser," *International Journal of Precision Engineering and Manufacturing*, vol. 13, no. 3, pp. 321–329, 2012.
- [104] R. Buhs, "Layout and technology of the CTS solar array blanket," in *Proceedings of the 10th IEEE Photovoltaic Specialists Conference*, 1973, pp. 296–306.
- [105] K. K. Reinhartz and J. J. Capart, "Status of welded solar cell module technology at ESRO," in *Proceedings of the 9th IEEE Photovoltaic Specialists Conference*, 1970, pp. 287–292.
- [106] H. G. Mesch, "Parallel gap welding of silver plated solar cells," in *Proceedings of the 10th IEEE Photovoltaic Specialists Conference*, 1973, pp. 275–280.
- [107] H. S. Rauschenbach, *Solar cell array design handbook: The principles and technology of photovoltaic energy conversion*. New York: Van Nostrand Reinhold, 1980.
- [108] R. Buhs, "Silicon solar cell arrays technical status, terrestrial applications, and future developments for low cost production," in *Proceedings of the 13th IEEE Photovoltaic Specialists Conference*, 1978, pp. 262–267.
- [109] A. Moalem, A. Schoonderbeek, R. Kling, and A. Ostendorf, "Advancing laser joining in solar module manufacturing," in *Proceedings of the 17th international Photovoltaics Science and Engineering*, 2007, pp. 438–439.

- [110] A. Moalem, A. Schoonderbeek, R. Kling, U. Stute, and B. Denkena, "Laser micro welding in silicon solar module manufacturing," in *Proceedings of the 8th International Symposium on Laser Precision Microfabrication*, 2007.
- [111] R. Hendel, B. Lehner, and C. Rüttimann, "Faster and reliable joining of solar cells: Bi-wavelength laser welding for photovoltaic module integration," *Laser Technik Journal*, vol. 9, no. 1, pp. 20–23, 2012.
- [112] J. M. Liu, "Simple technique for measurements of pulsed gaussian-beam spot sizes," *Optics Letters*, vol. 7, no. 5, pp. 196–198, 1982.
- [113] SCHOTT Technical Glass Solutions GmbH, "Schott borofloat® 33." [Online]. Available: http://www.schott.com/borofloat/german/download/borofloat_33_de.pdf
- [114] W. Kern and D. Puotinen, "Cleaning solutions based on hydrogen peroxide for use in silicon semiconductor technology," *RCA Review: A Technical Journal*, vol. 31, pp. 187–206, 1970.
- [115] W. Kern, "The evolution of silicon wafer cleaning technology," *Journal of The Electrochemical Society*, vol. 137, no. 6, pp. 1887–1892, 1990.
- [116] P. Engelhart, A. Teppe, A. Merkle, R. Grischke, and R. Meyer, "The RISE-EWT solar cell a new approach towards simple high efficiency silicon solar cells." in *Proceedings of the 15th International Photovoltaic Science and Engineering Conference*, 2005, pp. 802–803.
- [117] S. Hermann, P. Engelhart, A. Merkle, T. Neubert, T. Brendemühl, R. Meyer, N.-P. Harder, and R. Brendel, "21.4%-efficient emitter wrap-through RISE solar cell on large area and picosecond laser processing of local contact openings," in *Proceedings of the 22nd European Photovoltaic Solar Energy Conference*, 2007, pp. 970–973.
- [118] R. A. Sinton, P. Verlinden, D. E. Kane, and R. M. Swanson, "Development efforts in silicon backside-contact solar cells," in *Proceedings of the 17th European Photovoltaic Solar Energy Conference and Exhibition*, 1988, pp. 1472–1475.
- [119] H. Schulte-Huxel, S. Blankemeyer, A. Merkle, V. Steckenreiter, S. Kajari-Schröder, and R. Brendel, "Interconnection of busbar-free back contacted solar cells by laser welding," *Progress in Photovoltaics: Research and Applications*, vol. 23, no. 8, pp. 1057–1065, 2015.
- [120] H. Schulte-Huxel, S. Blankemeyer, R. Bock, A. Merkle, S. Kajari-Schröder, and R. Brendel, "Aging behaviour of laser welded Al-interconnections in crystalline silicon modules," *Solar Energy Materials and Solar Cells*, vol. 106, pp. 22–26, 2012.
- [121] K. Ramspeck, "Characterization techniques for silicon solar cells and material using an infrared-camera based approach," Ph.D. dissertation, Leibniz Universität Hannover, Hannover, 2009. [Online]. Available: <http://d-nb.info/995862753/04>
- [122] K. Ramspeck, K. Bothe, J. Schmidt, and R. Brendel, "Combined dynamic and steady-state infrared camera based carrier lifetime imaging of silicon wafers," *Journal of Applied Physics*, vol. 106, no. 11, 114506, 2009.
- [123] J. Müller, "Characterisation of local aluminum-alloyed contacts to silicon solar cells," Ph.D. dissertation, Leibniz Universität Hannover, Hannover, 2013. [Online]. Available: <http://edok01.tib.uni-hannover.de/edoks/e01dh13/773536930.pdf>
- [124] J. Müller, K. Bothe, S. Gatz, F. Haase, C. Mader, and R. Brendel, "Recombination at laser-processed local base contacts by dynamic infrared lifetime mapping," *Journal of Applied Physics*, vol. 108, no. 12, 124513, 2010.
- [125] J. Isenberg, "Realistic evaluation of power losses in solar cells by using thermographic methods," *Journal of Applied Physics*, vol. 95, no. 9, pp. 5200–5209, 2004.
- [126] M. Kasemann, B. Walter, C. Meinhardt, J. Ebser, W. Kwopil, and W. Warta, "Emissivity-corrected power loss calibration for lock-in thermography measurements on silicon solar cells," *Journal of Applied Physics*, vol. 103, no. 11, 113503, 2008.

-
- [127] T. Fuyuki, H. Kondo, T. Yamazaki, Y. Takahashi, and Y. Uraoka, "Photographic surveying of minority carrier diffusion length in polycrystalline silicon solar cells by electroluminescence," *Applied Physics Letters*, vol. 86, no. 26, 262108, 2005.
- [128] D. Hinken, "Luminescence-based characterization of crystalline silicon solar cells," Ph.D. dissertation, Leibniz Universität Hannover, Hannover, 2012. [Online]. Available: <http://edok01.tib.uni-hannover.de/edoks/e01dh12/717174778.pdf>
- [129] T. Trupke, E. Pink, R. A. Bardos, and M. D. Abbott, "Spatially resolved series resistance of silicon solar cells obtained from luminescence imaging," *Applied Physics Letters*, vol. 90, no. 9, 093506, 2007.
- [130] T. Trupke, R. A. Bardos, M. C. Schubert, and W. Warta, "Photoluminescence imaging of silicon wafers," *Applied Physics Letters*, vol. 89, no. 4, 044107, 2006.
- [131] J. D. Zook, "Effects of grain boundaries in polycrystalline solar cells," *Applied Physics Letters*, vol. 37, no. 2, pp. 223–226, 1980.
- [132] A. Goetzberger, J. Knobloch, B. Voss, and R. Waddington, *Crystalline silicon solar cells*. Chichester: Wiley, 1998.
- [133] B. L. Sopori and A. Baghdadi, "Some investigations on the influence of defects/grain boundaries on photovoltaic mechanisms in polycrystalline silicon films," *Solar Cells*, vol. 1, no. 3, pp. 237–250, 1980.
- [134] J. Marek, "Light-beam-induced current characterization of grain boundaries," *Journal of Applied Physics*, vol. 55, no. 2, pp. 318–326, 1984.
- [135] "Crystalline silicon terrestrial photovoltaic (PV) modules - design qualification and type approval," Norm IEC 61215:2005, VDE Verlag Berlin. [Online]. Available: <https://www.vde-verlag.de/normen/0126004/din-en-61215-vde-0126-31-2006-02.html>
- [136] J. Zhao, A. Wang, and M. A. Green, "24.5% efficiency silicon PERT cells on MCZ substrates and 24.7% efficiency PERL cells on FZ substrates," *Progress in Photovoltaics: Research and Applications*, vol. 7, no. 6, pp. 471–474, 1999.
- [137] F. Kiefer, R. Peibst, T. Ohrdes, J. Krügener, H. J. Osten, and R. Brendel, "Emitter recombination current densities of boron emitters with silver/aluminum pastes," in *Proceedings of the 40th IEEE Photovoltaic Specialists Conference*, 2014, pp. 2808–2812.
- [138] J. Nekarda, D. Reinwand, A. Grohe, P. Hartmann, R. Preu, R. Trassl, and R. Wieder, "Industrial pvd metallization for high efficiency crystalline silicon solar cells," in *Proceedings of the 34th IEEE Photovoltaic Specialist Conference*, 2009, pp. 892–896.
- [139] H. Schulte-Huxel, S. Blankemeyer, R. Bock, A. Merkle, S. Kajari-Schröder, and R. Brendel, "Al-foil on encapsulant for the interconnection of Al-metalized silicon solar cells," *IEEE Journal of Photovoltaics*, vol. 3, no. 1, pp. 77–82, 2013.
- [140] E. Matthias, M. Reichling, J. Siegel, O. W. Käding, S. Petzoldt, H. Skurk, P. Bizenberger, and E. Neske, "The influence of thermal diffusion on laser ablation of metal films," *Applied Physics A Solids and Surfaces*, vol. 58, no. 2, pp. 129–136, 1994.
- [141] K. Ujihara, "Reflectivity of metals at high temperatures," *Journal of Applied Physics*, vol. 43, no. 5, pp. 2376–2383, 1972.
- [142] B. Hüttner, "Optical properties of polyvalent metals in the solid and liquid state: aluminium," *Journal of Physics: Condensed Matter*, vol. 6, no. 13, pp. 2459–2474, 1994.
- [143] H. Schulte-Huxel, S. Blankemeyer, S. Kajari-Schröder, and R. Brendel, "Laser microwelding of thin Al layers for interconnection of crystalline Si solar cells: analysis of process limits for ns and μ s lasers," *Journal of Photonics for Energy*, vol. 4, no. 1, 041597, 2014.

- [144] J. E. Hatch, *Aluminum: Properties and physical metallurgy*. Metals Park, OH: American Society for Metals, 1984. [Online]. Available: <http://site.ebrary.com/lib/alltitles/docDetail.action?docID=10323430>
- [145] COMSOL Multiphysics® Modeling Software, Version 4.3, Comsol AB, Stockholm, Sweden.
- [146] L. F. Mondolfo, *Aluminum alloys: structure and properties*. London: Butterworths, 1976.
- [147] V. V. Semak, G. A. Knorovsky, D. O. MacCallum, and R. A. Roach, "Effect of surface tension on melt pool dynamics during laser pulse interaction," *Journal of Physics D: Applied Physics*, vol. 39, no. 3, pp. 590–595, 2006.
- [148] P. J. Cousins, D. D. Smith, H.-C. Luan, J. Manning, T. D. Dennis, A. Waldhauer, K. E. Wilson, G. Harley, and W. P. Mulligan, "Generation 3: Improved performance at lower cost," in *Proceedings of the 35th IEEE Photovoltaic Specialists Conference*, 2010, pp. 275–278.
- [149] J. Govaerts, S. Nicola Granata, T. Bearda, F. Dross, C. Boulord, G. Beaucarne, F. Korsos, K. Baert, I. Gordon, and J. Poortmans, "Development of a-Si:H/c-Si heterojunctions for the i²-module concept: Low-temperature passivation and emitter formation on wafers bonded to glass," *Solar Energy Materials and Solar Cells*, vol. 113, pp. 52–60, 2013.
- [150] I. Haedrich, U. Eitner, M. Wiese, and H. Wirth, "Unified methodology for determining CTM ratios: Systematic prediction of module power," *Solar Energy Materials and Solar Cells*, vol. 131, pp. 14–23, 2014.
- [151] J. Müller, D. Hinken, S. Blankemeyer, H. Kohlenberg, U. Sonntag, K. Bothe, T. Dullweber, M. Köntges, and R. Brendel, "Resistive power loss analysis of PV modules made from halved $15.6 \times 15.6 \text{ cm}^2$ silicon PERC solar cells with efficiencies up to 20.0%," *IEEE Journal of Photovoltaics*, vol. 5, no. 1, pp. 189–194, 2015.
- [152] M. Ernst, H. Schulte-Huxel, R. Niepelt, S. Kajari-Schröder, and R. Brendel, "Thin crystalline macroporous silicon solar cells with ion implanted emitter," *Energy Procedia*, vol. 38, pp. 910–918, 2013.
- [153] C. Mader, R. Bock, J. Schmidt, and R. Brendel, "Formation of highly aluminum-doped p-type silicon regions by in-line high-rate evaporation," *Solar Energy Materials and Solar Cells*, vol. 95, no. 7, pp. 1720–1722, 2011.
- [154] J. A. Thornton, "High rate thick film growth," *Annual Review of Materials Science*, vol. 7, no. 1, pp. 239–260, 1977.
- [155] U. Eitner, M. Köntges, and R. Brendel, "Use of digital image correlation technique to determine thermomechanical deformations in photovoltaic laminates: Measurements and accuracy," *Solar Energy Materials and Solar Cells*, vol. 94, no. 8, pp. 1346–1351, 2010.
- [156] H. B. Serreze, "Optimizing solar cell performance by simultaneous consideration of grid pattern design and interconnect configuration," in *Proceedings of the 13th IEEE Photovoltaic Specialists Conference*, 1978, pp. 609–614.
- [157] M. A. Green, *Solar cells: Operating principles, technology and system applications*. Kensington, NSW: Univ. of New South Wales, 1992.
- [158] Sentaurus Device User Guide, Version C-2009.06, Synopsys, Inc., Mountain View, CA., USA.
- [159] T. Ohrdes, U. Römer, Y. Larionova, R. Peibst, P. P. Altermatt, and N.-P. Harder, "High fill-factors of back-junction solar cells without front surface field diffusion," in *Proceedings of the 27th European Photovoltaic Solar Energy Conference and Exhibition*, 2012, pp. 866–869.
- [160] I. L. Eisgruber and J. R. Sites, "Extraction of individual-cell photocurrents and shunt resistances in encapsulated modules using large-scale laser scanning," *Progress in Photovoltaics: Research and Applications*, vol. 4, no. 1, pp. 63–75, 1996.

- [161] S. Roschier, G. Agostinelli, and E. D. Dunlop, "Laser scanning of amorphous silicon photovoltaic modules with different bias conditions," *Opto-Electronics Review*, vol. 8, no. 4, pp. 328–332, 2000.
- [162] S. Eidelloth, F. Haase, and R. Brendel, "Simulation tool for equivalent circuit modeling of photovoltaic devices," *IEEE Journal of Photovoltaics*, vol. 2, no. 4, pp. 572–579, 2012.
- [163] F. Granek, M. Hermle, D. M. Huljić, O. Schultz-Wittmann, and S. W. Glunz, "Enhanced lateral current transport via the front n^+ diffused layer of n -type high-efficiency back-junction back-contact silicon solar cells," *Progress in Photovoltaics: Research and Applications*, vol. 17, no. 1, pp. 47–56, 2009.
- [164] A. Teppe, P. Engelhart, and J. Müller, "Method for the contact separation of electrically-conducting layers on the back contacts of solar cells and corresponding solar cell," Patent US20 110 053 312 A1, 2011. [Online]. Available: <http://www.google.com/patents/US20110053312>
- [165] H. Schulte-Huxel, U. Römer, S. Blankemeyer, A. Merkle, Y. Larionova, V. Steckenreiter, R. Peibst, S. Kajari-Schroeder, and R. Brendel, "Two-level metallization and module integration of point-contacted solar cells," *Energy Procedia*, vol. 55, pp. 361–368, 2014.
- [166] R. Peibst, U. Römer, Y. Larionova, H. Schulte-Huxel, T. Ohrdes, M. Häberle, B. Lim, J. Krügener, D. Stichtenoth, T. Wutherich, C. Schollhorn, J. Graff, and R. Brendel, "Building blocks for back-junction back-contacted cells and modules with ion-implanted poly-Si junctions," in *Proceedings of the 40th IEEE Photovoltaic Specialists Conference*, 2014, pp. 0852–0856.
- [167] C. Vargel, *Corrosion of aluminium*, 1st ed. Amsterdam, Boston: Elsevier, 2004. [Online]. Available: <http://site.ebrary.com/lib/alltitles/docDetail.action?docID=10169853>
- [168] W. Geist, "Charakterisierung mechanischer Eigenschaften von Aluminiumfolie unter Berücksichtigung von Laserprozesseinflüssen zur Entwicklung eines Verbindersdesigns mit höherer mechanischer Stabilität für die Verschaltung von Rückkontaktzellen," Bachelor thesis, Fachhochschule Nordhausen, Nordhausen, 2013.
- [169] A. Goodrich, P. Hacke, Q. Wang, B. Sopori, R. Margolis, T. L. James, and M. Woodhouse, "A wafer-based monocrystalline silicon photovoltaics road map: Utilizing known technology improvement opportunities for further reductions in manufacturing costs," *Solar Energy Materials and Solar Cells*, vol. 114, pp. 110–135, 2013.
- [170] A. Schneider, M. Pander, T. Korvenkangas, S. Aulehla, R. Harney, and T. Horttana, "Cell to module loss reduction and module reliability enhancements by solder ribbon optimization," in *Proceedings of the 29th European Photovoltaic Solar Energy Conference and Exhibition*, 2014, pp. 165–170.
- [171] Z. Campeau, M. Anderson, E. Hasselbrink, D. Kavulak, Y.-C. Shen, R. Lacerda, A. Terao, S. Caldwell, Z. Defreitas, L. Leonard, M. Mikofski, D. DeGraaff, and A. S. Budiman, "Sunpower module degradation rate," 2013. [Online]. Available: <http://us.sunpower.com/sites/sunpower/files/media-library/white-papers/wp-sunpower-module-degradation-rate.pdf>
- [172] J. Govaerts, C. Boulord, M. Fisher, G. Beaucarne, I. Gordon, J. Poortmans, and K. Baert, "I-module technology: Evaluation and evolution," in *Proceedings of the 28th European Photovoltaic Solar Energy Conference and Exhibition*, 2013, pp. 59–62.
- [173] I. J. Bennett, P. C. de Jong, M. J. H. Kloos, C. N. J. Stam, A. Henckens, J. Schuermans, R. J. Gomez, P. Sánchez-Friera, B. Lalaguna, and H. Schmidt, "Low-stress interconnection of solar cells," in *Proceedings of the 22nd European Photovoltaic Solar Energy Conference*, 2007, pp. 2674–2678.
- [174] G. TamizhMani, "Testing the reliability and safety of photovoltaic modules: failure rates and temperature effects," *Photovoltaics International*, vol. 8, pp. 146–152, 2010.

- [175] J. Schneider, M. Turek, M. Dyrba, I. Baumann, B. Koll, and T. Booz, “Combined effect of light harvesting strings, anti-reflective coating, thin glass, and high ultraviolet transmission encapsulant to reduce optical losses in solar modules,” *Progress in Photovoltaics: Research and Applications*, vol. 22, no. 7, pp. 830–837, 2014.
- [176] M. R. Vogt, H. Holst, M. Winter, S. Knoc, A. Ruppenthal, R. Brendel, and P. P. Altermatt, “Optical loss analysis of colored pv modules,” in *Proceedings of the 6th World Conference on Photovoltaic Energy Conversion*, 2014, pp. 1115–1116.
- [177] K. R. McIntosh, J. N. Cotsell, J. S. Cumpston, A. W. Norris, N. E. Powell, and B. M. Ketola, “An optical comparison of silicone and EVA encapsulants for conventional silicon PV modules: A ray-tracing study,” in *Proceedings of the 34th IEEE Photovoltaic Specialist Conference*, 2009, pp. 544–549.
- [178] H. Holst, M. Winter, M. R. Vogt, K. Bothe, M. Köntges, R. Brendel, and P. P. Altermatt, “Application of a new ray tracing framework to the analysis of extended regions in Si solar cell modules,” *Energy Procedia*, vol. 38, pp. 86–93, 2013.
- [179] I. Haedrich, M. Wiese, B. Thaidigsman, D. Eberlein, F. Clement, U. Eitner, R. Preu, and H. Wirth, “Minimizing the optical cell-to-module losses for MWT -modules,” *Energy Procedia*, vol. 38, pp. 355–361, 2013.
- [180] F. Dross, E. van Kerschaver, and G. Beaucarne, “Minimization of the shadow-like losses for interdigitated back-junction solar cells,” in *Proceedings of the 15th International Photovoltaic Science and Engineering Conference*, 2005, pp. 971–972.
- [181] S. Kluska, F. Granek, M. Hermle, and S. W. Glunz, “Loss analysis of high-efficiency back-contact back-junction silicon solar cells,” in *Proceedings of the 23rd European Photovoltaic Solar Energy Conference*, 2008, pp. 1590–1595.
- [182] L. Hamann, M. Haas, W. Wille, J. Mattheis, and R. Zapf-Gottwick, “30% silver reduction in rear bus bar metal paste,” *Energy Procedia*, vol. 43, pp. 72–79, 2013.
- [183] F. Kiefer, T. Brendemühl, M. Berger, A. Lohse, S. Kirstein, N. Braun, M. Lehr, F. Heine-meyer, V. Jung, A. Morlier, S. Blankemeyer, I. Kunze, R. Winter, N.-P. Harder, T. Dullweber, M. Köntges, and R. Brendel, “Influence of solder pads to PERC solar cells for module inte-gration,” *Energy Procedia*, vol. 38, pp. 368–374, 2013.
- [184] K. Krauß, F. Fertig, and S. Rein, “Recombination and microstructural properties of soldering pads and their impact on solar cell performance,” *Energy Procedia*, vol. 38, pp. 760–769, 2013.
- [185] H. v. Campe, S. Huber, S. Meyer, S. Reiff, and J. Vietor, “Direct tin-coating of the aluminum rear contact by ultrasonic soldering,” in *Proceedings of the 27th European Photovoltaic Solar Energy Conference and Exhibition*, 2012, pp. 1150–1153.
- [186] P. Schmitt, D. Eberlein, C. Ebert, M. Tranzitz, U. Eitner, and H. Wirth, “Adhesion of Al-metallization in ultra-sonic soldering on the Al-rear side of solar cells,” *Energy Procedia*, vol. 38, pp. 380–386, 2013.
- [187] H. Schulte-Huxel, S. Blankemeyer, V. Steckenreiter, S. Kajari-Schroeder, and R. Brendel, “Laser-welded interconnection of screen-printed Si solar cells,” *Energy Procedia*, vol. 55, pp. 356–360, 2014.
- [188] E. van Kerschaver, R. Einhaus, J. N. Szlufcik, and R. Mertens, “A novel silicon cell structure with both external polarity contacts on the back surface,” in *Proceedings of the 2nd World Conference and Exhibition on Photovoltaic Solar Energy Conversion*, 1998, pp. 1479–1482.
- [189] E. van Kerschaver, S. d. Wolf, and J. Szlufcik, “Towards back contact silicon solar cells with screen printed metallisation,” in *Proceedings of the 28th IEEE Photovoltaic Specialist Con-ference*, 2000, pp. 209–212.

- [190] J. Bultman, M. Brieko, A. Burgers, J. Hoornstra, A. Tip, and A. Weeber, "Interconnection through vias for improved efficiency and easy module manufacturing of crystalline silicon solar cells," *Solar Energy Materials and Solar Cells*, vol. 65, no. 1-4, pp. 339–345, 2001.
- [191] E. L. Ralph, "Recent advancements in low cost solar cell processing," in *Proceedings of the 11th IEEE Photovoltaic Specialists Conference*, 1975, pp. 315–316.
- [192] F. Kiefer, R. Peibst, T. Ohrdes, T. Dullweber, J. Krügener, H. J. Osten, C. Schöllhorn, A. Grohe, and R. Brendel, "Influence of the boron emitter profile on V_{OC} and j_{SC} losses in fully ion implanted n-type PERT solar cells," *physica status solidi (a)*, vol. 212, no. 2, pp. 291–297, 2015.
- [193] A. Edler, V. D. Mihailetschi, L. J. Koduvelikulathu, C. Comparotto, R. Kopecek, and R. Harnay, "Metallization-induced recombination losses of bifacial silicon solar cells," *Progress in Photovoltaics: Research and Applications*, vol. 23, no. 5, pp. 620–627, 2015.
- [194] L. Tous, M. Aleman, R. Russell, E. Cornagliotti, P. Choulat, A. Uruena, S. Singh, J. John, F. Duerinckx, J. Poortmans, and R. Mertens, "Evaluation of advanced p-PERL and n-PERT large area silicon solar cells with 20.5% energy conversion efficiencies," *Progress in Photovoltaics: Research and Applications*, vol. 23, no. 5, pp. 660–670, 2015.
- [195] E. Cornagliotti, A. Sharma, A. Uruena, M. Aleman, L. Tous, R. Russell, J. Chen, J. John, F. Duerinckx, B. Dielissen, R. Görtzen, and L. Black, "Large area n-type C-Si solar cells featuring rear emitter and efficiency beyond 21 %," in *Proceedings of the 6th World Conference on Photovoltaic Energy Conversion*, 2014, pp. 1–5.
- [196] F. Duerinckx, A. Uruena, M. Aleman, E. Cornagliotti, A. Sharma, P. Choulat, L. Tous, M. Recaman, I. Kuzma-Filipek, A. Hajiah, R. Dang, R. Russell, M. Haslinger, J. John, and J. Szlufcik, "Ni/Cu plated n-Si rear junction cells with efficiencies up to 22% (and above)," presented at *5th nPV-Workshop 2015, Konstanz, Germany*, 2015.
- [197] www.boerse.de, 04.01.2015. [Online]. Available: <http://www.boerse.de/>
- [198] M. Alonso and E. J. Finn, *Physik*. Bonn: Addison-Wesley, 1977.
- [199] D. Macdonald and L. J. Geerligs, "Recombination activity of interstitial iron and other transition metal point defects in p- and n-type crystalline silicon," *Applied Physics Letters*, vol. 85, no. 18, pp. 4061–4063, 2004.
- [200] J. Benick, B. Hoex, M. C. M. van de Sanden, W. M. M. Kessels, O. Schultz, and S. W. Glunz, "High efficiency n-type Si solar cells on Al_2O_3 -passivated boron emitters," *Applied Physics Letters*, vol. 92, no. 25, 253504, 2008.
- [201] H. Schumann and H. Oettel, Eds., *Metallografie*, 14th ed. Weinheim: Wiley-VCH, 2005.
- [202] H. H. Berger, "Models for contacts to planar devices," *Solid-State Electronics*, vol. 15, no. 2, pp. 145–158, 1972.
- [203] S. Eidelloth and R. Brendel, "Analytical theory for extracting specific contact resistances of thick samples from the transmission line method," *IEEE Electron Device Letters*, vol. 35, no. 1, pp. 9–11, 2014.
- [204] P. Richet, "Heat capacity of silicate glasses," *Chemical Geology*, vol. 62, no. 1-2, pp. 111–124, 1987.
- [205] D. Mann, R. E. Field, and R. Viskanta, "Determination of specific heat and true thermal conductivity of glass from dynamic temperature data," *Wärme- und Stoffübertragung*, vol. 27, no. 4, pp. 225–231, 1992.
- [206] R. Hull, *Properties of crystalline silicon*, ser. EMIS datareviews series. London: INSPEC, 1999, vol. 20.

- [207] C. Glassbrenner and G. Slack, “Thermal conductivity of silicon and germanium from 3 K to the melting point,” *Physical Review*, vol. 134, no. 4A, pp. A1058–A1069, 1964.
- [208] P. P. Altermatt, J. O. Schumacher, A. Cuevas, M. J. Kerr, S. W. Glunz, R. R. King, G. Heiser, and A. Schenk, “Numerical modeling of highly doped Si:P emitters based on fermi–dirac statistics and self-consistent material parameters,” *Journal of Applied Physics*, vol. 92, no. 6, pp. 3187–3197, 2002.
- [209] B. Hoex, J. Schmidt, R. Bock, P. P. Altermatt, M. C. M. van de Sanden, and W. M. M. Kessels, “Excellent passivation of highly doped p-type Si surfaces by the negative-charge-dielectric Al₂O₃,” *Applied Physics Letters*, vol. 91, no. 11, 112107, 2007.
- [210] T. Ohrdes, “Charakterisierungsmethoden und simulationsgestützte Analysen von Silizium Solarzellen,” Ph.D. dissertation, Leibniz Universität Hannover, Hannover, 2014. [Online]. Available: <http://edok01.tib.uni-hannover.de/edoks/e01dh15/813192161.pdf>
- [211] C. Mader, J. Müller, S. Eidelloth, and R. Brendel, “Local rear contacts to silicon solar cells by in-line high-rate evaporation of aluminum,” *Solar Energy Materials and Solar Cells*, vol. 107, pp. 272–282, 2012.
- [212] A. Yu, “Electron tunneling and contact resistance of metal-silicon contact barriers,” *Solid-State Electronics*, vol. 13, no. 2, pp. 239–247, 1970.
- [213] A. Fell, K. C. Fong, K. R. McIntosh, E. Franklin, and A. W. Blakers, “3-D simulation of interdigitated-back-contact silicon solar cells with quokka including perimeter losses,” *IEEE Journal of Photovoltaics*, vol. 4, no. 4, pp. 1040–1045, 2014.

List of publications

Publications arising from the work in this thesis:

Refereed journal papers

1. R. Brendel, J. H. Petermann, D. Zielke, H. Schulte-Huxel, M. Kessler, S. Gatz, S. Eidelloth, R. Bock, E. Garralaga Rojas, J. Schmidt, and T. Dullweber, "High-efficiency cells from layer transfer: a first step toward thin-film/wafer hybrid silicon technologies," *IEEE Journal of Photovoltaics* **1** (1), pp. 9-15, 2011. doi:10.1109/JPHOTOV.2011.2165529
2. H. Schulte-Huxel, R. Bock, S. Blankemeyer, A. Merkle, and R. Brendel, "Aluminum-based mechanical and electrical laser interconnection process for module integration of silicon solar cells," *IEEE Journal of Photovoltaics* **2** (1), pp. 16-21, 2012. doi:10.1109/JPHOTOV.2011.2177072
3. H. Schulte-Huxel, S. Blankemeyer, R. Bock, A. Merkle, S. Kajari-Schröder, and R. Brendel, "Aging behaviour of laser welded Al-interconnections in crystalline silicon modules," *Solar Energy Materials & Solar Cells* **106**, pp. 22-26, 2012. doi:10.1016/j.solmat.2012.06.021
4. H. Schulte-Huxel, S. Blankemeyer, R. Bock, A. Merkle, S. Kajari-Schröder, and R. Brendel, "Al-foil on encapsulant for the interconnection of al-metalized silicon solar cells," *IEEE Journal of Photovoltaics* **3** (1), pp. 77-82, 2013. doi:10.1109/JPHOTOV.2012.2208096
5. A. Merkle¹, H. Schulte-Huxel¹, S. Blankemeyer, I. Feilhaber, R. Bock, V. Steckenreiter, S. Kajari-Schröder, N.-P. Harder, and R. Brendel, "From high-efficiency *n*-type solar cells to modules exceeding 20% efficiency with aluminum-based cell interconnection," *Progress in Photovoltaics: Research and Applications* **21** (6), pp. 1354-1362, 2013. doi:10.1002/pip.2297
6. H. Schulte-Huxel, S. Blankemeyer, A. Merkle, S. Kajari-Schröder, and R. Brendel, "Laser microwelding of thin Al layers for interconnection of crystalline Si solar cells: analysis of process limits for ns and μ s lasers," *Journal of Photonics for Energy* **4**, 041597-1-13, 2014. doi:10.1117/1.JPE.4.041597
7. J. H. Petermann, H. Schulte-Huxel, V. Steckenreiter, S. Kajari-Schröder, and R. Brendel, "Principle of module-level processing demonstrated at single a-Si:H/c-Si heterojunction solar cells," *IEEE Journal of Photovoltaics* **4** (4), pp. 1018-1024, 2014. doi:10.1109/JPHOTOV.2014.2314576
8. H. Schulte-Huxel, S. Blankemeyer, A. Merkle, V. Steckenreiter, S. Kajari-Schröder, and R. Brendel, "Interconnection of busbar-free back contacted solar cells by laser welding," *Progress in Photovoltaics: Research and Applications* **23** (8), pp. 1057-1065, 2015. doi:10.1002/pip.2514
9. H. Schulte-Huxel, S. Kajari-Schröder, and R. Brendel, "Analysis of Thermal Processes Driving Laser Welding of Aluminum Deposited on Glass Substrates for Module Interconnection of Silicon Solar Cells," *IEEE Journal of Photovoltaics* **5** (6), pp. 1606-1612, 2015. doi:10.1109/JPHOTOV.2015.2478027

¹Both first authors contributed equally.

Papers presented at international conferences

1. J. H. Petermann, H. Schulte-Huxel, V. Steckenreiter, R. Gogolin, S. Eidelloth, T. Dullweber, S. Kajari-Schröder, and R. Brendel, "Module interconnection of both sides-contacted silicon solar cells by screen-printing," In *Proceedings of the 39th IEEE Photovoltaic Specialists Conference*, pp. 3448-3453, 2013. doi:10.1109/PVSC.2013.6745190
2. M. Ernst, H. Schulte-Huxel, R. Niepelt, S. Kajari-Schröder, and R. Brendel, "Thin crystalline macroporous silicon solar cells with ion implanted emitter," *Energy Procedia* **38**, pp. 910-918, 2013. doi:10.1016/j.egypro.2013.07.364
3. R. Brendel, T. Dullweber, R. Gogolin, H. Hannebauer, N.-P. Harder, J. Hensen, S. Kajari-Schröder, R. Peibst, J. H. Petermann, U. Römer, J. Schmidt, H. Schulte-Huxel and V. Steckenreiter, "Recent progress and options for future crystalline silicon solar cells," In *Proceedings of the 28th European Photovoltaic Solar Energy Conference*, pp. 676-690, 2013. doi:10.4229/28thEUPVSEC2013-2BP.1.1
4. H. Schulte-Huxel, S. Blankemeyer, V. Steckenreiter, S. Kajari-Schröder, and R. Brendel, "Laser-welded interconnection of screen-printed Si solar cells," *Energy Procedia* **55**, pp. 356-360, 2014. doi:10.1016/j.egypro.2014.08.102
5. H. Schulte-Huxel, U. Römer, S. Blankemeyer, A. Merkle, Y. Larionova, V. Steckenreiter, R. Peibst, S. Kajari-Schröder, and R. Brendel, "Two-level metallization and module integration of point-contacted solar cells," *Energy Procedia* **55**, pp. 361-368, 2014. doi:10.1016/j.egypro.2014.08.104
6. R. Peibst, U. Römer, Y. Larionova, H. Schulte-Huxel, T. Ohrdes, M. Häberle, B. Lim, J. Krügener, D. Stichtenoth, T. Wütherich, C. Schöllhorn, J. Graff, and R. Brendel, "Building blocks for back-junction back-contacted cells and modules with ion-implanted poly-si junctions," In *Proceedings of the 40th IEEE Photovoltaic Specialists Conference*, pp. 0852-0856, 2014. doi:10.1109/PVSC.2014.6925049
7. H. Schulte-Huxel, S. Blankemeyer, V. Steckenreiter, S. Kajari-Schröder, and R. Brendel, "Solar cell interconnection by laser spot welding of thin aluminum layers: analysis of process limits for ns- and μ s-lasers," In *Ser. SPIE Proceedings, Laser Applications in Microelectronic and Optoelectronic Manufacturing (LAMOM) XIX*, 896716, 2014. doi:10.1117/12.2037628
8. R. Witteck, D. Hinken, J. Müller, S. Blankemeyer, K. Bothe, H. Schulte-Huxel, M. Köntges, and R. Brendel, "Simulation of optimized cell interconnection for PERC modules exceeding 300 W," In *Proceedings of the 6th World Conference on Photovoltaic Energy Conversion*, pp. 515-516, 2015.
9. H. Schulte-Huxel, S. Kajari-Schröder, and R. Brendel, "Thermal processes driving laser-welding for module interconnection," In *Proceedings of the 42nd IEEE Photovoltaic Specialists Conference*, pp. NA, 2015. doi: 10.1109/PVSC.2015.7356432

Patent applications

1. H. Schulte-Huxel, S. Blankemeyer, R. Brendel, R. Bock, T. Dullweber, N.-P. Harder, C. Hampe, Y. Larionova, "Method for electrically connecting several solar cells and photovoltaic module," International Patent Application WO/2012/171968.

Oral presentations

Oral presentations published in conference proceedings are not listed.

1. H. Schulte-Huxel, "AMELI-Aluminum-based Mechanical and Electrical Laser Interconnection," SiliconForest Workshop, Falkau, Germany, 4.-7.03.2012.
2. H. Schulte-Huxel, S. Blankemeyer, R. Bock, S. Kajari-Schröder, and R. Brendel, "Laser spot welding of thin aluminum layers for mechanical and electrical connection for photovoltaic application", E-MRS 2012 Spring Meeting, Symposium V, Strasbourg, France, 14.-18.05.2012.
3. S. Kajari-Schröder, V. Steckenreiter, H. Schulte-Huxel, M. Ernst, J. H. Petermann, and F. Haase, "Thin crystalline silicon hybrid technologies," Workshop on advanced concepts in silicon based photovoltaics, Oslo, Norway, 20.-22.06.2012.
4. H. Schulte-Huxel, A. Merkle, S. Blankemeyer, T. Friedrich, I. Feilhaber, R. Bock, V. Steckenreiter, S. Kajari-Schröder, N.-P. Harder, and R. Brendel, "From high-efficiency silicon solar cells to modules exceeding 20% efficiency with aluminum-based cell interconnection," 27th European Photovoltaic Solar Energy Conference, Frankfurt, Germany, 24.-28.09.2012. (plenary presentation)
5. H. Schulte-Huxel, S. Blankemeyer, A. Merkle, T. Friedrich, V. Steckenreiter, S. Kajari-Schröder, and R. Brendel, "Micro welding of Al-metallized solar cells," 4th Workshop on MWT solar cell and module technology, Amsterdam, The Netherlands, 21.-22.11.2012. (invited presentation)
6. H. Schulte-Huxel, S. Kajari-Schröder, and R. Brendel, "Laser spot welding of thin aluminum layers for photovoltaic applications", Seminar at Bremer Institut für angewandte Strahltechnik (BIAS), Bremen, Germany, 2.04.2013. (invited presentation)
7. S. Kajari-Schröder, H. Schulte-Huxel, A. Merkle, S. Blankemeyer, V. Steckenreiter, M. Ernst, and R. Brendel, "The AMELI process," 3rd nPV workshop, Chambéry, France, 22.-23.04.2013. (invited presentation)
8. H. Schulte-Huxel, "Füllfaktorerrhöhung durch Modulverschaltung mittels Laserschweißen," SiliconForest Workshop, Falkau, Germany, 23.-26.02.2014.
9. H. Schulte-Huxel, S. Blankemeyer, V. Steckenreiter, S. Kajari-Schröder, and R. Brendel, "Laser welding for module interconnection of Al metallized solar cells," APPOLO Workshop Laser processing in Photovoltaics, Leipzig Germany, 27.-28.11.2014. (invited presentation)
10. H. Schulte-Huxel, R. Witteck, S. Blankemeyer, K. Bothe, R. Peibst, T. Dullweber, M. Köntges, and R. Brendel, "From PERC and BJBC solar cells to modules - electrical and optical gains and losses," Seminar at National Renewable Energy Laboratory (NREL), Golden, Colorado, USA, 22.06.2015. (invited presentation)

Non-refereed journal papers

1. N.-P. Harder, A. Merkle, T. Brendemühl, F. Kiefer, R. Gogolin, M. Lehr, F. Heinemeyer, H. Schulte-Huxel, B. Lim, V. Jung, S. Kajari-Schröder, M. Köntges, and R. Brendel, "Back-contacted high-efficiency silicon solar cells - opportunities for low-cost metallization and cell interconnection," *PV International* **17**, pp. 50-60, 2012
2. Henning Schulte-Huxel and Sarah Kajari-Schröder, "AMELI - neuer Laserschweißprozess für Solarzellen", *ti Technologie-Informationen* **1**, p. 12, 2013

CURRICULUM VITAE

HENNING SCHULTE-HUXEL

Born January 10, 1985
in Dorsten, Germany

Stammestr. 42
30459 Hannover
Germany

Email:
hschultehuxel@googlemail.com

ACADEMIC EDUCATION

- | | |
|-------------------|--|
| 10.2012 - 10.2014 | Jena University, Germany, Laser technique by correspondence course |
| 10.2008 - 01.2010 | Leipzig University, Germany, Master studies in physics
Degree: Master of Science in Physics |
| 10.2007 - 02.2008 | Bucharest University, Romania, Erasmus Program |
| 10.2005 - 09.2008 | Leipzig University, Germany, Bachelor studies in physics
Degree: Bachelor of Science in Physics |

WORKING EXPERIENCE

- | | |
|-------------------|--|
| since 07.2014 | Scientist and project manager, Module technologies,
Institute for Solar Energy Research Hamelin (ISFH), Germany |
| 10.2010 - 06.2014 | Scientist, Future technologies photovoltaics,
Institute for Solar Energy Research Hamelin (ISFH), Germany |

SCHOOL EDUCATION AND CIVILIAN SERVICE

- | | |
|-------------------|---|
| 09.2004 - 07.2005 | Alternative civilian service, Don Bosco Centre, Negombo und
Murunkan, Sri Lanka |
| 09.1997 - 05.2004 | Gymnasium der Mariannahiller Missionare, Maria-Veen, Germany,
Degree: Abitur (Allgemeine Hochschulreife) |

Danksagung

Zum Schluss möchte ich mich ganz herzlich bei all denen bedanken, die zum Gelingen dieser Arbeit beigetragen haben. Mein besonderer Dank gilt:

- Prof. Dr.-Ing. Rolf Brendel für die Betreuung meiner Dissertation und die Möglichkeit, diese am ISFH durchführen zu können; für die wertvollen Anregungen während der Erstellung und den Freiraum beim Ausgestalten dieser Arbeit;
- Prof. Dr. Jef Poortmans für die freundliche Übernahme des Korreferats;
- Prof. Dr. Michael Oestreich für die Übernahme des Prüfungsvorsitzes;
- Sarah Kajari-Schröder für die ausgezeichnete wissenschaftliche Begleitung, immer Zeit für meine Fragen zu haben und unsere fruchtbaren Diskussionen.
- Susanne Blankemeyer für die unermüdliche experimentelle und weit darüber hinausgehende Unterstützung. Ohne deinen besonderen Einsatz hätten viele Ergebnisse dieser Arbeit nicht realisiert werden können.
- Dem CrystalLine Projekt-Team - Robert Bock, Verena Steckenreiter, Agnes Merkle, Jan Petermann, Susanne Blankemeyer, Ilka Feihlhaber und Thomas Friedrich - für unzählige Zellen und Proben, viel Unterstützung und wertvolle Diskussionen;
- Tobias Neubert, David Sylla und Peter Giesel für die Unterstützung an den Laseranlagen, wo sie immer wieder Unmögliches möglich gemacht haben;
- Frank Heinemeyer und Daniel Münster für Unterstützung an der ATON;
- Alexandra Pazidis für die AR-Beschichtungen sowie ihr, Christine Hein und Christian Peest für die Reflektionsmessungen;
- Robert Witteck für die LBIC-Messungen;
- Tobias Ohrdes für die SENTAURUS DEVICE Simulationen;
- Bettina Wolpensinger für die Unterstützung am REM;
- Waldemar Geist und Florent Paugam, die im Rahmen ihrer Abschlussarbeiten mechanische Aspekte des AMELI-Prozesses untersucht haben;
- Sarah Kajari-Schröder, Udo Römer, Susanne Blankemeyer und Heike Wadepohl für das unermüdliche Korrekturlesen;
- Udo Römer, Fabian Kiefer, Robby Peibst, Marc Köntges, Karsten Bothe, Nils-Peter Harder, Iris Kunze, Arnaud Morlier, Malte Vogt, Robert Witteck, Carsten Schinke, Bianca Lim, Boris Veith-Wolf, David Hinken, Dimitri Zielke, Marita Steinhof, Stefan Eidelloth, Ulrike Baumann, Michael Rienäcker, Matthias Offer, Till Brendemühl, Susanne Mau, Damaris Kröber, Jan Krügener, Ingo Ahrens, Arne Schmidt, Sarah Spätlich, Susanne Mau und den Dünn-Si-Kolleg-innen für die wertvollen Diskussionen, Korrekturen und vielseitige Unterstützung;
- Allen Mitarbeiter-innen am ISFH für eure Offenheit und Hilfsbereitschaft sowie die freundliche und entspannte Arbeitsatmosphäre;
- Heike für deine unglaubliche Unterstützung, Geduld und die "Arbeits"-Teilung.